

Primary User Detection and Protection in Broadband Cognitive Radio Systems

Cornelius Allamis Dawap Pahalson

PhD Thesis

Centre for Signal and Image Processing (CeSIP)
Department of Electronic and Electrical Engineering
University of Strathclyde, Glasgow, Scotland

March 31, 2026

This thesis is the result of the author's original research. It has been composed by the author and has not been previously submitted for examination, which has led to the award of a degree.

The copyright of this thesis belongs to the author under the terms of the United Kingdom Copyright Acts as qualified by University of Strathclyde Regulation 3.50. Due acknowledgements must always be made of the use of any material contained in, or derived from, this thesis.

Abstract

The radio spectrum remains a scarce resource under increasing demand for wireless communication despite evolving technologies. Cognitive Radio (CR) addresses this by allowing secondary users (SUs) to access underutilized licensed spectrum. A key function of CR systems is spectrum sensing, which detects primary users (PUs) and identifies available spectral opportunities for secondary use. Therefore, this thesis presents a set of advanced signal processing techniques for broadband array systems that address three challenges in the context of CR systems: detecting weak transient signals, designing targeted jamming strategies against hostile sources, and characterizing dynamic noise environments.

Firstly, we investigate the detection of weak broadband transients, such as emerging PUs, using a polynomial subspace approach and simple energy detection. In order to benchmark this method, it is compared to a likelihood ratio test (LRT). Although the LRT is statistically optimal, it can be computationally demanding and is shown to be numerically sensitive to data with high temporal correlation. Simulations demonstrate that restricting the LRT to the subspace data can significantly enhance its detection performance. We show that this is due to the fact that the subspace projection step whitens and compacts the data, reducing dimensionality and improving numerical stability. This explains the generally improved performance of the LRT when operating on subspace data rather than raw sensor data. This also establishes the polynomial subspace detector as a simple technique that, in such situations, can perform close to the LRT, even though the former does not require any knowledge of the channel or the statistics of the transient signal on which the LRT relies.

Secondly, if any transient sources are detected and might be deemed a hostile, this thesis addresses the design of jamming signals to interfere with these sources while preserving friendly users. Two scenarios are considered: one with known transmission paths, using a broadband multiple-input multiple-output (MIMO) beamforming approach based on an analytic singular value decomposition (SVD); and another that relies on channel reciprocity and on employing a time-reversal technique. The former sets an upper bound on performance, while the latter provides a robust alternative if the channel to the hostile source is unknown.

Lastly, we develop methods for estimating the time-varying power spectral density (PSD) of noise to identify opportunities for detecting weak signals. For simplicity, a single noise source is assumed. The framework combines a basis expansion model (BEM) with space-time covariance estimation, and the estimate is enhanced by optimal lag support selection and rank-one approximation via an analytic eigenvalue decomposition (EVD). These techniques yield significant improvements in estimation accuracy, particularly in environments with slow variations.

Collectively, the contributions of this thesis provide robust and efficient solutions for signal detection, interference control, and noise characterisation in complex broadband array processing scenarios.

Contents

Abbreviations	ix
List of Figures	xv
List of Tables	xvi
Mathematical Notations	xvii
List of Symbols	xviii
Publications	xxii
Acknowledgements	xxiii
1 Introduction	1
1.1 Motivation	1
1.2 Contributions of Thesis	5
1.3 Overview of Study	6
2 Background	9
2.1 Introduction	9
2.2 Energy Detection-Based Spectrum Sensing	10
2.2.1 Performance Criteria	11
2.2.2 Energy Detection Methods	13
2.2.3 Cyclostationary Feature Detection	19

Contents

2.2.4	Matched Filter Detection	21
2.2.5	Covariance-Based Detection	23
2.2.6	MIMO-Based Change-Point and Energy Detection	24
2.2.7	Discussion	25
2.3	Broadband Multiple-Input Multiple-Output Systems Descriptions	27
2.3.1	Broadband Channel Description	27
2.3.2	Space-Time Covariance Matrix	29
2.3.3	Broadband versus Narrowband Consideration	33
2.4	Eigenvalue Decomposition of a Parahermitian Matrix	35
2.4.1	Parahermitian Matrix EVD	35
2.4.2	Application to Strong Decorrelation and Subspace Decomposition	36
2.4.3	Parahermitian Matrix EVD Algorithms	38
2.5	Polynomial Matrix Singular Value Decomposition	41
2.5.1	Analytic SVD	41
2.5.2	Relation to Analytic EVD	42
2.5.3	Polynomial Matrix SVD Algorithms and Applications	43
2.6	Chapter Summary	44
3	Detection of Weak Transient Broadband Signals	45
3.1	Introduction	45
3.2	Data Model and Space-Time Covariance Matrix	47
3.2.1	Data model	47
3.2.2	Space-Time Covariance Matrices	48
3.3	Polynomial Subspace Detection	49
3.3.1	Analytic Eigenvalue Decomposition	49
3.3.2	Subspace Projection and Syndrome Vector	50
3.4	Syndrome Energy	53
3.4.1	Signal Statistics	54
3.4.2	Decimated Subspace Detector	55
3.4.3	Performance Metrics	57

Contents

3.5	Benchmark Using Likelihood Ratio Test	60
3.5.1	Likelihood Ratio Test	61
3.5.2	Likelihood Ratio Test on Measurements	62
3.5.3	Likelihood Ratio Test Applied to Subspace Data	63
3.5.4	Generalized Likelihood Ratio Test	64
3.6	Analysis of Subspace-Based LRT	65
3.6.1	Temporal Correlation	65
3.6.2	Covariance Matrix Conditioning	67
3.7	Generalised Likelihood Ratio Test Implementation	68
3.7.1	Implementation Overview	69
3.7.2	Cross-Correlation Estimation	70
3.7.3	Unbiased Estimation	70
3.7.4	Variance of Estimator	71
3.8	Simulation Results	73
3.8.1	Performance Metrics, Algorithms, and Parameters	73
3.8.2	Simulation	74
3.8.3	Changing SNR and Support of Mixing System	76
3.9	Chapter Summary	77
4	Time Reversal Methods to Enable and Protect Primary Users	84
4.1	Introduction	84
4.2	Scenario and Signal Model	85
4.2.1	Reception and Transient Signal Detection	85
4.2.2	Transmission and Channel Reciprocity	89
4.3	Signal Power Based on Innovation Filter Model	90
4.4	Power Transfer with Known Channel	92
4.4.1	Broadband Null Steering	92
4.4.2	Maximizing Power Transfer	93
4.5	Power Transfer Based on Time Reversal	95
4.5.1	Time Reversal Approach	95

Contents

4.5.2	Transmit Power	96
4.5.3	Received Power of Jamming Signal	98
4.6	Results	99
4.6.1	Parameters and Metrics	99
4.6.2	Simulations	100
4.7	Chapter Summary	102
5	Monitoring Time-Varying Noise PSD	103
5.1	Introduction	103
5.1.1	Preliminaries	103
5.1.2	Background and Overview	104
5.2	Signal Model	105
5.2.1	Innovation Filter Model	105
5.2.2	Basis Expansion Model	106
5.3	Expected Noise Power Spectral Density	108
5.3.1	Space-Time Covariance and Cross Spectral Density Matrices	108
5.3.2	Power Spectral Density	109
5.4	Estimated Noise Power Spectral Density	111
5.4.1	Spectral Estimation	111
5.4.2	Space-Time Covariance Matrix Estimation	112
5.5	PSD Via Enhanced Covariance Estimation	114
5.5.1	Optimized Lag Support	114
5.5.2	Rank One Approximation	115
5.6	Results	117
5.6.1	Parameters and Metrics	118
5.6.2	Ensemble Results	118
5.7	Chapter Summary	121
6	Conclusions and Future Work	123
6.1	Summary and Conclusions	123

Contents

6.2 Suggestions for Future Work 126

References **128**

Abbreviations

AOA	Angle of Arrival
AWGN	Additive White Gaussian Noise
BEM	Basis Expansion Model
BLUE	Best Linear Unbiased Estimator
CE-BEM	Complex Exponential BEM
CR	Cognitive Radio
CRN	Cognitive Radio Network
CSD	Cross Spectral Density
DOA	Direction of Arrival
CSI	Channel State Information
DFT	Discrete Fourier Transformation
DKL-BEM	Discrete Karhuen-Loéve BEM
DPS-BEM	Discrete Prolate Spheroidal BEM
DSA	Dynamic Spectrum Access
DSL	Digital Subscriber Line
DSP	Digital Signal Processing
EC	Energy Criterion
ED	Energy Detection
EVD	Eigenvalue Decomposition
FCC	Federal Communication Commission
FFT	Fast Fourier Transformation
FIR	Finite Impulse Response

Contents

FLOPS	Floating Point Operations
GLRT	Generalized Likelihood Ratio Tests
LRT	Likelihood Ratio Test
LLR	Log Likelihood Ratio (Test)
MAC	Multiply-Accumulate
MATLAB	Matrix Laboratory
MIMO	Multiple Input Multiple Output
MUSIC	Multiple Signal Classification
OFcom	Office of Communication
P-BEM	Polynomial BEM
PCA	Principal Component Analysis
P_D	Probability of Detection
P_{FA}	Probability of False Alarm
PEVD	Polynomial Matrix Eigenvalue Decomposition
P_M	Probability of Miss Detection
PQRD	Polynomial Matrix QR Decomposition
PSVD	Polynomial Matrix Singular Value Decomposition
PU	Primary User
QoS	Quality of Service
QRD	QR Decomposition
RF	Radio Frequency
rhs	right-hand side
RMT	Random Matrix Theory
ROC	Receiver Operating Characteristics
SBR2	Second Order Sequential Best Rotation Algorithm
SDR	Software-Defined Radio
SMD	Sequential Matrix Diagonalisation Algorithm
SNR	Signal-to-Noise Ratio
SONAR	Sonic Radar

Contents

s.t.	subject to
SU	Secondary User
SVD	Singular Value Decomposition
WLAN	Wireless Local Area Network
w.r.t	with respect to

List of Figures

1.1	Example of locally measured radio spectrum occupancy from 0–6 GHz, showing received power (dBm) versus frequency and integrated over a 24h time window in an urban environment (Singapore) [1].	2
1.2	Cognitive radio capabilities, after [2].	3
1.3	Spectrum band with spectrum holes or white spaces [3]	4
1.4	Links between research presented in the different core chapters of this thesis.	7
2.1	Examples PDFs of energy measurements x , $p(x \text{PU})$ and $p(x \overline{\text{PU}})$; ϑ denotes a decision threshold, which defines the probabilities of missed detection, P_M , and of false alarm, P_{FA}	12
2.2	Block diagram of MIMO system $\mathbf{C}[n] \in \mathbb{C}^{M \times L}$ with input $\mathbf{x}[n] \in \mathbb{C}^L$ and output $\mathbf{y}[n] \in \mathbb{C}^M$,	28
2.3	Channel $\mathbf{C}[n]$ for Example 1 comprising of channel impulse responses $c_{m,\ell}[n]$, $m, \ell = 1, 2$, with (\circ) and $(*)$ symbolising real and imaginary parts, respectively.	30
2.4	Space-time covariance matrix for Example 2 comprising of cross-correlation sequences $r_{m,\mu}[\tau]$, $m, \mu = 1, 2$, with (\circ) and $(*)$ symbolising real and imaginary parts, respectively.	33
2.5	Parahermitian matrix EVD factors (a) $\mathbf{Q}[n] \circ \bullet \mathbf{Q}(z)$ and (b) $\mathbf{\Lambda}[\tau] \bullet \circ \mathbf{\Lambda}(z)$ for Example 3, with (\circ) and $(*)$ symbolising real and imaginary parts, respectively.	36

List of Figures

2.6	Eigenvalues $\lambda_m(e^{j\Omega})$, $m = 1, 2$, of Example 3.	37
2.7	Applying parahermitian matrix factors for (a) strong decorrelation and (b) subspace decomposition.	37
2.8	Results of the SMD algorithm in Example 4 approximating the EVD factors (a) $\hat{\mathbf{Q}}[n] \circ \bullet \mathbf{Q}(z)$ and (b) $\hat{\mathbf{\Lambda}}[\tau] \circ \bullet \mathbf{\Lambda}(z)$ of $\mathbf{R}(z)$ from Example 2, with (\circ) and (\bullet) symbolising real and imaginary parts, respectively. . .	40
2.9	Approximate eigenvalues $\hat{\lambda}_m(e^{j\Omega})$, $m = 1, 2$, obtained with the SMD algorithm, with the ground truth analytic eigenvalues of Example 3 un- derlaid in grey.	41
2.10	Singular values $\sigma_m(e^{j\Omega})$, $m = 1, 2$, of Example 5.	43
3.1	Signal model for measurement $\mathbf{x}[n] \in \mathbb{C}^M$, containing stationary sources $\mathbf{u}[n] \in \mathbb{C}^L$, and a transient source $\mathbf{u}_t[n]$ and processing by $\mathbf{Q}_{\perp}^H[-n]$ to yield a subspace projection $\mathbf{s}[n] \in \mathbb{C}^{M-L}$	48
3.2	Sensor signal with transient signal presented during the interval $n \in$ (1200, 1800): (a) real and imaginary parts of first sensor signal $x_1[n]$, and (b) total sensor energy $\ \mathbf{x}[n]\ _2^2$ across all sensors.	52
3.3	Syndrome signal: (a) real and imaginary parts of the first element of $\mathbf{s}[n]$ and (b) energy of the syndrome vector $\ \mathbf{s}[n]\ _2^2$	53
3.4	Flow graph of decimated averaging of syndrome energy.	55
3.5	Measured and theoretical generalized χ^2 distributions of the energy $\ \mathbf{s}[n]\ _2^2$ for $T = 1$, comparing scenarios with and without a transient signal. . .	56
3.6	Receiver-operating characteristic (ROC) curves showing detection per- formance under varying false alarm rates.	57
3.7	Measured and theoretical generalized χ^2 distributions of the energy $\ \mathbf{s}[n]\ _2^2$ for $T = 10$, comparing scenarios with and without a transient signal. .	58
3.8	Receiver-operating characteristic (ROC) curves showing detection per- formance under varying false alarm rates.	59

List of Figures

3.9	Discrimination \mathcal{D} vs decision time \mathcal{T} for detecting transient sources of different strength (medium powered source 2, low-powered source 3), based on estimates of the space-time covariance relying on various sample sizes N	60
3.10	Block diagram for LRT/GLRT implementation.	69
3.11	Separability of distributions for different approaches with $M = 8$ sensors, $L = 5$ stationary sources, a mixing system of order $K = 8$, and an SNR $\gamma = 10$ dB	79
3.12	ROC curve for the case $T = 10$ in Fig. 3.11.	79
3.13	Separability with mixing matrix order $K = 16$ compared to Fig. 3.11.	80
3.14	ROC curve for the case $T = 10$ in Fig. 3.13.	80
3.15	Separability with $K = 16$ and SNR $\gamma = 20$ dB compared to Fig. 3.11.	81
3.16	ROC curve for the case $T = 10$ in Fig. 3.15.	81
3.17	Separability of distributions for setting with $K = 10$ and the transient source 10 dB below the stationary sources.	82
3.18	(a) Separability of distributions and (b) condition numbers of covariance matrices for setting with $K = 20$ and the transient source 20 dB below the stationary sources.	83
4.1	Signal model for an M element array with measurement vector $\mathbf{x}_r[n]$, with a processor $\Phi[n]$ to observe an potential transient contributions from $\mathbf{u}_{r,2}[n]$ in the presence of stationary signals $\mathbf{u}_{r,1}[n]$	86
4.2	Signal model of the same M element array as in Fig. 4.1, but with the aim of maximum power transfer to the transient sources represented in $\mathbf{u}_{t,2}[n]$ while not interfering with the stationary sources represented by $\mathbf{u}_{t,1}[n]$. Compared to Fig. 4.1, the signals flow from right to left.	89
4.3	Model to explain the spatio-temporal correlation structure of a signal vector $\mathbf{x}[n]$ based on a spatially and temporally uncorrelated input vector $\mathbf{u}[n]$ and a spatio-temporal filter $\mathbf{A}[n]$	90

List of Figures

4.4	Power transfer γ_t vs. receive SNR γ_r for various dimensions L_2 of $\mathbf{u}_{t,2}[n]$ for $\Sigma_2(z) = \mathbf{I}$; lines indicate experimental values and markers represent theoretical values.	100
4.5	Parameters as in Fig. 4.4, but for a randomized $\Sigma_2(z)$ of order 3. The black horizontal line indicates the method of Sec. 4.4 with a suboptimal $\Pi(z) = \mathbf{I}$	101
5.1	Model for M measurements observing a single non-stationary source.	106
5.2	Time-varying PSD of Example 10 generated by a BEM.	110
5.3	Example 11 for time-varying PSD using the Welch method [4], estimating the PSD of Example 10 in Fig. 5.2.	112
5.4	Result of Example 12 for time-varying PSD estimation based on rank-one space-time covariance matrix estimations.	117
5.5	Ensemble mean PSD errors, where \bar{e}_{STC} and $\bar{e}_{\text{R-1}}$ depend on different lag supports T for the space-time covariance estimate. The two groups of curves are for different sample sizes of $N = 64$ and $N = 512$	119
5.6	Ensemble mean errors for PSD estimates as a function of sample size N for maximum Doppler frequency Ω_{max} in the BEM. Error bars represent one standard deviation of the ensemble distribution. (a) Higher Ω_{max} ; (b) Lower Ω_{max}	120

List of Tables

2.1	Summary of energy detection	20
2.2	Multiple Antennas-Based Spectrum Sensing	26
3.1	Powers of contributions for a realistic detection scenario, according to simulated channel impulse responses using a radio planning tool [5]. . .	58
3.2	Simulation parameters for the mixing system	75

Mathematical Notations

$\mathcal{E}[\cdot]$	Expectation
$\mathcal{L}(\cdot)$	Log likelihood ratio
\mathbf{I}_M	Identity matrix of size $m \times m$
$\ \cdot\ _F$	Frobenius norm(the square-root sum of squares of all elements)
$(\cdot)^{-1}$	Matrix inverse
$\lfloor \cdot \rfloor$	Floor, round down
$\{\cdot\}^*$	complex conjugate operator
$(\cdot)^H$	Hermitian conjugate of a matrix or vector
$(\cdot)^T$	Transposition of a matrix or vector
$(\cdot)^P$	Parahermitian transpose
$\text{tr}(\cdot)$	matrix trace operation
$\mathbb{C}^{M \times N}$	Polynomial matrices with complex coefficients ($M \times N$)
\mathbb{Z}	Set of integer numbers

List of Symbols

Notations	Description
Time and Frequency Variables	
z^{-1}	Unit delay operator
$z = e^{j\Omega}$	Complex frequency variable
$\Omega_{m,p}$	Angular frequency of the basis function
$\Omega_{m,q}$	Frequency modulation term
τ	Polynomial index
T	Window period
K	Frequency bin
Ω	Normalized angular frequency
Signal and System Variables	
$\mathbf{x}[n]$	Received signal vector at time n
$\mathbf{x}_t[n]$	Transmit signal in time domain
$\mathbf{x}'[n]$	Data vector (both stationary sources and a transient signal)
$\mathbf{y}_r[n]$	Received data vector
$v[n]$	Additive Gaussian noise
$\mathbf{u}[n]$	Signal input vector
P_o	Power budget
σ^2	Noise variance
γ_r	Receive SNR
γ_t	Jamming efficiency/Power transfer ratio

List of Symbols

ρ	Gain factor
$\mathbf{x}_r[n]$	Measurement vector
$\mathbf{u}_{r,1}[n] \in \mathbb{C}^{L_1}$	Stationary sources
$\mathbf{u}_{r,2}[n] \in \mathbb{C}^{L_2}$	Transient sources

Filter Banks and Channels

$\mathbf{C}(z)$	Polynomial MIMO transfer Matrix
$\mathbf{F}(z)$	Transmitter FIR filter bank
$\mathbf{G}_1[n] \in \mathbb{C}^{M \times L_1}$	Innovation filter of stationary sources
$\mathbf{G}_2[n] \in \mathbb{C}^{M \times L_2}$	Innovation filter of transient sources
$\mathbf{H}(z)$	Convolutional MIMO channel matrix
$\mathbf{H}(z) \bullet \text{---} \mathbf{H}[n]$	Matrix of transfer function
$\mathbf{H}_2(z)$	Effective channel to intended (hostile) target
$H_{m,p}(z)$	Transfer function at sensor m , basis p
$h_m[n, \ell]$	Impulse response at sensor m , delay ℓ
$h_{m,p}[\ell]$	Basis coefficients at sensor m , basis p
$n - \ell$	Delay index

Preprocessing and Decomposition

$\Psi_1(z)$	Preprocessing to null interference to desired user
$\Psi_2(z)$	Preprocessing to maximize the power transfer to $\mathbf{u}_{t,2}[n]$
\mathbf{U}	Unitary Matrix from SVD decomposition & Jacobi rotation Matrix
$\mathbf{U}(z)$	Paraunitary matrix from PSVD decomposition
\mathbf{V}	Unitary Matrix from SVD decomposition
$\mathbf{V}(z)$	Paraunitary matrix from PSVD decomposition
$\mathbf{\Lambda}(z)$	Diagonal parahermitian matrix
$\mathbf{Q}(z)$	Paraunitary matrix
Σ	Summation operation
$\mathbf{R}(z)$	Para-Hermitian polynomial matrix
$\mathbf{\Pi}(z)$	Power allocation matrix
$\pi_m(z)$	Power allocated to mode m at frequency z

List of Symbols

$\pi_m[n]$	Time-domain power allocation for mode m
$\mathbf{U}_{1,\perp}(z)$	Nullspace basis of $\mathbf{\Psi}_1(z)$
$\mathbf{U}_2(z)$	Left singular vectors of analytic SVD of $G_2(z)$
$\mathbf{U}_{2,\parallel}(z)$	Dominant singular vectors of $\mathbf{U}_2(z)$
$\mathbf{U}_{2,\perp}(z)$	Orthogonal complement to $\mathbf{U}_{2,\parallel}(z)$
$\mathbf{A}[n]$	System impulse response (matrix-valued)
$\mathbf{A}(z)$	z -transform / transfer matrix
$\mathbf{y}[n]$	System output
$\mathbf{R}_y[\tau]$	Output space-time covariance
$\mathbf{R}_y(z)$	Output spectral density (matrix)
ξ_x	Total output power
$\sigma_m(z)$	Singular values of $\mathbf{A}(z)$
$\mathbf{\Phi}[n]$	Processor matrix
$\mathbf{P}(z)$	Projection matrix
$G_1^P(z)$	Nullspace of $\mathbf{H}_1(z)$
$\tilde{\mathbf{G}}_2(z)$	Matrix of single transient user
$\mathbf{\Phi}^*[-n]$	filtering operation involving time reversal
$\mathbf{G}_2^*[-n]$	complex conjugates of the channel matrix
$\mathbf{u}_{t,2}^*[-n]$	complex conjugate of the transient sources signal
$\mathbf{v}^*[-n]$	complex conjugate of the observation noise
$\mathbf{B}_1[n]$	signal path from the original transient source
$\mathbf{B}_2[n]$	transfer path for the observation noise

Statistical and Spectral Quantities

H_0	Hypothesis 0 : absence of primary users
H_1	Hypothesis 1 : presence of primary users
\mathbf{R}_0	Covariance matrix of stationary source
\mathbf{R}_1	Covariance matrix of the transient signal
$\mathbf{y}_{0,n}$	Contribution of stationary sources and additive noise
$\mathbf{y}_{1,n}$	Components of the transient signal

List of Symbols

\mathbf{y}_n	Probability density functions under the two hypotheses
\mathbf{c}	Decision threshold
c'	Threshold in the absence of any transient signal
$p(\cdot)$	Probability density function
χ^2	Chi-square distribution
N	Number of samples
$\gamma_{\mathbf{x},1}, \gamma_{\mathbf{s},1}$	Condition number for measurement data and projected data
δ	Separability of distributions
μ_0, μ_1	Mean for stationary source and transient signal
σ_0, σ_1	Standard deviation for a stationary source and transient signal
σ_t^2, σ_v^2	Maximum power for stationary source and the transient signal
$\mathbf{R}_{\mathbf{x},1}, \mathbf{R}_{\mathbf{s},1}$	Covariance matrices for measurement and projected data
$\mathbf{R}[\tau, n]$	Space-time covariance matrix (lag τ , time n)
$r_{m\mu}[\tau, n]$	Cross-correlation between sensor m and μ
$R_{m\mu}(z, n)$	Cross-spectral density
$\hat{\mathbf{R}}(z, n)$	Empirical cross-spectral density
$\hat{R}_{1,mm}(e^{j\Omega}, n)$	Denoised PSD estimate
$e_{R-1}[n]$	PSD estimation error at time n
$\mathbf{h}(z, n)$	Concatenated frequency-domain response
$q_m(z, n)$	Eigenvector from spectral EVD
$\lambda_m(z, n)$	Eigenvalue from spectral EVD
$\sigma_{2,m}[n]$	Time-domain singular value of mode m

System Dimensions

M	Number of sensors (channels)
L	Number of stationary sources
Q	Number of basis functions / multipath
L_1	stationary sources
L_2	transient sources

Publications

The work presented in this thesis has led to several peer-reviewed publications which are listed below for reference.

1. C. A. D. Pahalson, L. H. Crockett, and S. Weiss, "Detection of weak transient broadband signals using a polynomial subspace and likelihood ratio test approach" in *Proceedings of the 32nd European Signal Processing Conference (EUSIPCO)*, Lyon, France, pp. 1312–1316, September 2024.
2. C. A. D. Pahalson, L. H. Crockett and S. Weiss, "Computational and numerical properties of a broadband subspace-based likelihood ratio test", *IEEE High Performance Extreme Computing Conference (HPEC)*, Waltham, MA, September 2024.
3. C. A. D. Pahalson and S. Weiss, "Broadband array time reversal method for jamming with protective constraints," in *Proceedings of the 23rd IEEE Statistical Signal Processing Workshop (SSP)*. Edinburgh, Scotland, pp.1–5, June 2025.
4. C. A. D. Pahalson, S. Weiss, T. Clarke, J.L. Deeks, and D.P. Williams, "Estimating Fluctuating Single Source Noise Power Spectral Densities in Sensor Array," in *proceedings of the 28th International Workshop on Smart Antennas (WSA)*, Erlangen, Germany, pp.7–12, September 2025.
5. C. A. D. Pahalson, L. H. Crockett and S. Weiss, "Detection of weak transient broadband signals: subspace and likelihood ratio test approaches" *Science Talks*, vol. 14, p. 100451, 2025.

Acknowledgements

First of all, I would like to express my gratitude to God Almighty, who in his infinite mercy has seen me through to the end of my PhD. May his name be praised forever. I sincerely thank my supervisor, Professor Stephan Weiss, for his support and encouragement throughout the study.

His technical insights, breadth of knowledge, and diligent advice have always inspired and motivated me ever since I began the research. Working with him broadened my perspective and strengthened my confidence in my rights and abilities, which led to the successful completion of this thesis. I shall be ever grateful for the inspiration and personal education he gave me.

The author thanks the supervision team for their support. The authors thank Dr. Mehrdad Yaghoobi Vaighan for serving as an external examiner at my PhD oral defense. I also thank Prof. Vladimir Stankovic for serving as my internal examiner. Also, would like to thank Dr. David H Crawford for chairing my PhD oral defense committee.

The author extends special thanks to Timothy Clarke, Julian L. Deeks, and Duncan P. Williams, Dstl Porton Down, Salisbury, SP4 0JQ, UK, as well as the Engineering and Physical Sciences Research Council (EPSRC) Grant number EP/S000631, and the MOD University Defense Research Collaboration in Signal Processing is acknowledged. The author thanks my fellow PhD colleagues and staff members for their contributions to my academic success. I assure you that all your contributions are greatly appreciated. In particular, I have met many good friends and colleagues through the CeSIP group.

I want to express my gratitude to my biggest strength: my family. My wife, Ramatu Cornelius, was always there to support me mentally, if not physically, by my side

Acknowledgements

throughout the PhD. I cannot thank my parents enough for their constant support and for inspiring me to dream. In particular, I would like to dedicate this thesis to my daughter, Gift Cornelius, and my Father, Yohanna Pahalson, as a lasting memory!

Finally, I sincerely thank my sponsor, the Tertiary Education Trust Fund (TET-Fund) scholarship board, for sponsoring my PhD. May God richly bless Nigeria and remember the country for good. I appreciate the commitment of Plateau State Polytechnic, Barkin Ladi, Nigeria, to approve my study leave.

Chapter 1

Introduction

1.1 Motivation

The rapid growth of wireless communication technologies has led to an increasing demand for access to the radio frequency (RF) spectrum, creating significant global challenges to address and exploit spectrum scarcity [6] and underutilization. The RF spectrum, a finite and valuable natural resource [7], is used in a wide range of applications, typically spanning 10 MHz to 6 GHz [8]. However, the traditional approach to spectrum management, in which specific frequency bands are licensed exclusively to particular users, has proven to be inflexible and inefficient. This static allocation results in large portions of the spectrum being underutilized and remaining vacant most of the time [9, 10], while other parts of the RF spectrum experience severe congestion.

As wireless systems increasingly integrate with computing technologies for entertainment, information, and multimedia services, competition for spectrum continues to intensify [11, 12]. Recognizing the inefficiencies in conventional spectrum allocation, regulatory bodies such as the Federal Communications Commission (FCC) in the United States and the Office of Communications (Ofcom) in the United Kingdom have introduced policies to allow unlicensed devices to opportunistically access underutilized frequency bands, particularly those in the television (TV) broadcast spectrum [13, 14]. Measurements in e.g. [1] — illustrated also in Fig. 1.1 — have shown that spectrum

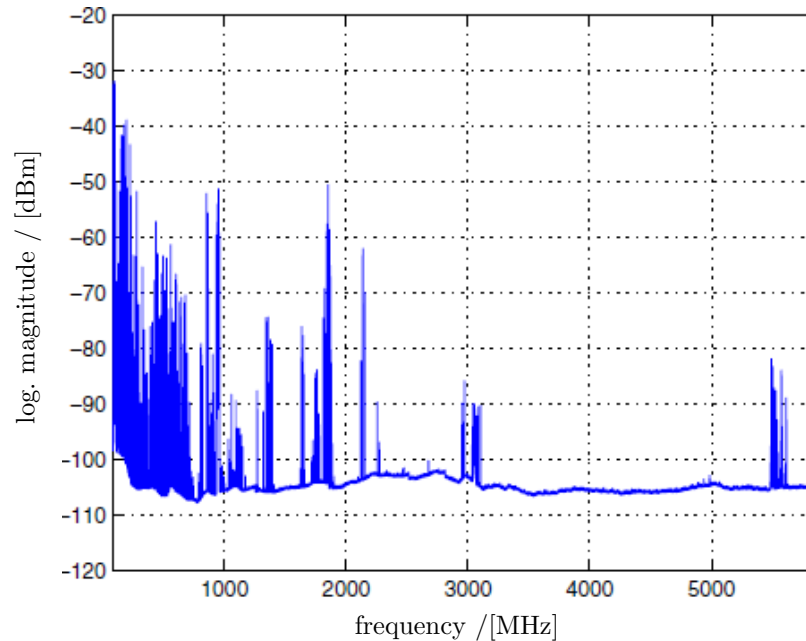


Figure 1.1: Example of locally measured radio spectrum occupancy from 0–6 GHz, showing received power (dBm) versus frequency and integrated over a 24h time window in an urban environment (Singapore) [1].

utilization in the 0 to 6 GHz range varies widely, from as low as 15% to as high as 85% with variation in time [15, 16], suggesting significant room for improvement in spectral efficiency. Various studies highlight substantial unused resources in frequency, time, and space [13, 17, 18]. Cognitive (CR) aims to utilize underutilized spectrum resources by opportunistically reusing unused spectrum in various domains [19–21], particularly by permitting access to additional non-legacy users, which are generally referred to as secondary users (SUs).

To address these issues, the IEEE formed the 802.22 Working Group to develop a standard for wireless regional area networks (WRANs) [22, 23], which provides the required specifications for using for operation in the TV white space spectrum. CR-enabled WRANs detect the presence of Primary Users (PUs) to avoid interference and provide broadband access in rural and underserved areas [24–26], with performance comparable to digital subscriber lines (DSL) or cable [27–29]. According to the IEEE

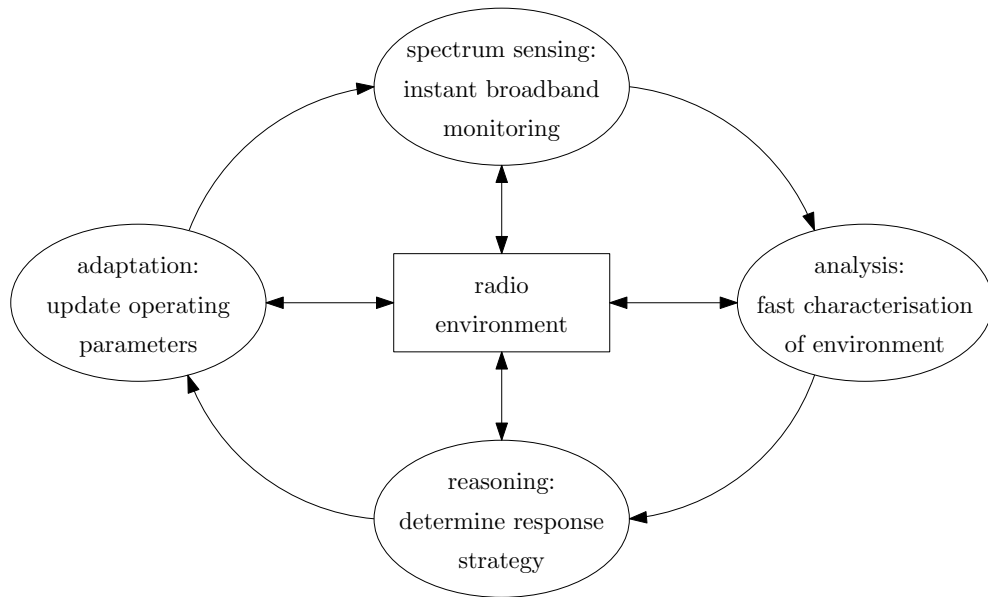


Figure 1.2: Cognitive radio capabilities, after [2].

802.22 standard, for example secondary users in the TV white space bands are required to reliably detect TV and wireless microphone signals and vacate the channel within 2 seconds of detection, thereby ensuring adequate protection of incumbent systems.

CR [2] is an adaptive wireless communication paradigm that enables unlicensed users, also known as Secondary Users (SUs) or cognitive users (CUs), to access licensed spectrum opportunistically, without interfering with the operation of incumbent PUs [19, 30]. CR technology employs intelligent software-driven algorithms to observe, learn from, and adapt to the RF environment in real time [31], as shown in Fig. 1.2. Its key capabilities, observation, adaptability, and intelligence enable dynamic spectrum access (DSA), allowing radios to make decisions based on spatiotemporal spectrum availability.

The concept of CR communications [32] was first introduced in [2] to improve spectrum efficiency by exploiting unused or underutilized frequencies, often referred to as 'spectrum holes' or 'white spaces' [33, 34]. The spectrum resource available for SUs is known as a spectrum hole [35]. Fig. 1.3 conceptually illustrates how DSA enables SUs to identify and utilize unused frequency bands. Through DSA technology, CR

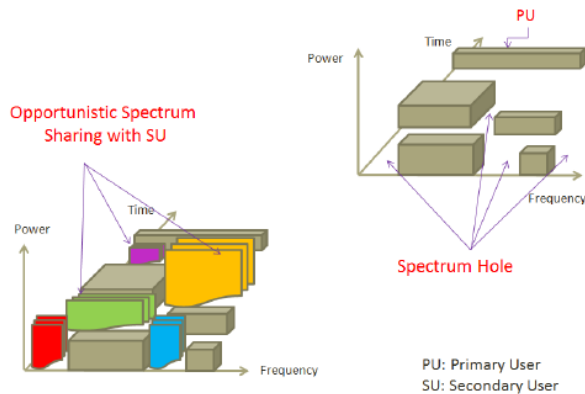


Figure 1.3: Spectrum band with spectrum holes or white spaces [3]

systems aim to maximize the utilization of available spectrum resources [3, 19] while minimizing interference [2, 19, 27, 36–38]. These technologies have shown great potential for a range of applications, including next-generation wireless communication systems, commercial broadband services, and military communications [39–41].

Despite their promise, CR systems face numerous challenges. The most fundamental requirement is that the SUs must vacate the spectrum when a PU becomes active [42]. Achieving this requires highly accurate and low-latency sensing mechanisms. Moreover, ensuring reliable communication under varying noise conditions, designing intelligent interference management techniques, and making real-time decisions in dynamic environments remain open research problems [43]. These challenges underscore the need for advanced sensing, learning, and adaptive decision-making techniques to realize the potential of CR networks.

The advancement of CR systems from theory to practice is based on four main areas: environmental awareness, intelligent decision-making, secure operation, and integration of real-time systems. While significant progress has been made, many of these challenges are exacerbated in non-stationary or contested wireless environments, where uncertainty and limited information are the norm.

To address these challenges, this research tackles three key problems in CR systems aimed at enhancing adaptive and intelligent wireless communication:

- a) *Detection of Weak Transient Signals.* This work develops methods to reliably identify short-duration, low-power transmissions in noisy and dynamic environments for accurate PU detection.
- b) *Design of Targeted Jamming.* This research introduces a judicious jamming approach in order to suppress undesired users. This method operates effectively in mixed-user environments without disrupting authorized users, thereby improving interference management and security.
- c) *Estimation of Time-Varying Noise Power Spectra.* To support adaptive sensing, this work proposes techniques for real-time estimation of noise characteristics. This can help to identify windows of opportunity when e.g. weak PU signals may be detected, or may allow for more efficient identification and exploitation of spectrum holes or white spaces [33].

Together, these contributions address core issues in signal detection, adversarial robustness, and environmental estimation, advancing the reliability and spectral efficiency of CR systems operating in complex wireless environments.

By addressing these key issues, this work contributes to the development of more agile, reliable, and spectrum-efficient CR systems. The proposed methodologies are based on principles from signal processing and statistics, resulting in a robust and extensible framework that advances the capabilities of next-generation wireless cognitive communication technologies.

1.2 Contributions of Thesis

To the best of our knowledge, the novel contributions reported in this thesis are:

- In order to verify a broadband subspace detection method likelihood ratio test (LRT) and generalised likelihood ratio test (GLRT) approaches are formulated using covariance terms derived from polynomial matrix methods [44, 45]. A comparison between this subspace technique and the LRT/GLRT leads to an inves-

tigation and justification why simple energy-based methods can outperform LRT and GLRT-based methods despite the latter requiring additional system information [46].

- In order to design jamming signals for broadband arrays that can target emerging sources or non-stationary users [47], this thesis introduces a time-reversal technique that leverages channel reciprocity to detect transient broadband sources from their emissions. Such jamming is performed while ensuring that existing users are protected by spatial nulls utilizing broadband beamforming techniques.
- For the estimation of noise power spectral density in a time-varying scenario based on a single noise source and across a sensor array [48], a space-time covariance estimation approach exploits an optimal support estimation which minimises the estimation error. This can be combined with a low-rank approximation to further enhance performance. The techniques are assessed and compared to the classical Welch method of power spectral density estimation.

1.3 Overview of Study

In Chapter 2, we review the literature and the essential background necessary to understand current methods in signal detection, and set the stage for broadband multiple-input multiple-output (MIMO) techniques based on polynomial matrix formulations and factorisations. This forms the basis on which the contributions Chapters 3 to 5 are built to address one of the key problems stated in Sec. 1.1, with Fig. 1.4 illustrating how these chapters interlink.

Chapter 3 investigates the problem of broadband transient signal detection via polynomial matrix subspace methods. This builds on previous work, which is reviewed and for which a comprehensive framework is provided. This approach works particularly well in the presence of stronger users, i.e. when aiming to detect weak signals. We introduce an LRT and GLRT method to understand how well the subspace method works against statistically optimal approaches, and provide some insight into the ben-

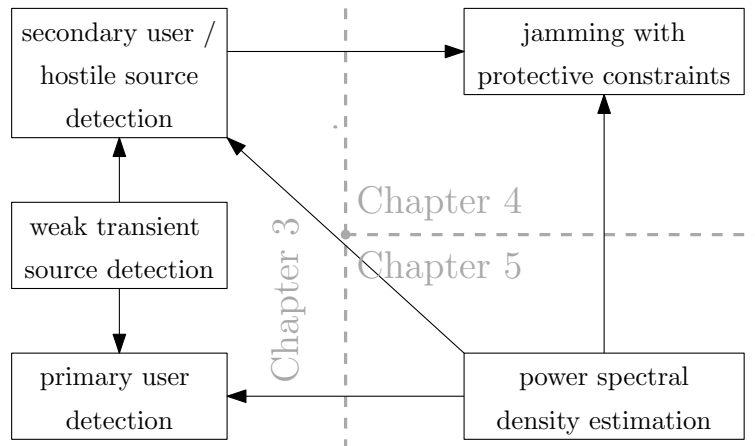


Figure 1.4: Links between research presented in the different core chapters of this thesis.

efits of the subspace approach by applying LRT and GLRT to both measurement data as well as data projected onto a broadband subspace. As depicted in Fig. 1.4, this approach can in principle be utilized to detect emerging primary users, or potentially hostile sources as in the originally proposed application of this broadband subspace approach. The chapter demonstrates that for these cases, a simple energy detection applied to the subspace method can perform close to or, due to enhanced conditioning, even outperform, LRT and GLRT implementations, even though the latter methods require more knowledge of the environment.

In Chapter 4, the design of jamming signals for broadband arrays is addressed in the presence of known stationary users. Two scenarios are considered: when the transmission paths to hostile sources are known and when the sources are unknown but have been previously detected. In this first case, we extend MIMO downlink techniques to the broadband setting using analytic singular value decomposition (SVD). In the second case, exploiting channel reciprocity, we apply a time reversal method to focus the interference on the target user, while aiming at null interference for known desired users. This method relates to the investigation in Chapter 3 in using the weak transient signal received for time reversal, as indicated in Fig. 1.4, and can be used to suppress secondary users, i.e. for aggressive forms of spectrum policing. We compare the

performance and robustness of the time-reversal approach with that of the well-known channel beamforming case through simulations. The results show that time reversal is effective when the reverse signal has sufficient SNR but degrades under high-noise conditions. Beamforming with full channel knowledge provides an upper performance bound and offers insight into time-reversal behaviour in more complex scenarios. The chapter provides a review of the signal detection background, presents interference design methods, and concludes with an evaluation and discussion of the key findings.

Chapter 5 addresses a key problem within Chapters 3 and 4: finding a window of opportunity when, in a fluctuating noise environment, the noise power is sufficiently low, i.e. the SNR sufficiently benign, to detect weaker environmental signals such as transient source and to record sequences that can be employed for time-reversal-based jamming. The simplified problem in this chapter is to estimate the PSD of noise originating from a single source and measured across an array of sensors. We employ a basis expansion model (BEM) for this scenario, from which the time-varying ground truth PSDs. We then explore and compare several data-driven estimation methods. As a baseline, the standard Welch method is applied. Beyond this, a framework for space-time covariance estimation is proposed. Recognizing that empirical covariance matrices derived from finite data are subject to perturbation, we introduce two enhancements: (1) optimal lag support truncation using a recently proposed criterion and (2) a rank-one approximation derived via analytic eigenvalue decomposition (EVD). The chapter also provides the necessary theoretical background to support these approaches. Through examples and simulations, we examine how key parameters, such as the number of sensors and properties of the BEM, affect estimation performance.

Chapter 6 summarises the research presented in this thesis and suggests potential routes that arise for future work.

Chapter 2

Background

2.1 Introduction

This chapter introduces key concepts and contributions to the research presented in this thesis. Some of the subsequent chapters will contain separate reviews, but there are two central aspects to the thesis for which some explicit background is provided below. This includes, firstly, the discussion of recent efforts to detect PU signals within an RF band in the context of CR communications; to this end, Sec. 2.2 focuses on energy detection methods.

Secondly, this chapter motivates the analysis of multiple-antenna CR systems using broadband techniques based on polynomial matrix algebra and provides some background on these techniques. Here, Sec. 2.3 reviews broadband description of the channel matrix describing a MIMO system, i.e., co-located antennas (compact array at a single receiver), the required broadband second order statistics, and discusses when such broadband descriptions need to be taken into account for problem formulations instead of the simpler narrowband case. Both the channel matrix and the statistics, expressed by the space-time covariance matrix, lead to a polynomial matrix notation with a z -transform. In order to solve such broadband problem formulations, matrix decompositions are required for such polynomial matrices. A first factorisation, the parahermitian matrix EVD applied to a space-time covariance matrix, is reviewed in

Sec. 2.4. This includes the existence of the EVD of parahermitian matrices, some of its properties such as strong decorrelation and its application for subspace decompositions, and relevant algorithms. Sec. 2.5 focuses on the polynomial matrix SVD, including the analytic SVD, its relation to the analytic EVD, and related algorithms and applications. Sec. 2.6 concludes with a summary of the chapter.

2.2 Energy Detection-Based Spectrum Sensing

In CR systems, SUs must reliably determine whether PUs occupy a frequency band before accessing the spectrum. There must also be a mechanism to sense whether a potential PU is entering frequency bands where SUs are currently active. Consequently, spectrum sensing is a fundamental operation whose performance directly affects both the level of interference imposed on PUs and the overall spectral utilisation efficiency [49]. Accurate detection of primary transmissions are therefore essential for effective coexistence between PUs and SUs. Generally, the task of spectrum sensing involves several key sub-tasks [50], including the detection of spectrum holes, spectral resolution of each detected hole, estimation of the spatial directions of incoming interferers, and signal classification. A wide range of spectrum-sensing techniques has been developed for CRs, forming a fundamental component of both standalone CR operation and cooperative sensing in CRNs, to identify available frequency bands. However, reliable detection of very weak PU signals remains a significant challenge, particularly under uncertainty of the noise, fading, and limited sensing time, while also requiring low computational complexity and implementation cost. Among the various approaches, energy detection has attracted significant attention due to its simplicity and the fact that it does not require prior knowledge of the PU's signal structure. More broadly, spectrum sensing techniques can be classified based on the bandwidth of the target frequency range into narrowband and wideband sensing. This distinction is fundamental, as it directly influences algorithm design and problem formulation.

In narrowband sensing, the CR system focuses on a single frequency band, allowing the use of relatively low-complexity techniques such as energy detection, cyclostation-

ary feature detection, and matched filtering. In contrast, wideband sensing involves the simultaneous analysis of multiple frequency bands, necessitating more advanced approaches, including multiband joint detection, compressive sensing, and Fast Fourier Transform (FFT)-based spectral analysis.

However, wideband sensing introduces several challenges, including high sampling rate requirements, increased computational complexity, and the need for fine spectral resolution. Furthermore, classical detection techniques—primarily developed for narrowband scenarios—are not directly applicable to wideband contexts without modification, often requiring enhanced or hybrid frameworks.

Understanding the distinction between narrowband and wideband sensing is therefore essential for a comprehensive literature review. It provides a structured basis for evaluating the applicability of different sensing techniques and helps define the scope of analysis, particularly in relation to energy detection and its advanced variants.

2.2.1 Performance Criteria

Ahead of reviewing a number of methods for energy detection, first, a number of performance criteria are defined. This includes parameters relating to, e.g., probability of detection (P_D), probability of false alarm (P_{FA}), detection time, computation cost, and CSI.

Probabilities of Detection and of False Alarm. Energy detection often involves detecting the difference in energy or power levels between cases with and without a PU. This closely relates to hypotheses of a PU being absent or present. As an example, Fig. 2.1 shows the probability density functions (PDFs) of signal energy measurements x given that a PU is present or absent, denoted as $p(x|PU)$ and $p(x|\overline{PU})$, respectively. Based on the PDF of energy measurements with a PU present and an arbitrary decision threshold ϑ (as indicated by the dashed line in Fig. 2.1), we define a probability of missed detection, P_M ,

$$P_M = \int_{-\infty}^{\vartheta} p(x|PU)dx . \quad (2.1)$$

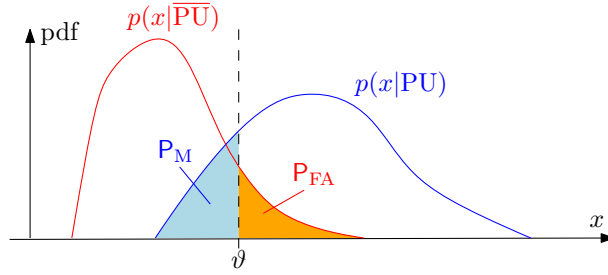


Figure 2.1: Examples PDFs of energy measurements x , $p(x|\text{PU})$ and $p(x|\overline{\text{PU}})$; ϑ denotes a decision threshold, which defines the probabilities of missed detection, P_M , and of false alarm, P_{FA} .

Its complement defines the probability of detection,

$$P_D = 1 - P_M . \quad (2.2)$$

A third metric is the probability of false alarm,

$$P_{\text{FA}} = \int_{\vartheta}^{\infty} p(x|\overline{\text{PU}}) dx . \quad (2.3)$$

Ideally, in applications we would like to operate with energy measurements (or other criteria) where the P_D is as high as possible, i.e. $P_D \rightarrow 1$, and the P_{FA} is as low as possible, i.e. $P_{\text{FA}} \rightarrow 0$.

Separability of Distributions. Setting the decision threshold ϑ therefore results in a trade-off between P_D and P_{FA} . In order to measure how well two distributions such as the ones in Fig. 2.1 separate, a receiver operating characteristic (ROC) draws P_D versus P_{FA} as a function of the threshold ϑ . The area under the ROC curve then provides a threshold-independent measure of separability of the two PDFs [51].

Computational Complexity. The computational complexity of a method is important as it determines whether it is technically feasible to run on a suitable computational platform. Computational complexity can be measured e.g., via multiply-accumulate (MAC) operations, which are the main signal processing operations for digital filtering, such as averaging or discrete/fast Fourier transforms, floating point operations

(FLOPS), or computation time. These can yield different results, since, e.g., MACs do not account for overheads such as memory moves.

Accuracy/Robustness. The accuracy and robustness of an algorithm are influenced not only by the signal-to-noise ratio (SNR) but also by implementation-specific factors such as finite word length effects, which introduce quantization and rounding errors. These effects become particularly critical in ill-conditioned problems, where numerical operations such as matrix inversion may significantly amplify small perturbations.

Time to Decision. Related to the computation time and accuracy is how long it takes to reach a decision, e.g. in order to detect the presence of a PU. This may depend on the computational complexity of a method, but also on the amount of data that needs to be acquired or buffered if e.g. averaging over time is performed. Performance criteria usually are interdependent, and the time to decision may have to be traded off against the accuracy of an approach.

2.2.2 Energy Detection Methods

Energy detection is one of the most widely adopted spectrum sensing techniques in CR due to its computational complexity, low power consumption, very short sensing time, and generic implementation. Although recent studies such as [52, 53] investigate practical implementations and performance enhancements of energy detection under various channel conditions, they do not constitute foundational contributions. The theoretical basis and early applications of energy detection in CR systems can be traced to seminal works such as [54, 55], which established its performance over fading channels and its applicability to opportunistic spectrum access. These contributions, along with early CR frameworks introduced by [19], form the primary justification for the widespread use of energy detection, while later works primarily focus on refinements and implementation aspects. Unlike spectrum sensing methods that use matched filters [56], energy detection does not require prior knowledge of the PUs' signal structure. However, knowledge of some signal statistics, such as the noise variance, is crucial for accurate detection. Energy detection often struggles to distinguish the PU signal from

noise at low SNR, leading to a high P_{FA} . This can reduce detection performance at low SNR, increase power consumption, and render the technique unsuitable, e.g., low-SNR techniques such as spread-spectrum methods [57]. In operation, the SU monitors the spectrum allocated to the PU and transmits data to its receiver as long as it detects no PU transmission.

In recent years, numerous studies have focused on spectrum sensing and energy detection methods within CRNs. Articles [58–67] highlight the improvement of detection performance while minimizing disruptions caused by SUs for licensed operators. The authors in [58] introduce a new generalized spectral detection technique called constant energy, which enables the quick and reliable detection of all PU signals. They utilize theoretical analysis and computational simulations to evaluate the performance of this approach. The results demonstrate that the proposed method achieves higher detection probabilities and faster detection times than conventional energy (i.e., classical threshold-based energy comparison method used in CRNs to detect primary users without prior knowledge of their signals) detection, with only a slight increase in computational complexity. Spectrum sensing schemes, despite their popularity, have notable limitations, as summarized in [57]. Energy detection is cost-effective but highly sensitive to noise, resulting in poor detection at low SNR and high false-alarm rates. Cyclostationary feature detection enhances performance under low SNR but requires significant computational resources and longer sensing times. Matched filter detection is optimal when the PU signal is known, though this increases complexity and costs. Covariance-based methods are robust to noise without requiring knowledge of the PU signal. Still, they perform poorly with uncorrelated signals and typically require longer sensing times and more computational power.

The study presented in [59] demonstrates the effectiveness of global adaptive threshold estimation, wherein sensing statistics collected from multiple SUs are aggregated to compute a network-wide detection threshold. Such cooperative approaches enhance detection reliability by mitigating the effects of fading and shadowing. However, this framework is developed under the assumption of a stable (stationary) environment,

where the statistical properties of the received signal and noise—particularly noise variance and signal power—remain constant or vary negligibly over time. Under these stationary conditions, threshold adaptation based on globally estimated statistics can be performed reliably. In contrast, the present work addresses transient and non-stationary scenarios, characterized by time-varying signal, interference, and noise statistics due to mobility, dynamic spectrum access, or intermittent jamming. In such environments, the assumption of statistical stability no longer holds, rendering global threshold estimation potentially outdated or inaccurate. Rather than emphasizing threshold adaptation, the proposed approach exploits the relative temporal behavior of the received signal, thereby reducing sensitivity to noise uncertainty and abrupt environmental changes. Consequently, a direct comparison with global adaptive-threshold-based energy detection methods is not straightforward, as the underlying statistical assumptions differ fundamentally. Future work may explore hybrid frameworks that incorporate cooperative (global) sensing statistics while maintaining robustness under non-stationary conditions.

In [60], a novel spectral detection strategy is proposed that emphasizes both energy- and spectrum-efficient sensing. The method performs wideband sensing to identify vacant sub-bands within a PU’s licensed spectrum and subsequently monitors energy variations to detect the PU’s reappearance. Compared with conventional periodic wideband sensing and traditional energy detection schemes, the proposed algorithm reduces sensing duration and processing overhead, thereby lowering the energy consumption of secondary users. This reduction in sensing overhead limits unnecessary interference with both PUs and other SUs while enabling more frequent data transmission, which improves throughput without compromising the reliable protection of licensed users. The authors evaluate their approach against conventional spectrum sensing techniques through theoretical analysis and CRN simulations, demonstrating improved channel detection performance and spectrum utilization efficiency. Furthermore, the study in [61] provided a comprehensive survey of recent advances in spectrum detection, examining the effectiveness and limitations of narrow-band and wide-band

spectrum detection techniques, as well as the challenges associated with their implementation. However, these works primarily focus on the mathematical models that underpin spectrum sensing metrics, which limits insight into how such methods perform under practical operating conditions. In particular, many existing studies assume idealised conditions and do not adequately account for non-ideal factors such as hardware impairments, noise uncertainty, non-stationary interference, dynamic jamming, and spatially varying channels. These factors can significantly degrade sensing performance and are critical in practical systems. As a result, the robustness and scalability of these techniques remain insufficiently explored in realistic scenarios, especially in MIMO and beamforming-based systems, where additional complexities such as channel estimation errors, antenna coupling, and beam misalignment may arise.

Window-based energy detection has been widely explored to improve signal detectability in challenging environments and for bursty transmissions. In cooperative sensing scenarios, window-based energy detection has been shown to significantly enhance detection performance by exploiting spatial diversity. For instance, in rural propagation environments, window-based energy detection was evaluated alongside a localization approach based on double-thresholding and forward-consecutive-mean excision, with both techniques estimating individual detection probabilities [62]. Simulation results demonstrated that window-based energy detection consistently outperformed the double-thresholding localization method. At the same time, cooperation among sensing nodes extended the signal detection range by up to five times, depending on system parameters such as signal bandwidth, decision rules, and the number of cooperating nodes.

Beyond cooperative window-based processing, energy detection techniques have also been extended to address practical receiver impairments. In this context, the Wavelet-based energy detection spectrum-sensing technique was introduced in [64], employing double-resolution spectral cooperative detection and a high-frequency harmonic-rejection mixer to mitigate harmonic mixing. The proposed approach achieved substantial harmonic rejection, making it suitable for energy-efficient ultra-wideband CR

systems.

Complementary to cooperative sensing gains, window-based energy detection has also been investigated for detecting burst signals without prior knowledge of their structure. By employing short observation windows, an energy sensing scheme was proposed that enables reliable detection of bursty signals while maintaining a prescribed P_{FA} [63]. The analysis identifies the optimal window length that maximizes captured burst energy and characterizes the resulting detection performance (P_{M}) and energy efficiency, demonstrating clear performance improvements over conventional energy detection approaches.

Meanwhile, in [68], the author presents a theoretical formulation of a spectral detection technique based on the standard condition number (i.e., the matrix condition number) within an asynchronous CRN. The study examines how asynchronous scenarios—where the SU must learn or estimate the PU communication timing—impact the spectral detection performance. The proposed analytical framework for cooperative asynchronous spectrum detection does not assume synchronization among the SUs; instead, asynchrony is defined relative to the timing relationships among the SUs and the PU.

Reference [65] investigated energy detection-based spectrum sensing to determine the presence of a PU. The study analyzed the P_{D} and the P_{FA} for an individual sensing node (SU) operating over an AWGN channel. The results showed that P_{D} is strongly influenced by the energy detection decision threshold and improves with increasing SNR. Additionally, employing different modulation schemes across both fading and non-fading channels was shown to enhance detection performance, while more extended observation intervals further improved sensing reliability.

Extending conventional energy detection, [67] evaluated the performance of CRNs using an enhanced (generalized) energy detector under various fading channel models and different relative velocities of SUs. The enhancement is achieved by introducing an arbitrary power parameter that generalizes the conventional energy detector by raising the received signal energy to a tunable exponent. Simulation results showed

that the optimal value of this parameter depends on both SU mobility and the number of cooperating SUs, thereby significantly affecting detection performance.

Several studies have investigated adaptive threshold-based energy detection techniques to improve spectrum sensing performance, particularly in low SNR environments. The works in [69–73] highlight various adaptive strategies to overcome the limitations of conventional fixed-threshold energy detection approaches. In [74], a modified dual-threshold cooperative energy detection scheme was proposed to mitigate PU emulation attacks. The study reports a significant reduction in the impact of such attacks while maintaining reliable detection performance.

A subset of these studies focus on optimizing the trade-off between detection probability and false alarm rate. In [69], the authors proposed a method to identify an optimal detection threshold at low SNR that simultaneously satisfies $P_{FA} \leq 0.1$ and $P_D \geq 0.9$. Unlike traditional constant false alarm rate and constant detection rate approaches [75], the proposed method aims to minimize the probability of error while maximizing throughput across varying SNR levels.

Another research direction addresses the uncertainty in adaptive threshold design due to noise. In [71], an adaptive spectrum energy detection approach was developed under AWGN assumptions, with performance evaluated in terms of P_D and P_{FA} . The results indicate that the detection probability increases with SNR, whereas expanding the bandwidth factor reduces detection performance. Furthermore, the same study introduced an adaptive threshold computed from a noise uncertainty factor estimated via sliding-window resampling of the received signal, demonstrating improved robustness compared to conventional constant-threshold energy detection.

In [72], an adaptive multi-stage threshold model was presented to enhance energy detection performance at low SNR. The approach focuses on maximizing P_D while maintaining constraints on the false alarm rate by determining appropriate thresholds at each detection stage. The reported results show improved utilization of spectrum holes compared to traditional energy-detection schemes.

From an algorithmic perspective, the three-event energy detection algorithm pro-

posed in [73] incorporates an adaptive detection threshold approximated by the Newton method, thereby ensuring convergence to an optimal decision threshold. Simulation results demonstrate that this approach outperforms conventional energy detection across various wireless network environments.

A summary of the above energy-based detection for spectrum sensing methods for CR applications is provided in Table 2.1.

2.2.3 Cyclostationary Feature Detection

Cyclostationary feature detection (CFD), introduced by [76], is a signal detection technique that utilizes periodic statistical properties inherent in communication signals. These properties arise from factors such as carrier frequencies and modulation schemes, leading to variations in statistical measures such as the mean and autocorrelation function. Unlike stationary noise processes, communication signals exhibit periodic behavior, enabling CFD to effectively distinguish between noise and structured signals, even in low SNR conditions.

In narrowband CR systems, the received discrete-time signal can be expressed as

$$y[n] = h \cdot x[n] + w[n], \quad (2.4)$$

where $x[n]$ denotes the transmitted PU signal, h represents the channel gain, and $w[n]$ is AWGN. A signal is cyclostationary if its statistical moments, like mean and autocorrelation, show periodicity over time [77, 78]. Practical examples include sinusoidal carriers, pulse trains, and spreading sequences. These periodic structures are crucial for cognitive radio, allowing for reliable detection of PU signals. Cyclostationarity refers to the correlation of a signal with its frequency-shifted versions [76, 79], quantified by the cyclic autocorrelation function (CAF) defined as

$$R_y^\alpha[\tau] = \mathcal{E}\{y[n]y^*[n - \tau]e^{-j2\pi\alpha n}\} \quad (2.5)$$

where α denotes the cyclic frequency and τ represents the time lag. The spectral rep-

Table 2.1: Summary of energy detection

Ref.	Method	Complexity	Accuracy	Speed
[52, 53]	Classical energy detection (ED) without prior PU knowledge	Very low	Poor at low SNR; sensitive to noise uncertainty; high P_{FA}	Very fast
[58]	Constant Energy generalized spectral detection	Low-moderate	Higher P_D than conventional ED	Faster than classical ED
[59]	Adaptive threshold ED (local vs global)	Moderate	Global adaptive methods outperform local ones	Moderate
[60]	Energy- and spectrum-efficient ED with wide-band sensing	Moderate	Improved channel detection and utilization	Faster sensing than conventional ED
[62]	Window-based ED and double-threshold localization (cooperative)	Moderate	Window-based ED yields higher P_D	Moderate
[63]	Short-window ED for burst signal detection	Low	Improved P_D and reduced P_M	Very fast
[64]	Wavelet-based ED with harmonic rejection	High	High detection accuracy in ultra-wideband CR	Moderate
[65]	Threshold-based ED under AWGN	Very low	P_D improves with SNR and observation length	Very fast
[67]	Enhanced ED under fading and SU mobility	Moderate	Improved robustness; sensitive to SU velocity	Moderate
[69]	Optimal adaptive threshold ED at low SNR	Moderate	High P_D (≥ 0.9) with controlled P_{FA}	Moderate
[71]	Adaptive threshold ED using noise uncertainty estimation	Moderate	Outperforms constant energy detection under noise uncertainty	Moderate
[72]	Multi-stage adaptive threshold ED	Moderate-high	Significant P_D improvement at low SNR	Moderate
[73]	Three-event ED with Newton-based adaptive threshold	Moderate-high	Higher detection accuracy than traditional ED	Moderate
[74]	Dual-threshold cooperative ED for PU emulation attack mitigation	High	Excellent robustness against PU emulation attacks	Moderate

resentation of this function, known as the cyclic spectral density or spectral correlation function (SCF), is obtained by taking the Fourier transform, such that

$$S_y(e^{j\Omega}, \alpha) = \sum_{\tau=-\infty}^{\infty} R_y^\alpha[\tau] e^{-j\Omega\tau}, \quad (2.6)$$

where f is the spectral frequency. The presence of distinct peaks in $S_y(e^{j\Omega}, \alpha)$ at non-zero cyclic frequencies ($\alpha \neq 0$) indicates cyclostationarity and, consequently, the presence of a structured communication signal. In contrast, AWGN does not exhibit such features, as its spectral correlation is theoretically zero for all non-zero cyclic frequencies.

CFD operates as a first-order or second-order detector based on statistical properties, with second-order detection being more common due to its reliance on the periodicity of the autocorrelation function. Higher-order cyclostationary techniques improve robustness in challenging environments but add computational complexity. CFD excels at detecting signals at low SNR, distinguishing structured signals from noise by their signal-specific periodicities. However, it requires significant computational resources, longer observation times, and often depends on prior knowledge of signal parameters, which may be unavailable in dynamic conditions.

2.2.4 Matched Filter Detection

Matched filter detection (MFD) maximizes output SNR in additive noise and is the optimal method for detecting known deterministic signals in Gaussian noise [56, 80]. It plays a vital role in CR systems by accurately determining spectrum occupancy using prior knowledge of PU signal characteristics. The MFD scheme enables SUs to demodulate signals by requiring knowledge of PU signaling characteristics such as frequency, modulation type, bandwidth, and frame structure. It is most effective with pre-known PU patterns, such as pilot signal, preamble, etc., to assist synchronisation, signal detection, and other purposes [81]. Wideband matched filter techniques enable multiband CR to dynamically identify spectral opportunities by correlating received

signals with PU patterns.

MFD differs from energy detection and CFD by requiring precise knowledge of the transmitted PU waveform. It uses a matched filter for correlation with a known reference template, maximizing output SNR and achieving optimal detection performance in ideal conditions. The received discrete-time signal is modelled as in (2.4), where the matched filter output $y_{\text{MF}}[n]$ is obtained by convolving the received signal with the filter's impulse response, expressed as

$$y_{\text{MF}}[n] = \sum_{\nu=-\infty}^{+\infty} h[n-\nu]y[\nu], \quad (2.7)$$

where the impulse response $h[n]$ is designed as a time-reversed and conjugated version of the known PU signal:

$$h[n] = s^*[T-n], \quad (2.8)$$

with $s[n]$ representing the reference PU signal and T its duration. In practical implementations, the received signal is digitized using an analog-to-digital converter (ADC) and then correlated with stored pilot sequences of the PU signal. The matched filter output acts as a decision statistic, compared to a predefined threshold for binary hypothesis testing to determine the presence of the PU signal.

The matched filter maximizes output SNR and requires fewer samples for a desired detection probability compared to non-coherent methods like energy detection. Specifically, the number of required samples scales proportionally to $\mathcal{O}(1/\text{SNR})$, whereas energy detection typically requires $\mathcal{O}(1/\text{SNR}^2)$ samples [82]. This property makes MFD particularly attractive in low SNR environments.

MFD offers optimal performance but has key limitations, primarily the need for complete and accurate prior knowledge of PU signal parameters, which isn't always available in dynamic environments. Mismatches in timing, frequency, or phase can degrade detection. Additionally, in heterogeneous scenarios with multiple PU signal types, the need for multiple matched filters increases computational complexity and power consumption, making MFD less suitable for energy-constrained devices. MFD

optimizes performance by maximizing output SNR through coherent detection, making it effective with accurate prior knowledge of the PU signal. However, its reliance on precise signal information, sensitivity to parameter mismatches, and high implementation complexity limit its practical use in CR environments.

2.2.5 Covariance-Based Detection

A covariance-based feature detection scheme identifies the presence of a PU signal using singular value decomposition (SVD) and the sample covariance matrix of the received signal $y[n]$. The statistical covariance matrices of the received signal and noise differ, allowing for the differentiation of the desired signal from noise [83, 84]. In an AWGN channel, the noise samples correlate with zero in different time instances, while the signal samples exhibit a positive correlation if the duration of the data symbol exceeds the time separation [85, 86]. The eigenvalues of the covariance matrix $R_y(M)$ are computed via a singular value decomposition (SVD), and the ratio of the maximum eigenvalue to the minimum eigenvalue can be calculated using random matrix theory [87, 88]. This ratio is compared to a predetermined threshold to assess the presence of the primary signal. The sample covariance matrix of $y[n]$ is estimated using:

$$\hat{\mathbf{R}}_y = \frac{1}{M} \sum_{n=P-1}^{P-2+M} \hat{\mathbf{y}}[n] \hat{\mathbf{y}}^H[n], \quad (2.9)$$

where $\hat{\mathbf{y}}(n) \in \mathbb{C}^K$ is the received signal vector, M denotes the number of samples used for averaging, and P defines the starting index of the observation window (e.g., related to smoothing or subarray selection). An analysis of covariance matrix-based detection reveals that the CoFD scheme performs poorly in fast-varying fading channels compared to slower ones. Increasing the smoothing factor and the correlation in the decision metric improves the detection rate. This method enhances spectrum sensing in CRNs and is incorporated into the IEEE standard 802.11af for TV white space usage. Its threshold value is independent of SNR, ensuring robustness against noise uncertainty without prior knowledge of the primary signal, noise, or channel. Additionally, a cost-

effective mean-square extreme eigenvalue method has been proposed for blind primary signal detection in [89].

2.2.6 MIMO-Based Change-Point and Energy Detection

The use of multiple co-located antennas in the CR receiver can significantly enhance spectrum sensing performance by exploiting spatial diversity and array processing gains. These advantages improve detection reliability, spectral efficiency, and energy efficiency, enabling robust operation even in low SNR regimes [90]. In sequential detection settings, multi-antenna processing is particularly valuable, as it improves the reliability of test statistics under short sensing intervals and uncertain channel conditions.

Among multi-antenna spectrum sensing techniques, the generalized likelihood ratio test (GLRT) has emerged as a natural extension of sequential detection frameworks, as it can accommodate unknown signal and noise parameters. GLRT-based approaches that exploit spatial information, such as beamforming and direction-of-arrival (DOA) estimation, have demonstrated superior detection performance [91]. However, their reliance on accurate spatial parameter estimation limits robustness in dynamic environments. More general GLRT formulations developed for adaptive MIMO systems have shown improved resilience to unknown disturbance covariance matrices [92], albeit at the cost of increased hardware complexity and power consumption.

To address CSI uncertainty, several studies have derived LRT for MIMO CR networks under imperfect CSI, providing analytical expressions for performance metrics such as P_{FA} [93]. Bayesian extensions of the GLRT have further improved detection performance in limited-sample multi-antenna scenarios [94], while cooperative GLRT-based sensing schemes have enhanced robustness through spatial diversity [95]. Despite their effectiveness, these methods are primarily designed for batch processing and do not explicitly optimize detection delay, a key consideration in sequential sensing.

Eigenvalue- and subspace-based detection methods constitute another important class of multi-antenna spectrum sensing techniques. By exploiting the structure of the received signal covariance matrix, these methods offer robustness to noise uncertainty

and reduced dependence on CSI. Eigenvalue-based detectors have been shown to outperform classical energy detection in both single- and multi-antenna CR systems [96], while interference-aware subspace methods further improve detection performance by mitigating structured interference [97, 98]. However, the need for reliable covariance estimation often necessitates relatively long observation windows, limiting their applicability in fast sequential detection scenarios.

To overcome the limitations imposed by CSI uncertainty and estimation overhead, CSI-free and low-complexity multi-antenna detection schemes have been proposed. Generalized F-test-based detectors eliminate the need for CSI while providing closed-form performance analysis [99]. Tensor-based detection frameworks extend these ideas to higher-dimensional signal representations and have demonstrated improved detection capability in fading environments [100], though at increased computational cost. Recent work has also emphasized energy efficiency and practical deployment considerations, with two-stage MIMO sensing frameworks reducing energy consumption while enhancing detection performance [101] and weighted eigenvalue detection improving throughput and detection reliability in IoT-oriented multi-user MIMO systems [102]. Additional studies have examined the impact of fading, antenna correlation, and mobility, highlighting the sensitivity of conventional detectors to dynamic operating conditions [103].

The above MIMO techniques for energy and change point detection in the context of CR applications are summarised in Table 2.2.

2.2.7 Discussion

Tables 2.1 and 2.2 collectively reveal the inherent trade-offs among spectrum sensing techniques in CRNs, particularly with respect to computational complexity, detection accuracy, sensing speed, and implementation feasibility. Classical energy detection remains attractive due to its low complexity and fast sensing; however, its performance deteriorates significantly under low-SNR conditions and in the presence of noise uncertainty. Sequential and GLRT-based detectors achieve reduced detection delay and

Table 2.2: Multiple Antennas-Based Spectrum Sensing

Ref.	Method	Complexity	Accuracy	Speed
[91]	GLRT with DOA and beamforming	High	Outperforms classical detectors	Moderate
[92]	Adaptive MIMO GLRT detectors	Very high	High robustness to disturbances	Slow
[93]	LRT under CSI uncertainty	Moderate	Improves with SNR	Moderate
[94]	Bayesian GLRT for multi-antenna CR	High	Superior detection with limited samples	Moderate
[96]	Eigenvalue-based MIMO sensing	Moderate	Better than Energy detection-based methods	Moderate
[99]	MIMO generalized F-test via SVD	Moderate	Accurate without CSI	Moderate
[102]	Weighted eigenvalue detection	Moderate	Improved detection gain and throughput	Moderate
[101]	Two-phase intensive/precise MIMO detection	Moderate-high	Significant P_D improvement	Moderate

improved low-SNR performance by leveraging statistical modelling and prior information. However, their effectiveness is sensitive to modelling inaccuracies and parameter uncertainty.

Multiple-antenna-based sensing techniques provide the highest detection reliability by exploiting spatial diversity and beamforming gain, yet their increased hardware requirements and algorithmic complexity can limit practical deployment in energy and cost-constrained systems. However, when overall focusing less on what is technically feasible and more on what is scientifically possible, a multi-antenna approach utilising LRT or GLRT techniques is advantageous, particularly when it is considered as a performance benchmark.

2.3 Broadband Multiple-Input Multiple-Output Systems Descriptions

2.3.1 Broadband Channel Description

If we assume a CR system that involves potentially several transmitters and receivers, the system between transmit and receive antennas is described as a MIMO system. Transmission should generally be considered as a broadband system if the delay spread of the channel between any pair of transmit and receive antennas exceeds one period of symbols. Thus, channels need to be characterised by their impulse responses. This type of channel is described below.

Given L transmit and M receive antennas, and a channel impulse response $c_{m,\ell}[n]$ between the ℓ th transmit and the m th receive antenna, $\ell = 1, \dots, L$, and $m = 1, \dots, M$. The arising MIMO channel matrix can be compactly represented by a matrix-valued

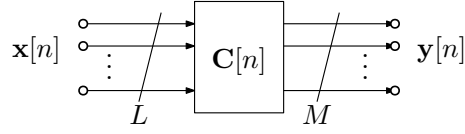


Figure 2.2: Block diagram of MIMO system $\mathbf{C}[n] \in \mathbb{C}^{M \times L}$ with input $\mathbf{x}[n] \in \mathbb{C}^L$ and output $\mathbf{y}[n] \in \mathbb{C}^M$,

impulse response $\mathbf{C}[n] \in \mathbb{C}^{M \times L}$, whose (m, ℓ) -th entry is $c_{m,\ell}[n]$.

$$\mathbf{C}[n] = \begin{bmatrix} c_{1,1}[n] & c_{1,2}[n] & \dots & c_{1,L}[n] \\ c_{2,1}[n] & c_{2,2}[n] & & c_{2,L}[n] \\ \vdots & & \ddots & \vdots \\ c_{M,1}[n] & c_{M,2}[n] & & c_{M,L}[n] \end{bmatrix} \quad (2.10)$$

If L transmit signals $x_\ell[n]$, $\ell = 1, \dots, L$ and M receive signals $y_m[n]$, $m = 1, \dots, M$ are organised into vectors $\mathbf{x}[n]$ and $\mathbf{y}[n]$ such that

$$\mathbf{x}[n] = \begin{bmatrix} x_1[n] \\ x_2[n] \\ \vdots \\ x_L[n] \end{bmatrix}, \quad \text{and} \quad \mathbf{y}[n] = \begin{bmatrix} y_1[n] \\ y_2[n] \\ \vdots \\ y_M[n] \end{bmatrix} \quad (2.11)$$

then the input-output behaviour can be written as

$$\mathbf{y}[n] = \sum_{\nu=0}^{\infty} \mathbf{C}[\nu] \mathbf{x}[n - \nu] = \mathbf{C}[n] * \mathbf{x}[n] \quad (2.12)$$

where $*$ is the short-hand notation for the convolution operation in (2.12). The block diagram illustrates this system in Fig. 2.2. It is assumed that $\mathbf{C}[n]$ only contains causal filters, such that $\mathbf{C}[n] = \mathbf{0} \forall n < 0$ ¹.

When taking the z -transform for $\mathbf{C}[n]$, we obtain a matrix of transfer functions

¹Causality combined with stability will be an important property for $\mathbf{C}[n]$ to be a matrix of analytic functions. Otherwise, causality and stability may be traded off against each other; consider e.g. the causal but unstable $1/(1 + 2z^{-1}) = \sum_{n=0}^{\infty} 2^n z^{-n}$ versus $1/(1 + 2z^{-1}) = z \sum_{n=0}^{\infty} (\frac{1}{2})^n z^n$, which is stable but anti-causal.

$\mathbf{C}(z)$,

$$\mathbf{C}(z) = \sum_{n=0}^{\infty} \mathbf{C}[n]z^{-n}, \quad (2.13)$$

or for short $\mathbf{C}[n] \circ \bullet \mathbf{C}(z)$, which assumes that all channel impulse responses are absolutely convergent, such that $\sum_n |c_{m,\ell}[n]| < \infty$. The resulting transfer functions are then analytic within some region of convergence that includes at least the unit circle. Analyticity implies important properties such as infinite differentiability, i.e., smooth behavior of the functions contained in $\mathbf{C}(z)$. Because it only contains power in z^{-1} , the transfer function matrix $\mathbf{C}(z)$ is generally a power series. If the channel in (2.10) comprises of finite impulse responses such that also $\mathbf{C}[n] = \mathbf{0}$ for $n > N$, then the entries of $\mathbf{C}(z)$ are polynomials, and $\mathbf{C}(z)$ is referred to as a polynomial matrix. The name ‘polynomial matrix’ is often used beyond this narrow definition, and also covers matrices with elements consisting of more general powers or Laurent series.

Example 1 For a randomly created channel $\mathbf{C}[n]$ with $M = L = 2$, Fig. 2.3 shows the channel impulse responses $c_{m,\ell}[n]$ of order 10, i.e. of length $N = 11$. Thus, the impulse responses outside the window $0 \leq n < N$ are zero.

2.3.2 Space-Time Covariance Matrix

In order to describe the statistics of a signal vector, say $\mathbf{x}[n]$ in Fig. 2.2, the space-time covariance matrix $\mathbf{R}[\tau]$ has played a major role in solving various problems related to the processing of broadband signals [104–107]. Given the signal samples $\mathbf{x}[n] \in \mathbb{C}^L$, the statistical expectation operator $\mathcal{E}\{\cdot\}$, and the Hermitian transpose operator $\{\cdot\}^H$, the space-time covariance matrix [107–110]

$$\mathbf{R}[\tau] = \mathcal{E} \{ \mathbf{x}[n] \mathbf{x}^H[n - \tau] \} \quad (2.14)$$

captures both spatial and temporal correlations. In (2.14), $\tau \in \mathbb{Z}$ denotes the discrete lag parameter [107], which generalises the standard narrowband or instantaneous co-

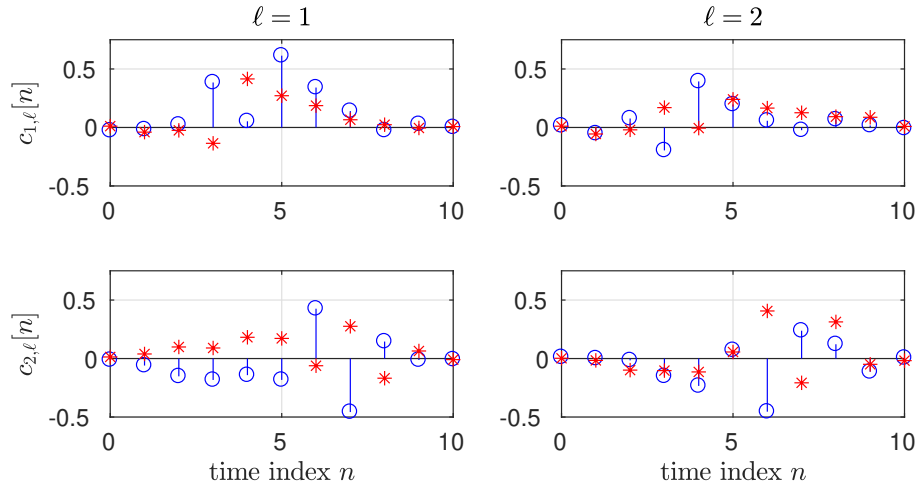


Figure 2.3: Channel $\mathbf{C}[n]$ for Example 1 comprising of channel impulse responses $c_{m,\ell}[n]$, $m, \ell = 1, 2$, with (\circ) and $(*)$ symbolising real and imaginary parts, respectively.

variance $\mathbf{R} = \mathcal{E} \{ \mathbf{x}[n] \mathbf{x}^H[n] \}$ to include temporal correlations; note that for zero lag in (2.14), we have $\mathbf{R} = \mathbf{R}[0]$.

The definition in (2.14) implies that $\mathbf{R}[\tau]$ comprises of cross-correlation functions. In the m th row and μ th column of $\mathbf{R}[\tau]$, we find the element $r_{m,\mu}[\tau] = x_m[n] x_\mu^*[n - \tau]$. Since

$$r_{\mu,m}[\tau] = \mathcal{E} \{ x_\mu[n] x_m^*[n - \tau] \} = \mathcal{E} \{ x_m^*[n] x_\mu[n + \tau] \} = \mathcal{E} \{ x_m[n] x_\mu^*[n + \tau] \}^* \quad (2.15)$$

$$= r_{m,\mu}^*[-\tau], \quad (2.16)$$

the space-time covariance matrix satisfies the parahermitian symmetry

$$\mathbf{R}[\tau] = \mathbf{R}^H[-\tau], \quad (2.17)$$

which generalises the Hermitian property of the narrowband, instantaneous covariance matrix $\mathbf{R} = \mathbf{R}[0] = \mathbf{R}^H[0]$. The property in (2.17) is sometimes also referred to as palindromic symmetry [111]. For the case of $M = 2$ sensors, the space-time covariance

takes the form

$$\mathbf{R}[\tau] = \begin{bmatrix} \mathcal{E} \{x_1[n]x_1^*[n-\tau]\} & \mathcal{E} \{x_1[n]x_2^*[n-\tau]\} \\ \mathcal{E} \{x_2[n]x_1^*[n-\tau]\} & \mathcal{E} \{x_2[n]x_2^*[n-\tau]\} \end{bmatrix} \quad (2.18)$$

$$= \begin{bmatrix} r_{11}[\tau] & r_{12}[\tau] \\ r_{21}[\tau] & r_{22}[\tau] \end{bmatrix} = \begin{bmatrix} r_{11}[\tau] & r_{12}[\tau] \\ r_{12}^*[-\tau] & r_{22}[\tau] \end{bmatrix}. \quad (2.19)$$

The diagonal entries correspond to the autocorrelation functions of each signal in $\mathbf{x}[n]$, while the off-diagonal entries capture cross-correlations between pairs of signals.

When taking the z -transform of the space-time covariance matrix $\mathbf{R}[\tau]$, we obtain the cross-spectral density (CSD) matrix $\mathbf{R}(z)$ $\bullet\text{-}\circ$ $\mathbf{R}[n]$ [108]. Because of (2.17), we find that from (2.17) which establishes the Hermitian symmetry property in the lag domain. Taking the z -transform of $\mathbf{R}[\tau]$, we obtain the cross-spectral density (CSD) matrix

$$\mathbf{R}(z) = \sum_{\tau=-\infty}^{\infty} \mathbf{R}[\tau]z^{-\tau} \quad (2.20)$$

Using the symmetry property $\mathbf{R}[\tau] = \mathbf{R}^H[-\tau]$, we have

$$\mathbf{R}(z) = \sum_{\tau=-\infty}^{\infty} \mathbf{R}^H[-\tau]z^{-\tau}. \quad (2.21)$$

By substituting $k = -\tau$, this becomes

$$\mathbf{R}(z) = \sum_{k=-\infty}^{\infty} \mathbf{R}^H[k]z^k \quad (2.22)$$

Recognizing that $z^k = (1/z^*)^{-k}$ and taking the Hermitian transpose, we obtain

$$\mathbf{R}(z) = \{\mathbf{R}(1/z^*)\}^H \quad (2.23)$$

Therefore, the CSD matrix satisfies the parahermitian symmetry property

$$\mathbf{R}^P(z) = \{\mathbf{R}(1/z^*)\}^H = \mathbf{R}(z), \quad (2.24)$$

where $\{\cdot\}^P$ is the parahermitian transpose operator, which applies a Hermitian transposition and time reversal. A matrix that satisfies the property (2.24) is termed a parahermitian matrix. CSD matrices, therefore, are parahermitian matrices by construction; this impacts the EVD, which we will explore further.

In order to compare the CSD matrices between the input and the output of a system as in Fig. 2.2, we define the space-time covariances $\mathbf{R}_x[\tau] = \mathcal{E}\{\mathbf{x}[n]\mathbf{x}^H[n-\tau]\}$ and $\mathbf{R}_y[\tau] = \mathcal{E}\{\mathbf{y}[n]\mathbf{y}^H[n-\tau]\}$, and their associated CSD matrices $\mathbf{R}_x(z) \bullet\!\!\!\circ \mathbf{R}_x[\tau]$ and $\mathbf{R}_y(z) \bullet\!\!\!\circ \mathbf{R}_y[\tau]$. Using the time domain relation (2.12),

$$\mathbf{R}_y[\tau] = \mathcal{E}\left\{\sum_{\nu} \mathbf{C}[\nu]\mathbf{x}[n-\nu] \left(\sum_{\mu} \mathbf{C}[\mu]\mathbf{x}[n-\tau-\mu]\right)^H\right\} \quad (2.25)$$

$$= \sum_{\nu,\mu} \mathbf{C}[\nu] \mathcal{E}\{\mathbf{x}[n-\nu]\mathbf{x}[n-\tau-\mu]^H\} \mathbf{C}^H[\mu] \quad (2.26)$$

$$= \sum_{\nu,\mu} \mathbf{C}[\nu] \mathbf{R}_x[\tau+\mu-\nu] \mathbf{C}^H[\mu] \quad (2.27)$$

$$= \mathbf{C}[\tau] * \mathbf{R}_x[\tau] * \mathbf{C}^H[-\tau]. \quad (2.28)$$

For CSD matrices, the result in (2.28) is equivalent to

$$\mathbf{R}_y(z) = \mathbf{C}(z)\mathbf{R}_x(z)\mathbf{C}^P(z). \quad (2.29)$$

If Fig. 2.2 is an innovation model [112] with temporally and spatially uncorrelated input signals that are zero mean and unit variance s.t. $\mathbf{R}_x(z) = \mathbf{I}_L$ with \mathbf{I}_L an $L \times L$ identity matrix, then $\mathbf{R}_y(z) = \mathbf{C}(z)\mathbf{C}^P(z)$, and the system $\mathbf{C}(z)$ explains the spatio-temporal correlations of $\mathbf{y}[n]$. In that case, note that if $\mathbf{C}(z)$ is a polynomial, $\mathbf{C}(z)\mathbf{C}^P(z)$ will be Laurent polynomial (i.e. of finite order); if $\mathbf{C}(z)$ is a power series, the $\mathbf{C}(z)\mathbf{C}^P(z)$ will be Laurent series (i.e. potentially of infinite order). As opposed to polynomials and power series, Laurent polynomials and Laurent series, respectively, are finite and infinite order expressions in both z and z^{-1} .

Example 2 *If the channel matrix $\mathbf{C}[n]$ from Example 1 is excited by an input $\mathbf{x}[n]$*

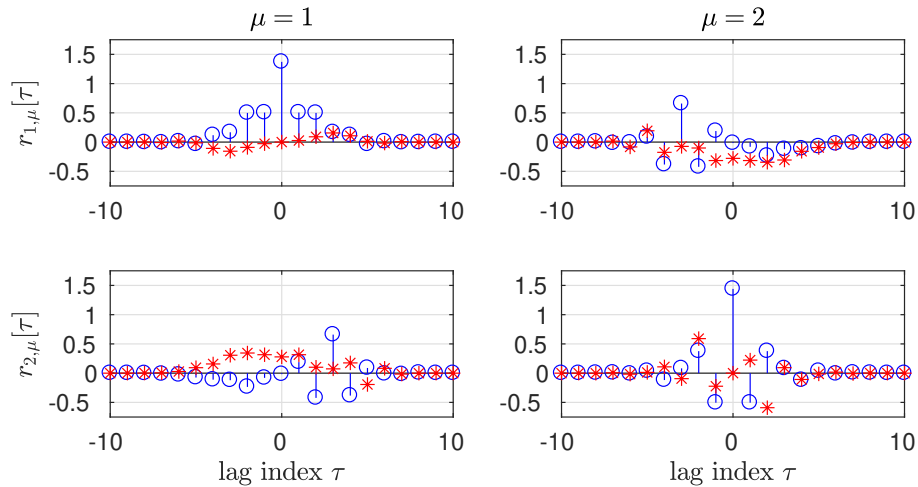


Figure 2.4: Space-time covariance matrix for Example 2 comprising of cross-correlation sequences $r_{m,\mu}[\tau]$, $m, \mu = 1, 2$, with (\circ) and $(*)$ symbolising real and imaginary parts, respectively.

that is spatially and temporally uncorrelated with zero mean and unit variance, then the space-time covariance matrix of the output $\mathbf{y}[n] = \mathbf{C}[n] * \mathbf{x}[n]$ is $\mathbf{R}_y[\tau] = \mathbf{C}[\tau] * \mathbf{C}^H[-\tau]$ as shown in Fig. 2.4. Note the conjugate symmetry of the diagonal elements with $r_{1,2}[\tau] = r_{2,1}^*[-\tau]$.

2.3.3 Broadband versus Narrowband Consideration

Secs. 2.3.1 and 2.3.2 covered broadband generalisation of narrowband concepts — channel matrices containing impulse responses rather than complex gain factors, and space-time instead of instantaneous covariance matrices. We will now briefly review under which circumstances it is important to ensure that such broadband aspects are captured, i.e., when it is insufficient to rely on narrowband description only.

For channel characterisation, such as in Sec. 2.3.1, a narrowband system applies a complex gain that can impose a frequency-independent amplitude and phase change on a signal. This is suitable if, e.g., the delay spread of the channel is small relative to the symbol time or sampling period of the transmitted signal. Another rule of thumb is that channels should be characterised as broadband if the fractional bandwidth — the ratio between bandwidth and carrier frequency — exceeds a certain percentage.

This fractional bandwidth limit is typically stated between 5 and 10%, but in array configurations also depends on the array aperture [113]: the wider the aperture, the lower the fractional bandwidth limit for a scenario to be considered broadband.

Since we address CR systems with multiple antennas, the spatial information of signals is important. Given a signal arriving at different receive antennas, the direction of propagation resides in the relative delays with which the signal arrives at the different antenna array elements. In the narrowband case, these delays reduce to phase shifts, and the spatial correlation between different antenna signals is entirely captured by the complex-valued elements of the instantaneous covariance matrix expressed in terms of these phase shifts. In the broadband case, we must consider explicit time delays, and hence a lag value must be included in the space-time covariance matrix $\mathbf{R}[\tau]$. The boundary between the two cases is somewhat fluent, but a number of indicators can be found in the literature. For example, if the signals received by different elements of the array are not fully correlated — which happens when the array is large compared to the signal wavelength or when the signal has a wide bandwidth — the system should be treated as broadband [114]. There are other indicators, for example, if the rank of the instantaneous covariance matrix exceeds the number of independent sources in the environment [115], or if performance metrics such as for angle-of-arrival (AOA) estimation start to drop [116–119].

By selecting the correct description via narrowband or broadband considerations, e.g. optimisation problems based on channels or signal power can be adequately formulated. The solution to such problems then often requires factorising, e.g., channel matrices or covariances in the narrowband case. To extend this utility of the broadband case, Secs. 2.4 and 2.5 review factorisation techniques for polynomial matrices that will be exploited in later chapters of this thesis.

2.4 Eigenvalue Decomposition of a Parahermitian Matrix

2.4.1 Parahermitian Matrix EVD

The standard EVD [120] applies to ordinary matrices with real- or complex-valued entries. If evaluated for a space-time covariance matrix $\mathbf{R}[\tau]$ or a CSD matrix $\mathbf{R}(z)$, the EVD can generally only diagonalise such a system for one specific parameter τ or z . To extend the diagonalisation across all parameter values for τ or z , we require to extend the EVD to a polynomial matrices [107]. Specifically, for a parahermitian, analytic matrix $\mathbf{R}(z)$, there exists in almost all cases a parahermitian matrix EVD [109,110,121]

$$\mathbf{R}(z) = \mathbf{Q}(z)\mathbf{\Lambda}(z)\mathbf{Q}^P(z) \quad (2.30)$$

such that $\mathbf{\Lambda}(z)$ is a diagonal, parahermitian matrix of eigenvalues, and the paraunitary matrix $\mathbf{Q}(z) = [\mathbf{q}_1(z), \dots, \mathbf{q}_M(z)]$ contains in its columns the corresponding eigenvectors. Both factors can be selected to be analytic, paraunitarity implies that [108,122]

$$\mathbf{Q}(z)\mathbf{Q}^P(z) = \mathbf{Q}^P(z)\mathbf{Q}(z) = \mathbf{I}_M. \quad (2.31)$$

For $\mathbf{\Lambda}(z) = \text{diag}\{\lambda_1(z), \dots, \lambda_M(z)\}$, the parahermitian property $\lambda_m^P(z) = \lambda_m(z)$, $m = 1, \dots, M$ implies that when evaluated on the unit circle, $\lambda(e^{j\Omega}) \in \mathbb{R}$. These properties are generalizations of the EVD of a Hermitian matrix.

The analytic eigenvalues $\lambda_m(z)$ in (2.30) are distinct up to their ordering within $\mathbf{\Lambda}(z)$. If there are no identical eigenvalues, i.e., if $\lambda_m(z) = \lambda_\mu(z)$ only holds for $m = \mu$, then their corresponding eigenvectors are unique up to an arbitrary allpass function $\phi_m(z)$: if $\mathbf{q}_m(z)$ is a valid m th eigenvector of $\mathbf{R}(z)$, then so is $\phi_m(z)\mathbf{q}_m(z)$.

Example 3 For the CSD matrix of Example 2, the factorisation $\mathbf{R}(z) = \mathbf{Q}(z)\mathbf{\Lambda}(z)\mathbf{Q}^P(z)$ is shown in Fig. 2.5. Note that in this case $\mathbf{Q}(z)$ is a polynomial of order 4, while the parahermitian and diagonal $\mathbf{\Lambda}(z)$ is a Laurent polynomial of order 8. An arbitrary allpass can modify the eigenvalues. If this allpass is anything other than a delay, then $\mathbf{Q}(z)$ is generally a power series of infinite order. In addition, the evaluation of the

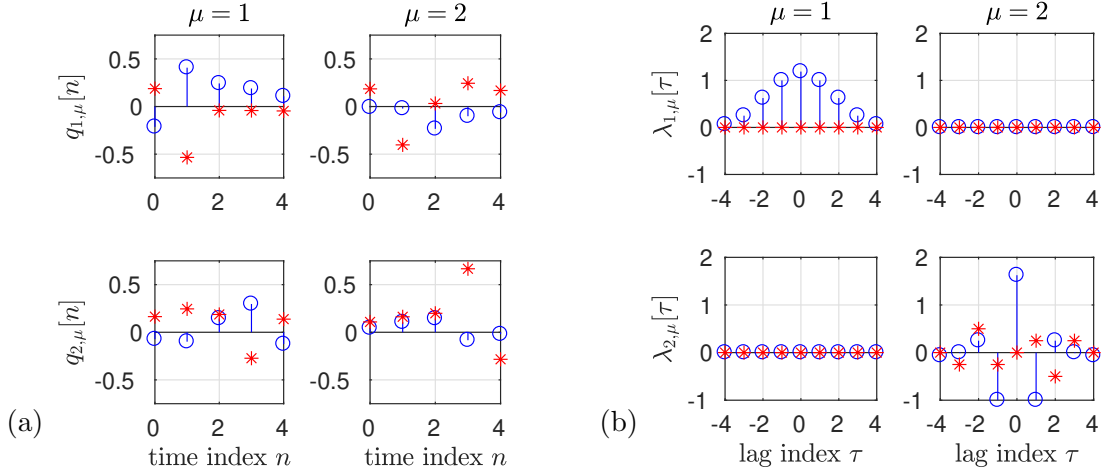


Figure 2.5: Parahermitian matrix EVD factors (a) $\mathbf{Q}[n] \circ \bullet \mathbf{Q}(z)$ and (b) $\Lambda[\tau] \bullet \circ \Lambda(z)$ for Example 3, with (\circ) and $(*)$ symbolising real and imaginary parts, respectively.

eigenvalues in the unit circle, $\lambda_m(e^{j\Omega})$, $m = 1, 2$, is illustrated in Fig. 2.6.

2.4.2 Application to Strong Decorrelation and Subspace Decomposition

Assume that a measurement vector $\mathbf{x}[n]$ has a CSD matrix $\mathbf{R}_x(z)$ with the parahermitian matrix EVD $\mathbf{R}_x(z) = \mathbf{Q}(z)\Lambda(z)\mathbf{Q}^P(z)$. We now use the parahermitian of the eigenvector matrix, $\mathbf{Q}^P(z)$, to process the data as shown in Fig. 2.7(a). Because $\mathbf{Q}(z)$ is paraunitary, the transformation $\mathbf{y}[n] = \mathbf{Q}^H[-n] * \mathbf{x}[n]$ with $\mathbf{Q}[n] \circ \bullet \mathbf{Q}(z)$ reserves the total signal power $\mathcal{E}\{\|\mathbf{y}[n]\|_2^2\} = \mathcal{E}\{\|\mathbf{x}[n]\|_2^2\}$. This is analogous to a unitary rotation in frequency space: it changes the basis to one in which the signals are decorrelated but does not amplify or attenuate energy. For the CSD of $\mathbf{y}[n]$ we find based on (2.29) that $\mathbf{R}_y(z) = \mathbf{Q}^P(z)\mathbf{R}_x(z)\mathbf{Q}(z) = \Lambda(z)$. The diagonal CSD matrix indicates that all elements of $\mathbf{y}[n]$ in Fig. 2.7(a) are decorrelated, but do not amplify or attenuate energy. The diagonal matrix $\Lambda(z)$ resulting from this transformation contains the individual power spectra of the decorrelated components, providing both a measure of their energy distribution for all possible lag values τ , and this property of $\mathbf{y}[n]$ is referred to as a strong decorrelation [108, 123]. This is a useful property for applications such as subband coding [124] or source enumeration [125].

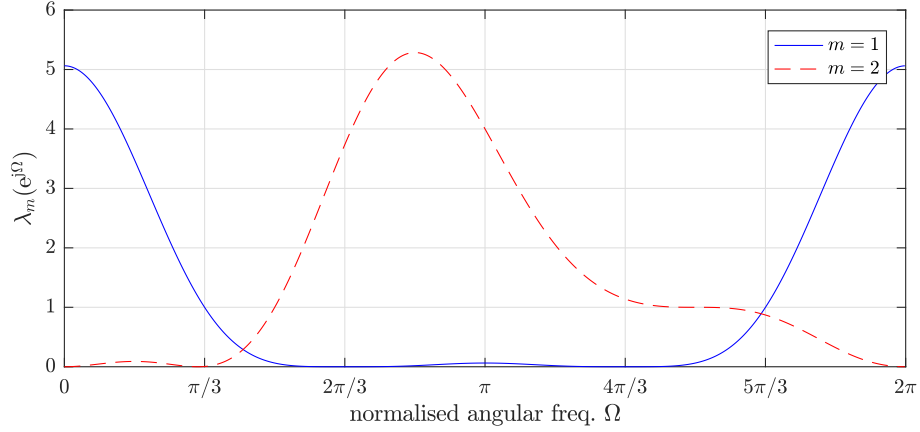
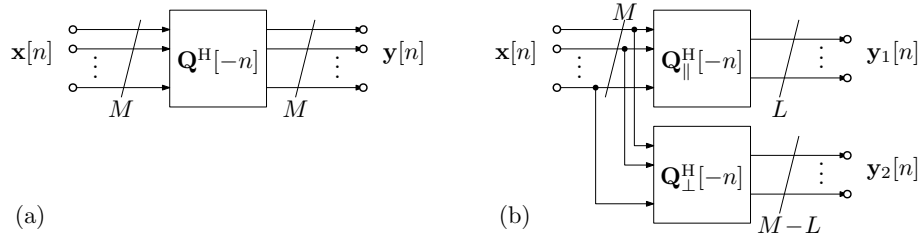

 Figure 2.6: Eigenvalues $\lambda_m(e^{j\Omega})$, $m = 1, 2$, of Example 3.


Figure 2.7: Applying parahermitian matrix factors for (a) strong decorrelation and (b) subspace decomposition.

The parahermitian matrix EVD can also be used for defining subspaces. To explore this, assume the situation of Fig. 2.2 with an input CSD matrix $\mathbf{R}_{\mathbf{x}}(z) = \mathbf{I}_L$ of dimension $L \times L$ with $L < M$, and an output $\mathbf{y}'[n] = \mathbf{y}[n] + \mathbf{v}[n]$ where $\mathbf{v}[n]$ is spatially and temporally uncorrelated zero mean noise of variance σ_v^2 that is independent of $\mathbf{y}[n]$. Then we have $\mathbf{R}_{\mathbf{v}}(z) = \sigma_v^2 \mathbf{I}_M$, and we obtain

$$\mathbf{R}_{\mathbf{y}'}(z) = \mathbf{R}_{\mathbf{y}}(z) + \sigma_v^2 \mathbf{I}_M \quad (2.32)$$

for the CSD matrix of the noise output of $\mathbf{y}'[n]$. Because $\mathbf{R}_{\mathbf{y}}(z)$ is generated by the source model of Fig. 2.2, it will be rank L . The parahermitian EVD of the rank- L matrix $\mathbf{R}_{\mathbf{y}}(z)$ is given by $\mathbf{R}_{\mathbf{y}}(z) = \mathbf{Q}^P(z) \mathbf{\Lambda}(z) \mathbf{Q}(z)$, whereby $\mathbf{\Lambda}(z) = \text{diag} \{ \lambda_1(z), \dots, \lambda_L(z), 0, \dots, 0 \}$.

Due to $\mathbf{Q}(z)\mathbf{Q}^P(z) = \mathbf{I}_M$, we can write

$$\mathbf{R}_{\mathbf{y}'}(z) = \mathbf{Q}^P(z)\mathbf{\Lambda}(z)\mathbf{Q}(z) + \sigma_v^2\mathbf{I}_M = \mathbf{Q}(z) (\mathbf{\Lambda}(z) + \sigma_v^2\mathbf{I}_M) \mathbf{Q}^P(z) \quad (2.33)$$

$$= \begin{bmatrix} \mathbf{Q}_{\parallel}(z) & \mathbf{Q}_{\perp}(z) \end{bmatrix} \begin{bmatrix} \mathbf{\Lambda}'(z) + \sigma_v^2\mathbf{I}_L & \\ & \sigma_v^2\mathbf{I}_{M-L} \end{bmatrix} \begin{bmatrix} \mathbf{Q}_{\parallel}^P(z) \\ \mathbf{Q}_{\perp}^P(z) \end{bmatrix}, \quad (2.34)$$

where $\mathbf{\Lambda}'(z) = \text{diag}\{\lambda_1(z), \dots, \lambda_L\}$ is an $L \times L$ matrix. The L eigenvectors corresponding to $\mathbf{\Lambda}'$ are gathered in the $M \times L$ matrix $\mathbf{Q}_{\parallel}(z)$, while the remaining $(M - L)$ eigenvectors reside in the $M \times (M - L)$ matrix $\mathbf{Q}_{\perp}(z)$. Because $\begin{bmatrix} \mathbf{Q}_{\parallel}(z) & \mathbf{Q}_{\perp}(z) \end{bmatrix}$ is paraunitary, we have $\mathbf{Q}_{\parallel}^P(z)\mathbf{Q}_{\perp}(z) = \mathbf{0}$. Akin to the case of ordinary matrices [120], (2.34) offers subspace partitioning, where the columns of $\mathbf{Q}_{\parallel}(z)$ span the signal-plus-noise subspace and the columns of $\mathbf{Q}_{\perp}(z)$ the noise-only subspace.

This subspace partitioning can be exploited as in Fig. 2.7(b) the matrix $\mathbf{Q}_{\perp}^P(z)$ generates an output $\mathbf{y}_2[n]$ that contains only noise, while all structured signal components are contained in the output $\mathbf{y}_1[n]$ generated by $\mathbf{Q}_{\parallel}^P(z)$. This can be used for applications such as denoising for speech enhancement [105, 126], broadband angle of arrival estimation [127–129], localisation and path discovery [130, 131], dimensionality reduction and compaction [132], or energy detection [5, 133, 134]. This is driven by the statistics of a multichannel signal, and the fact that these signals only occupy a limited subspace; sparsity in some domain can also be driven by other criteria, such as the ℓ_0 -norm in compressive sensing, see e.g. [135, 136].

2.4.3 Parahermitian Matrix EVD Algorithms

A number of algorithms to approximate the parahermitian matrix EVD in (2.30) have been proposed. Initial attempts preceded the existence proof for (2.30), and included time domain algorithms such as second-order sequential best rotation (SBR2) algorithms and its variants [106, 107, 124, 137] as well as sequential matrix diagonalisation (SMD) algorithms [138–140]. These techniques iteratively eliminated off-diagonal elements of $\mathbf{R}(z)$ by means of elementary paraunitary operations until a sufficient level

of diagonalisation is achieved. These algorithms encourage spectral majorisation, such that the extracted eigenvalues are generally ordered at every frequency such that

$$\hat{\lambda}_1(e^{j\Omega}) \geq \hat{\lambda}_2(e^{j\Omega}) \geq \dots \geq \hat{\lambda}_M(e^{j\Omega}) \quad \forall \Omega. \quad (2.35)$$

In the case of the SBR2 algorithm, spectral majorisation is a proven property of the algorithm [141]. Both SBR2 and SMD algorithms have worked sufficiently well for many applications, but spectral majorization in (2.35) limits in how closely they can approximate (2.30): even though it has been suggested that approximation can be arbitrarily close for sufficiently high polynomial order of the decomposition factors [142], if the ground-truth analytic eigenvalues intersect, SBR2 and SMD are trying to approximate piece-wise analytic functions, resulting in non-differentiable eigenvalues and discontinuous eigenvectors [109]. Because of the above spectral majorisation, the eigenvalues approximated by SBR2 and SMD algorithms are switched where the ground truth analytic eigenvalues intersect, leading to non-differentiability. For their corresponding eigenvectors, SBR2 and SMD therefore recover also switched functions, which, because of the orthogonality of the eigenvectors, leads to the approximation of discontinuous functions compared to the ground truth analytic eigenvectors. This is, for example, evidenced in AOA estimation applications [143].

In order to directly target the analytic factorisation in (2.30), a number of frequency-domain methods have emerged. This includes a smooth DFT-domain decomposition in [144] for a given DFT-size, and iterative DFT-domain algorithms that grow the DFT-length until sufficient accurate eigenvalues [145–148] and eigenvectors [149–151], with proven convergence for [146, 151].

Example 4 *To demonstrate two algorithms, applying SMD [138] to the CSD matrix $\mathbf{R}(z)$ of Example 2 with a maximum of 200 iterations results in the matrices $\hat{\mathbf{Q}}(z)$ and $\hat{\mathbf{\Lambda}}(z)$ in Fig. 2.8, which shows truncated polynomials. Evaluating the eigenvalues on the unit circle results in the curves in Fig. 2.9, which compared to the ground truth in Fig. 2.6 are now spectrally majorised and no longer intersect. Reconstructing*

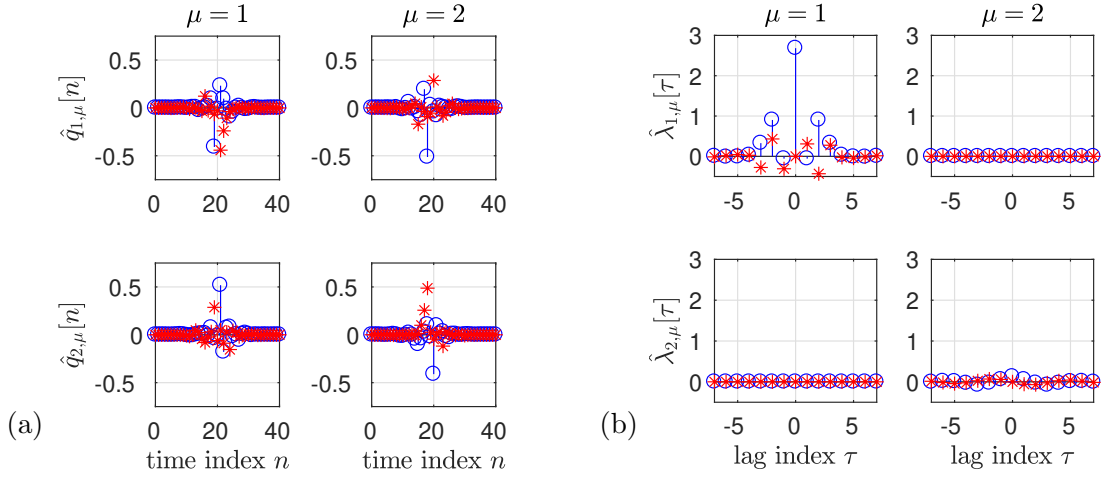


Figure 2.8: Results of the SMD algorithm in Example 4 approximating the EVD factors (a) $\hat{\mathbf{Q}}[n]$ \circ — \bullet $\mathbf{Q}(z)$ and (b) $\hat{\mathbf{\Lambda}}[\tau]$ \circ — \bullet $\mathbf{\Lambda}(z)$ of $\mathbf{R}(z)$ from Example 2, with (\circ) and $(*)$ symbolising real and imaginary parts, respectively.

$\hat{\mathbf{R}}(z) = \hat{\mathbf{Q}}(z)\hat{\mathbf{\Lambda}}(z)\hat{\mathbf{Q}}^P(z)$ with the shown precision with $\hat{\mathbf{R}}[\tau]$ \circ — \bullet $\mathbf{R}(z)$ yields an error $\sum_{\tau} \|\mathbf{R}[\tau] - \hat{\mathbf{R}}[\tau]\|_{\text{F}}^2 = 8.334$, where $\|\cdot\|_{\text{F}}$ is the Frobenius norm. In contrast, running the analytic eigenvalues and eigenvector extractions from [146, 151] results in an error of $6.571 \cdot 10^{-10}$, which matches the selected precision of 10^{-10} in the extraction algorithms [146, 151].

The SMD algorithm is iterative with typically linear convergence. Its convergence rate depends on eigenvalue separation, matrix size, and polynomial truncation. For Example 2, 200 iterations yield a Frobenius norm error of 8.334, significantly higher than the precision 10^{-10} achieved by the analytic extraction methods of eigenvalue and eigenvectors [146, 151]. This highlights that SMD provides only an approximate para-hermitian EVD and may converge slowly, particularly for near-degenerate eigenvalues or truncated representations. Although SMD is computationally cheaper per iteration, it often requires many iterations to achieve acceptable accuracy. In contrast, analytic methods incur a higher per-pass cost but deliver high-precision results in a single step, making them preferable for accuracy-critical applications.

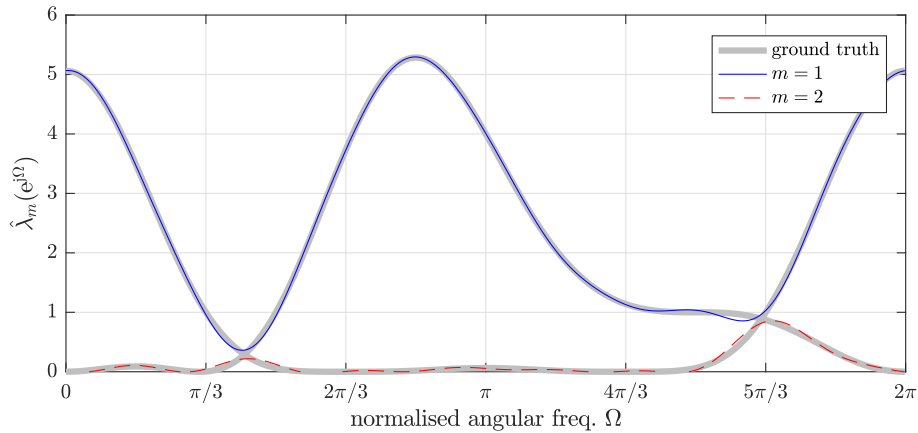


Figure 2.9: Approximate eigenvalues $\hat{\lambda}_m(e^{j\Omega})$, $m = 1, 2$, obtained with the SMD algorithm, with the ground truth analytic eigenvalues of Example 3 underlaid in grey.

2.5 Polynomial Matrix Singular Value Decomposition

The parahermitian matrix EVD or analytic EVD in Sec. 2.4 applies to parahermitian matrices only. In order to diagonalise general polynomial matrices, such as the MIMO channel matrix in (2.10), in the following we review an extension of the SVD, which plays a central role in signal processing [152–154] and is, for example, widely used for the factorization of MIMO communication channels [155], to the broadband case.

2.5.1 Analytic SVD

Assume an analytic matrix $C(z) : \mathbb{C} \rightarrow \mathbb{C}^{M \times N}$ which for $M \neq N$ includes the non-square case. Analyticity implies that the entries of $C[n] \circ \bullet C(z)$ are causal and stable filters, such that the elements $c_{m,n}[n]$ decay at least exponentially. If $C(z)$ is not tied to multiplexing, it generally admits an analytic SVD [121, 156]

$$C(z) = U(z)\Sigma(z)V^P(z), \quad (2.36)$$

where $\Sigma(z)$ is an analytic diagonal, parahermitian matrix containing analytic singular values, and $U(z) : \mathbb{C} \rightarrow \mathbb{C}^{M \times M}$ and $V(z) : \mathbb{C} \rightarrow \mathbb{C}^{N \times N}$ are paraunitary matrices that hold the corresponding analytic left- and right-singular vectors [121, 156]. Recall

that paraunitarity implies that e.g., $\{\mathbf{U}(z)\}^{-1} = \mathbf{U}^{\text{P}}(z) = \{\mathbf{U}(1/z^*)\}^{\text{H}}$ with $\{\cdot\}^{\text{P}}$ the parahermitian transposition as defined in (2.24), while a matrix being parahermitian means that $\mathbf{\Sigma}^{\text{P}}(z) = \mathbf{\Sigma}(z)$, which implies that on the unit circle, $\mathbf{\Sigma}(e^{j\Omega})$ is real-valued.

The singular values $\sigma_m(z)$ within $\mathbf{\Sigma}(z) = \text{diag}\{\sigma_1(z), \dots, \sigma_M(z)\}$ are unique up to their ordering. Unlike the ordinary SVD of the matrix [120], where singular values are sorted in descending order, analytic singular values can intersect, making the majorisation less meaningful. To ensure $\sigma_m(z)$ is analytic [156], similar to the continuous time case [157, 158], singular values must be allowed to become negative.

Similar to the analytic eigenvectors, the left- and right-singular vectors can be modified by arbitrary allpass functions, but are coupled. With $\mathbf{U}(z) = [\mathbf{u}_1(z), \dots, \mathbf{u}_M(z)]$ and $\mathbf{V}(z) = [\mathbf{v}_1(z), \dots, \mathbf{v}_N(z)]$, we can write (2.36) alternatively as

$$\mathbf{C} = \sum_{\ell=1}^{\min(M,N)} \sigma_{\ell}(z) \mathbf{u}_{\ell}(z) \mathbf{v}_{\ell}^{\text{P}}(z) = \sum_{\ell=1}^{\min(M,N)} \sigma_{\ell}(z) (\mathbf{u}_{\ell}(z) \phi_{\ell}(z)) (\phi_{\ell}^{\text{P}}(z) \mathbf{v}_{\ell}^{\text{P}}(z)) \quad (2.37)$$

where $\phi_{\ell}(z)$ is an allpass, noting that $\phi_{\ell}(z) \phi_{\ell}^{\text{P}}(z) = 1$. Thus, if $\mathbf{u}_{\ell}(z)$ and $\mathbf{v}_{\ell}(z)$ are a pair of valid left- and right-singular vectors, then so are $\phi_{\ell}(z) \mathbf{u}_{\ell}(z)$ and $\phi_{\ell}(z) \mathbf{v}_{\ell}(z)$.

In some contrived cases, the analytic SVD in (2.36) may not exist because the singular values exhibit an odd number of zero crossings, leading to 4π -periodicity on the unit circle. This can be resolved by either seeking the decomposition of $\mathbf{C}(z^2)$, i.e. the twice oversampled matrix [156], or by including a half-sample delay in the offending singular values — which then are no longer parahermitian [159, 160].

2.5.2 Relation to Analytic EVD

Recall from the innovation model in Fig. 2.2 and (2.29) that for a temporally and spatially uncorrelated input, the output of a system $\mathbf{C}(z)$ possesses the CSD matrix $\mathbf{R}(z) = \mathbf{C}(z) \mathbf{C}^{\text{H}}(z)$. If $\mathbf{C}(z)$ can be factored as shown in (2.36), then

$$\mathbf{R}(z) = \mathbf{C}(z) \mathbf{C}^{\text{P}}(z) = \mathbf{U}(z) \mathbf{\Sigma}(z) \mathbf{V}^{\text{P}}(z) \mathbf{V}(z) \mathbf{\Sigma}^{\text{P}}(z) \mathbf{U}^{\text{P}}(z) \quad (2.38)$$

$$= \mathbf{U}(z) \mathbf{\Sigma}(z) \mathbf{\Sigma}^{\text{P}}(z) \mathbf{U}^{\text{P}}(z) \quad (2.39)$$

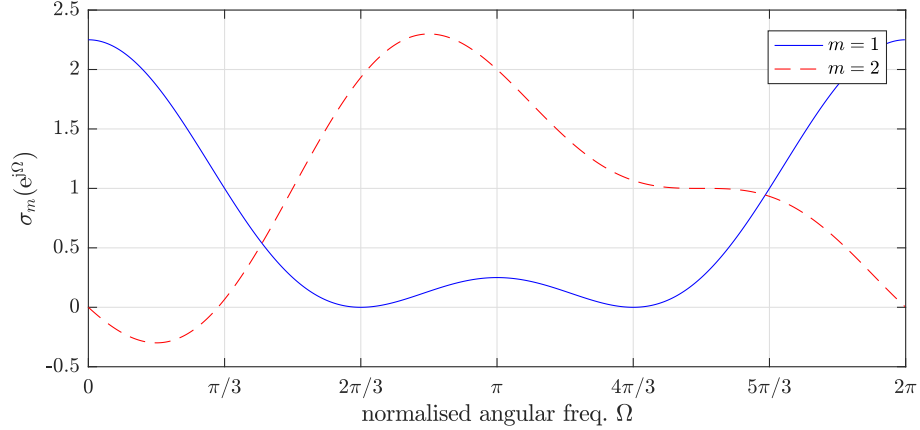


Figure 2.10: Singular values $\sigma_m(e^{j\Omega})$, $m = 1, 2$, of Example 5.

Thus, w.r.t. the parahermitian matrix EVD in (2.16), we find that $\mathbf{Q}(z) = \mathbf{U}(z)$ and $\mathbf{\Lambda}(z) = \mathbf{\Sigma}(z)\mathbf{\Sigma}^P(z)$. If we were to set $\mathbf{R}(z) = \mathbf{C}^P(z)\mathbf{C}(z)$, then its parahermitian matrix EVD will yield the same eigenvalues as before, but we have $\mathbf{Q}(z) = \mathbf{V}(z)$.

Example 5 *The singular values of the channel matrix $\mathbf{C}(z)$ of Example 1, evaluated on the unit circle, is shown in Fig. 2.10. Note that $\sigma_2(e^{j\Omega})$ takes on negative values between $\Omega = 0$ and approximately $\Omega = \frac{\pi}{3}$.*

For the eigenvalues of Example 3 in Fig. 2.6, $\lambda_m(e^{j\Omega}) = |\sigma_m(e^{j\Omega})|^2$, and the eigenvectors in Fig. 2.5(a) match the left-singular vectors in $\mathbf{U}(z)$ due to (2.39).

2.5.3 Polynomial Matrix SVD Algorithms and Applications

Initial approximate SVD algorithms for applications in e.g., communications [161–165] exploited the EVD relationship as outlined in Sec. 2.5.2. This approach solved two parahermitian matrix EVDs of $\mathbf{C}(z)\mathbf{C}^P(z)$ and $\mathbf{C}^P(z)\mathbf{C}(z)$ to obtain $\hat{\mathbf{U}}(z)$ and $\hat{\mathbf{V}}(z)$, respectively, and then obtained the singular values via $\hat{\mathbf{\Sigma}}(z) = \mathbf{U}^P(z)\mathbf{C}(z)\mathbf{V}(z)$ as suggested in [107]. Dedicated time-domain algorithms have emerged for the SVD, including an extension of the Kogbetliantz method to the broadband case [166], as well as an extension of an SMD-like scheme in [167]. However, similar to SBR2 and SMD algorithms, such methods favour spectrally majorised singular values, and hence may

not recover the ground truth where analytic singular values $\sigma_m(e^{j\Omega})$, $m = 1, \dots, M$, intersect as in the example of Fig. 2.10.

More recently, some initial attempts at frequency domain methods aligned with the DFT-domain parahermitian matrix EVD algorithms in [146, 151] have also emerged in [168–172], but require some further efforts to robustly yield the analytic SVD decomposition in (2.36). Meanwhile, it is possible to use the parahermitian matrix EVD algorithms in [146, 151] to approximate the analytic SVD factors via the connection in Sec. 2.5.2.

2.6 Chapter Summary

This chapter has provided some background on the area of research addressed in this thesis. This firstly concerned energy detection techniques for CRNs, where the use of MIMO-based GLRT techniques appears to be particularly appealing. To address MIMO techniques, and particularly broadband MIMO scenarios, this chapter has further introduced some fundamentals of polynomial matrix representations, which is a convenient way to express second-order statistics and terms such as signal power or energy. This can lead to straightforward formulations for broadband MIMO problems; solutions can often be obtained by way of polynomial matrix algebra, where generalisations of the EVD and SVD to polynomial matrices have been reviewed.

In the remainder of this thesis, we will use these mathematical techniques in Chapter 3 to explore a subspace detector for transient signals such as from emerging PUs, which we then benchmark against the optimal detection based on the LRT and GLRT. This then sets the basis for targeted interference in Chapter 4 and for fluctuating noise PSD across arrays, which also utilise the polynomial matrix techniques reviewed in this this background chapter.

Chapter 3

Detection of Weak Transient Broadband Signals

3.1 Introduction

Detecting the emergence of weak broadband transient signals presents a significant challenge for various applications. In CR environments [21, 173–175], for example, it is vital to identify emerging primary users. Recognizing faint speakers among background noise [133] or multiple voices [134] is a key task in the audio domain. Similarly, detecting weak transient sources in the RF or sonar domains is essential in military contexts [5].

Energy-based methods, including the short-time Fourier transform (STFT) and wavelet-based approaches, are frequently used to detect transient signals by analyzing their correlation structures [176–178]. For multisensory data, data-dependent transforms such as the Karhunen-Loeve transform [179] efficiently achieve optimal energy compaction in lower-dimensional subspaces through the EVD of the covariance matrix. In addition, subspace partitioning techniques have been utilized in various source detection applications [180–184].

An interesting method is the proposed polynomial subspace projection approach for broadband signals [5]. This method resembles the filter bank-based joint source-channel coder discussed in [185], where the projection away from the code subspace as

defined by the code’s generator matrix is termed a ‘syndrome vector’. This syndrome helps to identify and correct transmission errors [185]. In broadband signal detection, an increase in energy within the noise-only polynomial subspace indicates the presence of a new transient signal. This methodology detects weak transient signals by projecting received data onto the orthogonal complement of the subspace spanned by the stationary sources. This eliminates the need for channel state information w.r.t. the transient source, which is often unreliable in practice, and instead focusses on energy within the noise-only subspace to identify emerging signals.

In this chapter, first the approach in [5] is explored by providing polynomial matrix representations for subspace detection in the context of this thesis. This approach extends existing subspace detection approaches such as [180–184], which use standard linear algebraic tools [120], to the domain of polynomial matrices, capable of addressing broadband problems as outlined in Chapter 2. Specifically, we here demonstrate the structure of the space-time covariance and the resulting subspace decomposition. The norm of the projection onto the noise-only subspace of the space-time covariance matrix, termed the syndrome vector, follows a generalized χ^2 distribution; as a criterion, its discrimination w.r.t. to data with transients either absent or present can be enhanced by averaging. A threshold-independent framework indicates that weak sources can be identified reliably, provided that sufficient temporal support is available to estimate the covariance matrix. Based on the existing algorithmic approach in [5], the contribution of this chapter lies in understanding and characterising the performance of this broadband subspace method with respect to suitable benchmarks.

In order to explore the performance of this broadband subspace-based energy test, it is here benchmarked against an LRT/GLRT optimal detector [186, 187]. Such detectors rely on the statistics or channels to be known or estimated. While this is impractical for an emerging, transient broadband source, assuming such knowledge nevertheless lets us deploy LRT or GLRT approaches in order to provide a comparison for the syndrome energy approach. We apply the LRT/GLRT approaches to both directly the sensor data, but also explore its application to the syndrome vector, which can reveal

some of the appeals of the syndrome approach: optimal test such as LTR/GLRT, when evaluated, can suffer from numerical problems such as large matrix dimensions and ill-conditioning for high-dimensional data, high temporal correlation, and at low SNR [44, 46], and can be computationally very demanding. This comparison can thus highlight how the syndrome-based method approximates optimal detection performance without channel information while ensuring numerical stability and scalability. This trade-off benefits practical applications, making the syndrome vector a more feasible option for real-world broadband detection systems.

In the remainder of this chapter, the system model and broadband subspace decomposition are detailed in Secs. 3.2 and 3.3, which leads to a broadband subspace detector in Sec. 3.4 and in turn to an examination of the subspace energy. Temporal correlation complicates the description of subspace energy, but a decimated processor facilitates the use of statistical results for generalized χ^2 distributions to define discrimination metrics. Sec. 3.5 reviews the LRT method, with the key contribution in Sec. 3.6 focusing on the LRT applied to measurement and projected data. Sec. 3.7.1 analyzes the sample cross-correlation sequence as a linear unbiased estimator using Gaussian data, characterizing its variance and estimating error against ground truth, with simulations in Sec. 3.8. A summary for Chapter 3 is provided in Sec. 3.9.

3.2 Data Model and Space-Time Covariance Matrix

3.2.1 Data model

We consider a scenario with M sensors measuring emission from $L < M$ stationary sources in the environment, as shown in Fig. 3.1. The sources are modelled as mutually independent, temporally uncorrelated signals with zero mean and unit variance, represented by $u_\ell[n], \ell = 1, \dots, L$ organized in a vector $\mathbf{u}[n] = [u_1[n], \dots, u_L[n]]^T \sim \mathcal{CN}(\mathbf{0}, \mathbf{I}_L)$. The power spectral density of the individual sources, affected by the convolutive mixing, is represented by a matrix of impulse responses $\mathbf{H}[n] \in \mathbb{C}^{M \times L}$, which also functions as an innovation filter [112]. Measurements are corrupted by additive

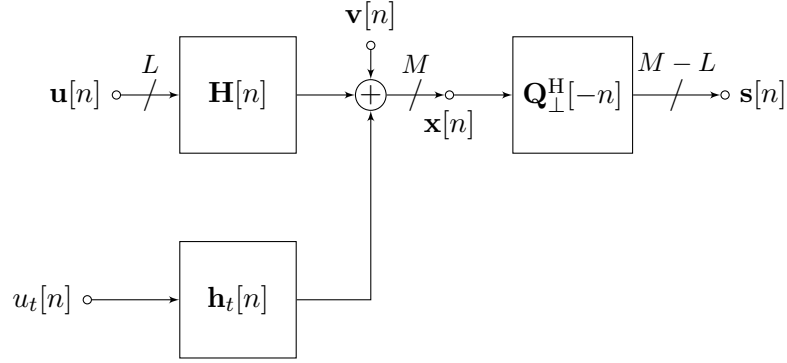


Figure 3.1: Signal model for measurement $\mathbf{x}[n] \in \mathbb{C}^M$, containing stationary sources $\mathbf{u}[n] \in \mathbb{C}^L$, and a transient source $\mathbf{u}_t[n]$ and processing by $\mathbf{Q}_\perp^H[-n]$ to yield a subspace projection $\mathbf{s}[n] \in \mathbb{C}^{M-L}$.

Gaussian noise $v[n] \in \mathbb{C}^M$ with covariance $\mathcal{E}\{\mathbf{v}[n]\mathbf{v}^H[n-\tau]\} = \sigma_v^2\delta[\tau]\mathbf{I}$, where $\mathcal{E}\{\cdot\}$ is the mathematical expectation operator performed on n , where wide-sense temporal stationarity is assumed. The quantity $\tau \in \mathbb{Z}$ is a lag parameter and $\{\cdot\}^H$ the Hermitian transposition [107, 108]. A transient signal potentially illuminates the array through a vector of filters $\mathbf{h}_t[n] \in \mathbb{C}^M$ via another uncorrelated signal $u_t[n] \sim \mathcal{CN}(0, \sigma_t^2)$. Our objective is to detect the presence of this signal.

3.2.2 Space-Time Covariance Matrices

The space-time covariance matrix of the measurement vector $\mathbf{x}[n]$ is given by $\mathbf{R}[\tau] = \mathcal{E}\{\mathbf{x}[n]\mathbf{x}^H[n-\tau]\}$ of the measurement vector $\mathbf{x}[n]$. In the absence of the transient signal, i.e. for $u_t[n] = 0$, the z transform of the space-time covariance or CSD matrix is expressed as $\mathbf{R}(z) = \sum_\tau \mathbf{R}[\tau]z^{-\tau}$, or simply $\mathbf{R}[\tau] \circ \bullet \mathbf{R}(z)$. The notation with square brackets expresses the dependency on the discrete variable, while the round brackets denote a continuous dependency variable. Based on the system model in Fig. 3.1, as well as (2.29) and (2.32), the parahermitian matrix $\mathbf{R}[\tau]$ can be written as

$$\mathbf{R}(z) = \mathbf{H}(z)\mathbf{H}^P(z) + \sigma_v^2\mathbf{I}, \quad (3.1)$$

where in (3.1), $\mathbf{H}(z) \bullet\!\!\!\circ \mathbf{H}[n]$ represents the transfer function matrix of the mixing system. As introduced in Chap. 2, the parahermitian operator $\{\cdot\}^P$ performs a Hermitian transposition and time reversal, defined as $\mathbf{H}^P(z) = \{\mathbf{H}(1/z^*)\}^H$ [108]. Consequently, $\mathbf{R}(z)$ is a parahermitian matrix satisfying $\mathbf{R}(z) = \mathbf{R}^P(z)$. A polynomial matrix can be interpreted as a matrix-valued polynomial or a polynomial with matrix coefficients, $\mathbf{R}[\tau]$ denoting the coefficient of $z^{-\tau}$. The matrix $\mathbf{R}[\tau]$ can also be understood as a matrix containing cross-correlation sequences of elements between sensor pairs.

In the case of $u_t[n] \neq 0$, the contribution of this signal to the overall CSD matrix is

$$\mathbf{R}_t(z) = \mathbf{h}_t(z)\mathbf{h}_t^P(z), \quad (3.2)$$

where $\mathbf{h}_t(z) \bullet\!\!\!\circ \mathbf{h}_t[n]$. Note that $\mathbf{R}_t(z)$ has rank one and that for the overall CSD matrix, we have $\mathbf{R}(z) + \mathbf{R}_t(z)$.

3.3 Polynomial Subspace Detection

3.3.1 Analytic Eigenvalue Decomposition

Given the signal model in Fig. 3.1, the CSD matrix $\mathbf{R}(z)$ is analytic in the z -transform and admits an analytic EVD [109, 110, 121, 156]. As outlined in Chapter 2, a parahermitian polynomial matrix, therefore, has a parahermitian matrix EVD

$$\mathbf{R}(z) = \mathbf{Q}(z)\mathbf{\Lambda}(z)\mathbf{Q}^P(z). \quad (3.3)$$

In (3.3), $\mathbf{\Lambda}(z) = \text{diag}\{\lambda_1(z), \dots, \lambda_M(z)\}$ is a diagonal parahermitian matrix with analytic eigenvalues $\lambda_m(z)$, $m = 1, \dots, M$ of $\mathbf{R}(z)$. The eigenvectors are the columns of $\mathbf{Q}(z)$, which is also analytic in the z -transform and satisfies the paraunitary property such that $\mathbf{Q}^P(z)\mathbf{Q}(z) = \mathbf{Q}(z)\mathbf{Q}^P(z) = \mathbf{I}_M$. This indicates a lossless filter bank that conserves signal energy at all frequencies and implies that $\mathbf{Q}^{-1}(z) = \mathbf{Q}^P(z)$ as shown in [108]. The analyticity of the factors in (3.3) is essential to approximating $\mathbf{Q}(z)$ closely by polynomials through shift and truncation operations [145, 146, 150, 151, 188–190].

Based on (3.3) and in the absence of a transient signal, we can establish a subspace decomposition,

$$\mathbf{\Lambda}(z) = \begin{bmatrix} \mathbf{\Lambda}_{\parallel}(z) + \sigma_v^2 \mathbf{I}_L & \\ & \sigma_v^2 \mathbf{I}_{M-L} \end{bmatrix} \quad (3.4)$$

$$\mathbf{Q}(z) = \begin{bmatrix} \mathbf{Q}_{\parallel}(z), & \mathbf{Q}_{\perp}(z) \end{bmatrix}, \quad (3.5)$$

where $\mathbf{\Lambda}_{\parallel}(z)$ contain the L analytic eigenvalues of $\mathbf{H}(z)\mathbf{H}^P(z) : \mathbb{C} \rightarrow \mathbb{C}^{L \times L}$, and $\mathbf{Q}_{\parallel}(z)$ includes their corresponding eigenvectors. The orthogonal complement $\mathbf{Q}_{\perp}(z)$, such that $\mathbf{Q}_{\perp}^P(z)\mathbf{Q}_{\parallel}(z) = 0$, consists of analytic eigenvectors that span the noise-only subspace of $\mathbf{R}(z)$. This noise-only subspace excludes any contributions from the stationary sources L .

3.3.2 Subspace Projection and Syndrome Vector

With the partitioning of the analytic EVD factors in (3.4) and (3.5), $\mathbf{Q}_{\perp}(z) \bullet\!\!\!\circ \mathbf{Q}_{\perp}[n]$ describes a lossless filter bank that can be used to project the measurement data vector $\mathbf{x}[n]$ onto the noise-only subspace defined by

$$\mathbf{s}[n] = \sum_{\nu} \mathbf{Q}_{\perp}^H[-\nu] \mathbf{x}[n - \nu], \quad (3.6)$$

where $\mathbf{s}[n] \in \mathbb{C}^{M-L}$ is the projected data vector as shown in Fig. 3.1. In the ideal case, this new signal vector $\mathbf{s}[n]$ remains free of contributions from stationary sources L . However, with the emergence of the transient signal $u_t[n]$, there are now a total of $L + 1$ signals in the environment. Consequently, at least a portion of $u_t[n]$ will project into $\mathbf{s}[n]$, making its presence easier to detect than in the measurements $\mathbf{x}[n]$. Thus, $\mathbf{s}[n]$ is also referred to as a syndrome vector.

Example 6 *To illustrate the detection of a weak transient source using the above polynomial subspace projection technique, the following example simulates a scenario with $L = 3$ stationary sources with complex uncorrelated Gaussian distributions with unit*

variance that illuminate an array of $M = 5$ elements. A random $M \times M$ paraunitary matrix $\mathbf{U}(z)$ of order 5 [108] is partitioned as

$$\mathbf{U}(z) = [\mathbf{H}(z), \mathbf{Q}_\perp(z)] \quad (3.7)$$

where $\mathbf{H}(z) : \mathbb{C} \rightarrow \mathbb{C}^{5 \times 3}$ is the convolutive mixing system for stationary users w.r.t. Fig. 3.1. Additive complex Gaussian noise $\mathbf{v}[n]$ with a power $\sigma_v^2 = 0.01$ is added over an interval of $n \in (0, 5000)$. During an interval $n = (1200, 1800)$, a complex Gaussian transient signal $u_t[n]$ with variance $\mathcal{E}\{u_t[n]\} = 0.1$ is active, and illuminates the array via a random unit-norm vector $\mathbf{h}_t[n]$ of order 5 as shown in Fig. 3.1.

For random realization of signals, Fig. 3.2(a) and (b) show the time series of the first sensor signal and the energy in the data vector, $\|\mathbf{x}[n]\|_2^2$, over time n , respectively. The time interval during which the transient source is active is shaded in gray; notice that there does not appear to be any noticeable energy difference between the inside and the outside of this shaded interval.

With the choice of $\mathbf{H}(z)$ as in (3.7), its complement $\mathbf{Q}_\perp(z)$ can generate the syndrome vector $\mathbf{s}[n] \in \mathbb{C}^2$ according to (3.6). Since $\mathbf{Q}_\perp(z)$ is known by construction, it is ideal in the sense that $\mathbf{s}[n]$ will not contain any components of stationary sources, but only parts of the noise and the transient signal. Figs. 3.3(a) and (b) show the complex-valued time series of the first element of $\mathbf{s}[n]$ and the energy of the syndrome $\|\mathbf{s}[n]\|_2^2$, respectively. Compared to Fig. 3.2, it is now possible to clearly see the difference in energy between the unshaded region, where the transient signal is absent, and the shaded interval, where the transient signal is active.

In [5], the broadband signal $u_{L+1}[n]$ is projected onto the noise-only subspace; this resulting vector has also been called a syndrome vector in [5]. This terminology originates from coding theory, particularly in filter bank-based source channel coding methods [185], where the occurrence of any components in this subspace can indicate the presence of impulse noise and transmission errors. The operation in (3.6) represents a generalization of narrowband subspace detection methods [180] to the broadband

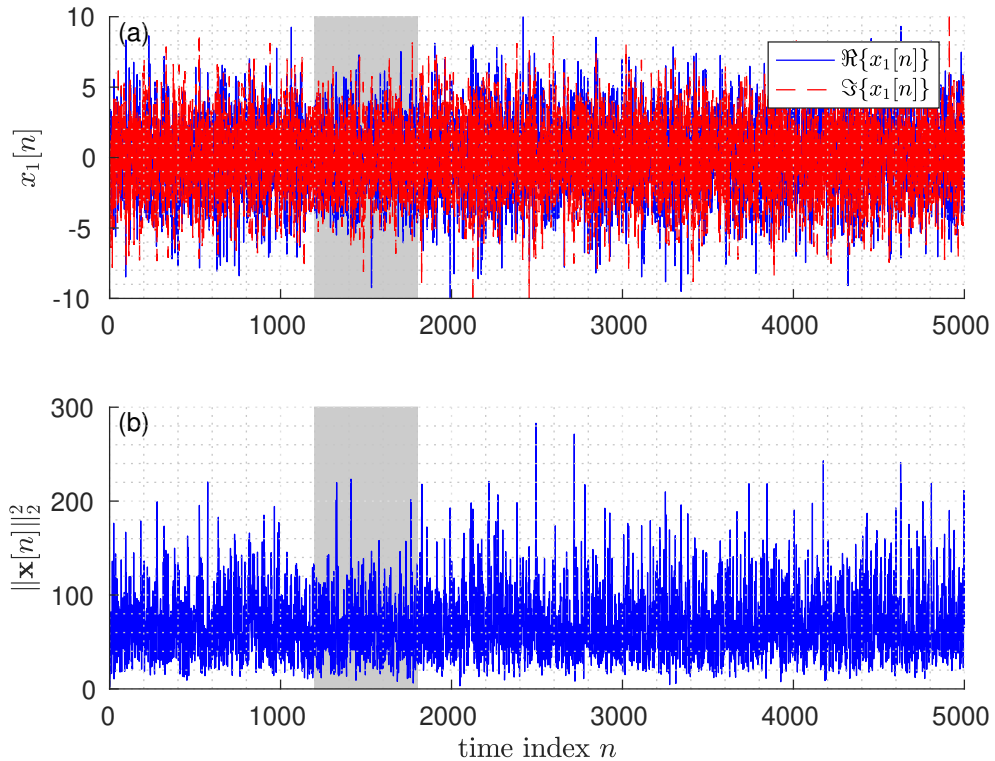


Figure 3.2: Sensor signal with transient signal presented during the interval $n \in (1200, 1800)$: (a) real and imaginary parts of first sensor signal $x_1[n]$, and (b) total sensor energy $\|\mathbf{x}[n]\|_2^2$ across all sensors.

scenario. This approach can be advantageous in applications such as the detection of voice activity in the presence of stronger speakers [134] or noise [133].

If the temporal correlation in $\mathbf{s}[n]$ is ignored, then a detection variable $\|\mathbf{s}[n]\|_2^2$ will follow a generalized χ^2 distribution and forms a surprisingly good discriminator for the presence of a transient source [5]. This holds when $\mathbf{s}[n]$ is a zero-mean Gaussian vector with uncorrelated components. However, the temporal dimension of the filtering operator $\mathbf{Q}_\perp^H[-n]$ introduces temporal correlation even when the input $\mathbf{x}[n]$ is uncorrelated signals. This correlation compromises the statistical independence of the detection variable over time, increasing variance and reducing the contrast between the signal and noise distributions, thus limiting the detection performance. This temporal decorrelation can be partially addressed by averaging a decimated version of the output $\mathbf{s}[nQ]$ [5], where $Q \in \mathbb{N}$ exceeds the period over which $\mathbf{s}[n]$ is temporally correlated.

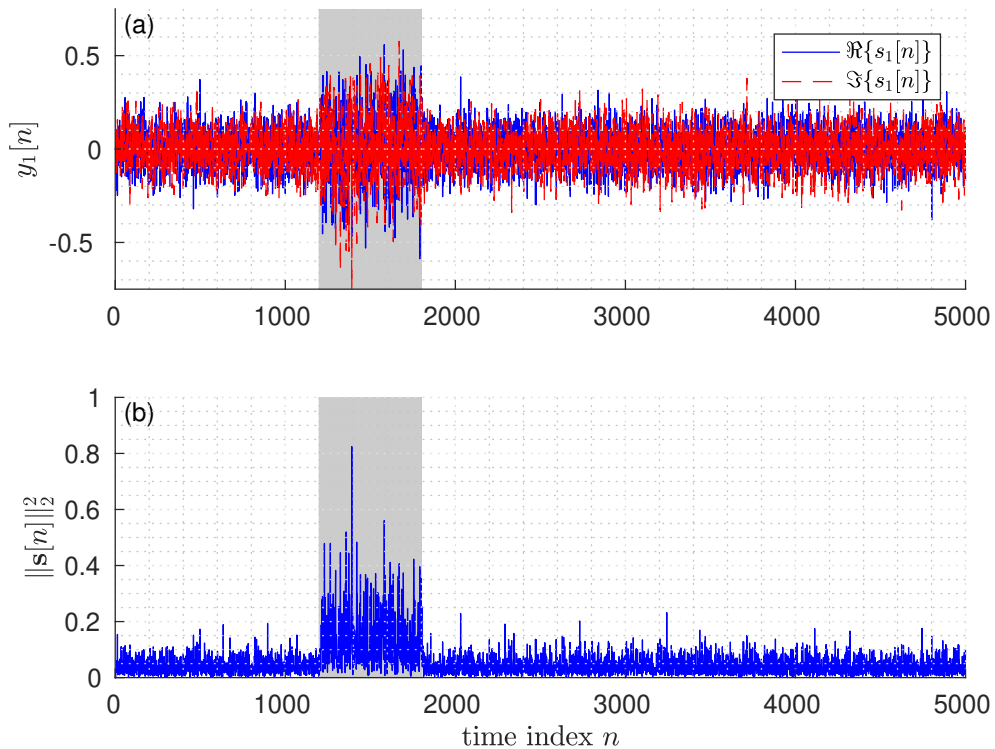


Figure 3.3: Syndrome signal: (a) real and imaginary parts of the first element of $\mathbf{s}[n]$ and (b) energy of the syndrome vector $\|\mathbf{s}[n]\|_2^2$.

3.4 Syndrome Energy

When a new source emerges, its components can extend into the noise-only subspace, allowing for easier detection of energy changes compared to the direct measurement from the measurement $\mathbf{x}[n]$ [5], as the contributions of the stationary source are eliminated. We therefore compute a type of syndrome vector $\mathbf{s}[n] \in \mathbb{C}^{M-L}$ from $\mathbf{Q}_\perp(n) \circ \bullet \mathbf{Q}_\perp[z]$.

The expression in (3.6) represents a projection in a reduced $(M - L)$ dimensional space that preserves the energy in $\mathcal{E}\{\|\mathbf{s}[n]\|_2^2\}$. This is analogous to a standard projection using the operator $\mathbf{P}(z) = \mathbf{Q}_\perp(z)\mathbf{Q}_\perp^P(z)$, which yields the same information, but in a higher-dimensional space. As indicated in Fig. 3.3 of Example 6, the energy of the syndrome $\mathbf{s}[n]$ can help establish the presence or absence of a transient signal, e.g. in a hypothesis test.

3.4.1 Signal Statistics

In the absence of a transient signal, let the CSD matrix of $\mathbf{x}[n]$ be $\mathbf{R}(z)$ as in (3.1); thus, the CSD matrix of the syndrome vector is given by

$$\mathbf{R}_s(z) = \sigma_v^2 \mathbf{I}_{M-L} . \quad (3.8)$$

If $\mathbf{x}'[n]$ is a data vector that includes both stationary sources from $\mathbf{u}[n]$ and a transient signal, then the modified CSD matrix $\mathbf{R}'(z)$,

$$\mathbf{R}'(z) = \mathbf{R}_s(z) + \mathbf{a}'(z)\gamma'(z)\mathbf{a}'^P(z) , \quad (3.9)$$

is generated, where $\mathbf{a}'(z)$ is the vector of the transfer function between the transient source and the sensor array, and $\gamma'(z)$ is the PSD of the transient signal with spectral factorization $\gamma'(z) = b(z)b^P(z)$. Thus, the term $\mathbf{a}'(z)\gamma'(z)\mathbf{a}'^P(z)$ is the contribution of the transient signal as a rank-one structured component added to the noise-only CSD, introducing correlation across the syndrome channels and enabling its detection through subspace-based analysis.

The modified syndrome has the CSD matrix

$$\mathbf{R}'_s(z) = \mathbf{Q}_\perp^P(z)\mathbf{h}_t(z)\mathbf{h}_t^P(z)\mathbf{Q}_\perp(z) + \sigma_v^2 \mathbf{I}_{M-L} , \quad (3.10)$$

where with reference to the model in Fig. 3.1, $\mathbf{h}_t(z) = \mathbf{a}(z)b(z)$. The first term on the right-hand side (rhs) of (3.10) generates the power offset that could allow us to detect the presence of a transient signal.

To analyze the statistics of $\|\mathbf{s}[n]\|_2^2$, we assume that the noise components of $\mathbf{x}[n]$ consist of Gaussian random variables with zero mean and are equally distributed. However, in the presence of transient components or subspace leakage from stationary sources, elements of the syndrome vector show Gaussian distributions with varying variances, resulting in $\|\mathbf{s}[n]\|_2^2$ following a generalized χ^2 distribution [191, 192].

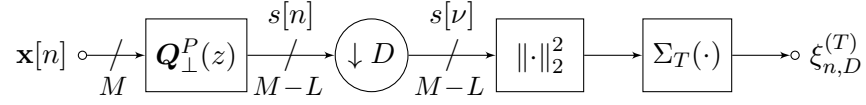


Figure 3.4: Flow graph of decimated averaging of syndrome energy.

3.4.2 Decimated Subspace Detector

The flow graph in Fig. 3.4 illustrates the processing of the syndrome vector. Decimation by D disrupts temporal correlation and reduces complexity, while averaging consecutive syndrome vectors improves discrimination. The factor D decreases the energy of the syndrome before averaging with a sliding window of length T . By applying noble identities [108], the order of the decimator and the processor matrix $\mathbf{Q}_\perp(z)$ can be rearranged, allowing a computationally efficient polyphase implementation compared to the setup depicted in Fig. 3.4.

The energy of decimated syndrome vectors, defined as

$$\xi_{n,D}^{(T)} = \frac{1}{T} \sum_{\mu=0}^{T-1} |\mathbf{s}[n - D\mu]|_2^2, \quad (3.11)$$

allows efficient hypothesis testing by managing large data volumes at high sampling rates and, at the same time, decorrelates consecutive vectors during temporal averaging. Decorrelation through decimation by D of the processor matrix $\mathbf{Q}_\perp(z)$ ensures that $\xi_{n,D}^{(T)}$ follows a generalized distribution χ^2 when temporal correlation is suppressed [193, 194], which helps theoretical predictions for hypothesis testing in $\xi_{n,D}^{(T)}$. Otherwise, if the syndrome vectors contributing to (3.11) are temporally correlated, the distribution is no longer generalized χ^2 .

Example 7 *In order to illustrate the impact effect of the averaging on the syndrome energy, an array of $M = 6$ sensors picks up $L = 3$ independent, temporally uncorrelated Gaussian distributed stationary sources and one transient source of the same variance via convolutive mixing matrices in the presence of additive Gaussian noise at an SNR of 2.5 (≈ 4 dB). The stationary and transient signals are received via convolutive mixing*

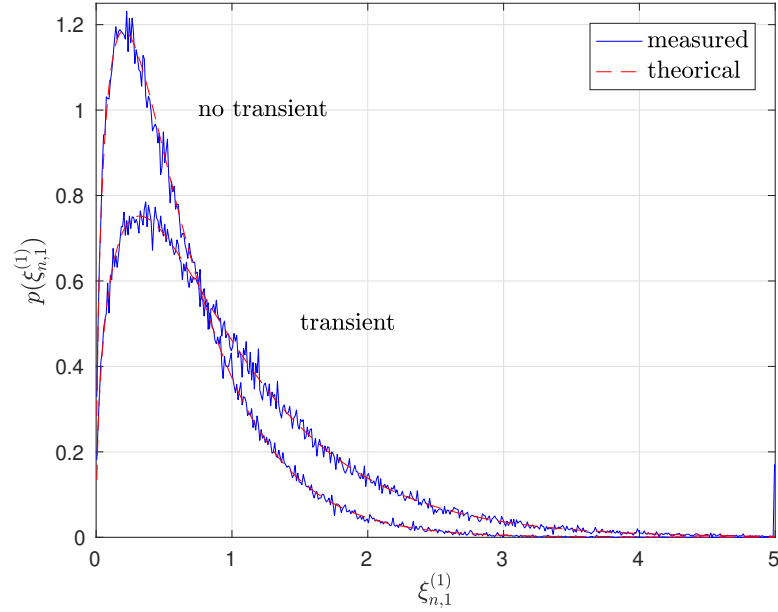


Figure 3.5: Measured and theoretical generalized χ^2 distributions of the energy $\|\mathbf{s}[n]\|_2^2$ for $T = 1$, comparing scenarios with and without a transient signal.

matrices $\mathbf{H}[n]$ and $\mathbf{h}_t[n]$ of order 6. For the syndrome approach, a broadband subspace decomposition is calculated via a polynomial EVD using the SMD algorithm [138] from the space-time covariance matrix in (3.1). Based on subspace partitioning to produce $\mathbf{Q}_\perp(z)$, the experimental and theoretical distributions of the syndrome energy $\|\mathbf{s}[n]\|_2^2$ with and without the transient signal are shown in Fig. 3.5. The measured PDFs are compared to generalized χ^2 distributions based on the known receive powers (i.e. the diagonal components of $\mathbf{R}[0]$ representing the signal powers in the sensors) [193]. If a variable threshold ϑ , $0 < \vartheta < 5$, is applied to energy detection, Fig. 3.6 shows the ROC [51], displaying the correct detection probability versus the false alarm rate for the range of values over which ϑ is varied.

If the syndrome energy is averaged over $T = 10$ snapshots with a decimation ratio of $D = 10$ to avoid most of the temporal correlation imposed by the convolutive mixing matrices and the system $\mathbf{Q}_\perp(z)$, the resulting distributions are shown in Fig. 3.7. These now separate better than for the unaveraged results in Fig. 3.5. Due to the decimation, the averaged syndrome vectors are approximately temporally uncorrelated, and the re-

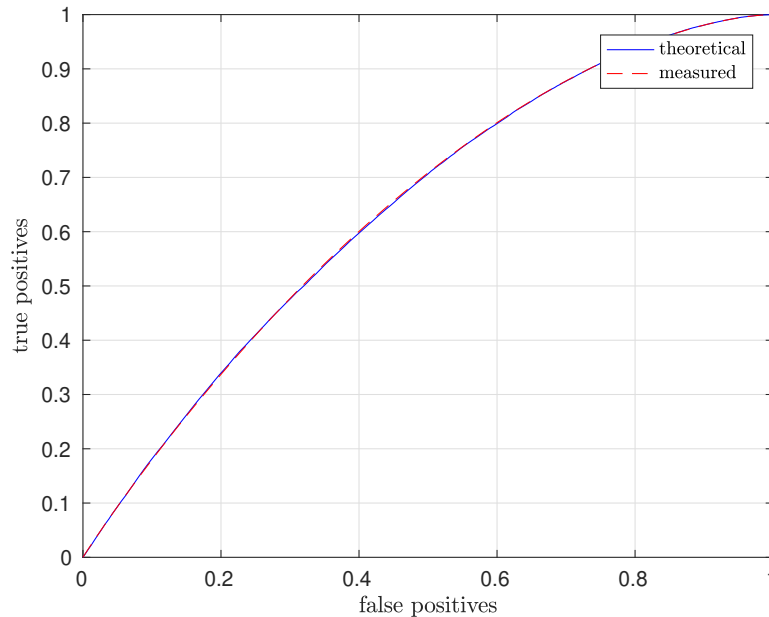


Figure 3.6: Receiver-operating characteristic (ROC) curves showing detection performance under varying false alarm rates.

sulting experimental distributions still closely match the theoretical curves of generalized χ^2 distributions. The ROC curves derived from the PDFs in Fig. 3.7 are displayed in Fig. 3.8. Compared to Fig. 3.6, the better separation of the distributions of the averaged syndrome energies leads to a larger area under the ROC curves in Fig. 3.8.

3.4.3 Performance Metrics

To define metrics for the detection of a transient signal, first a discrimination measure of $\mathcal{D} = 2(1 - A)$ can be derived from the area A under the ROC curve from the distribution plots in Figs. 3.6 and 3.8 [51], without the need for a specific threshold. The area A can assume values between $\frac{1}{2}$ for coinciding distributions and 1 if the distributions are distinct, with \mathcal{D} approaching zero as the distributions become more distinct. Secondly, the decision time defined as $\mathcal{T} = [(T - 1)D + 1]T_s$, with T the number of averaged syndrome vectors, D the decimation ratio, and T_s the sampling period, evaluates the time required to achieve discrimination \mathcal{D} for the variable $\xi_{n,Q}^{(T)}$.

Example 8 *For a scenario with $M = 6$ receive antennas, channel estimates obtained*

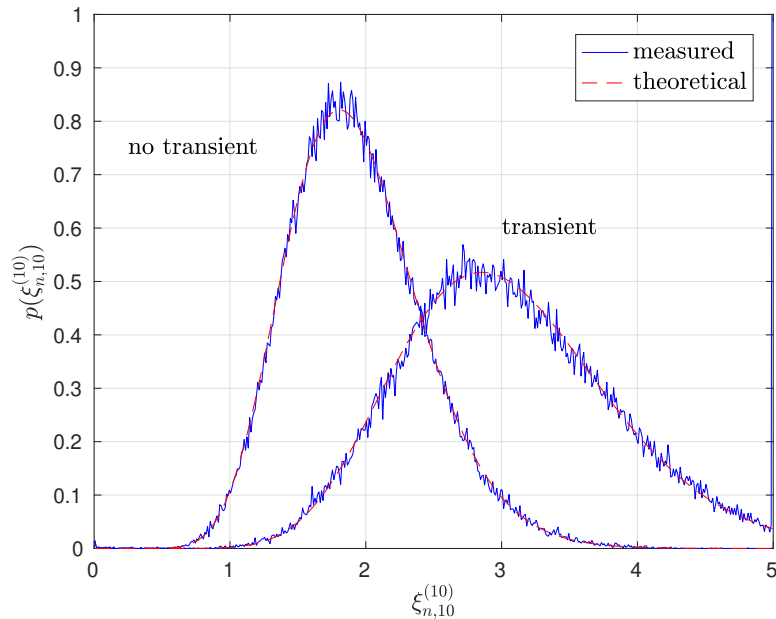


Figure 3.7: Measured and theoretical generalized χ^2 distributions of the energy $\|\mathbf{s}[n]\|_2^2$ for $T = 10$, comparing scenarios with and without a transient signal.

from a radio planning tool in the ISM band with a bandwidth of 20MHz and a sampling period of $T_s = \frac{1}{20} \mu$ in [5] are used to define transfer functions of order 40 from three different sources of different powers characterized in Tab. 3.1. Spatially and temporally uncorrelated Gaussian noise is added at each receiver at 3dB below the weakest source. We derive two scenarios, in which each two sources are stationary, and the remaining source — either the weakest source 3, or the mid-powered source 2 from Tab. 3.1 — provides the transient signal. The CSD matrices are estimated using samples sizes of

Table 3.1: Powers of contributions for a realistic detection scenario, according to simulated channel impulse responses using a radio planning tool [5].

signal	power
source 1	0.000 dB
source 2	-7.380 dB
source 3	-17.190 dB
noise	-20.190 dB

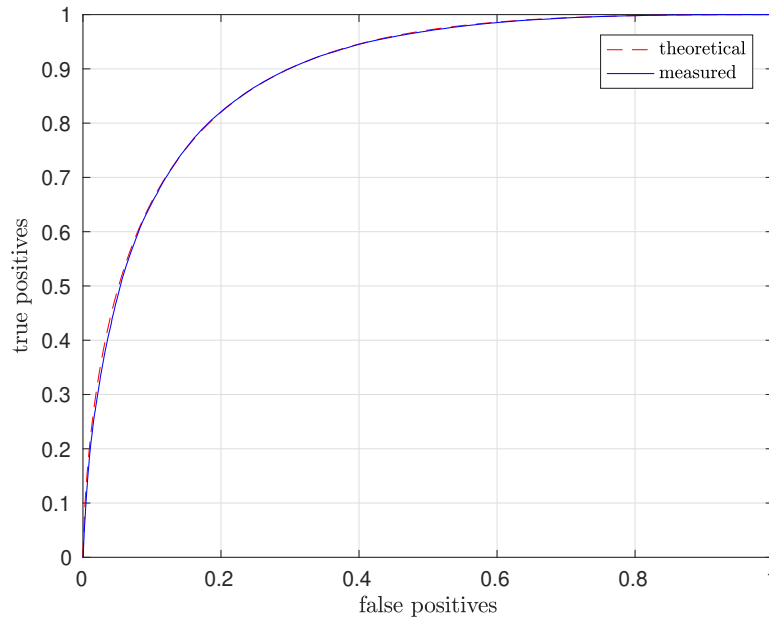


Figure 3.8: Receiver-operating characteristic (ROC) curves showing detection performance under varying false alarm rates.

$N = 10^2, 10^3, 10^4$ [195–197] or are based on the exact channel information ($N \rightarrow \infty$). Any subspace decomposition is obtained via the SMD algorithm [138].

For each of the scenarios with a weak and a medium-powered transient source, Fig. 3.9 shows a group of curves. For the medium-powered transient source, the distributions with the transitory source absent or present separate well, and the discrimination \mathcal{D} drops to close to machine accuracy for small values of T . The CSD matrix estimation results in some subspace leakage [198], but with almost no performance degradation for sample sizes of $N = 10^4$ and $N = 10^3$. Thus, working with an estimate is almost as good as operating with the ground truth CSD matrix. Still, very good discrimination is achieved even when estimating $\hat{\mathbf{R}}(z)$ from a very small sample size of $N = 100$. For the detection time \mathcal{T} , a value of $5 \mu\text{s}$ is equivalent to averaging over $T = 10$ samples at a decimation ratio $D = 10$.

In Fig. 3.9, a second group of curves refers to the weakest source 3 as a transient signal. Compared to the previous case, here a larger value T is required for temporal averaging to achieve better discrimination. The subspace leakage experienced in the

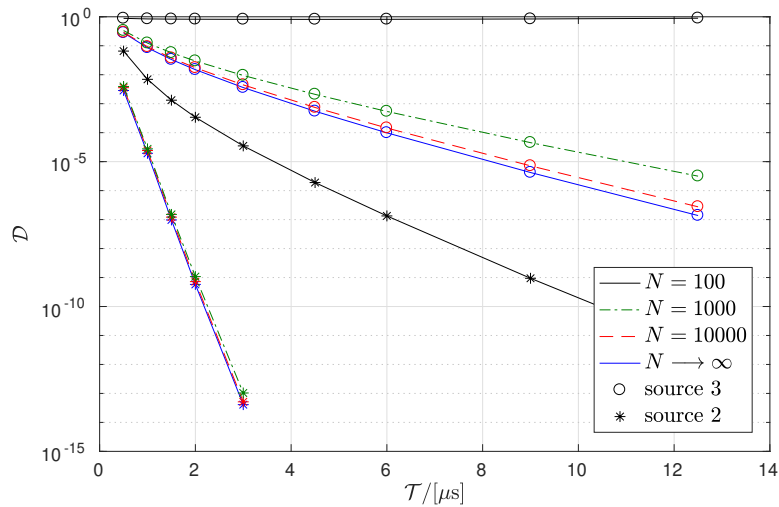


Figure 3.9: Discrimination \mathcal{D} vs decision time \mathcal{T} for detecting transient sources of different strength (medium powered source 2, low-powered source 3), based on estimates of the space-time covariance relying on various sample sizes N .

estimation process is now more pronounced for low sample sizes N , to the extent that the method breaks down for $N = 100$, where the low power of the source and the comparatively high noise level lead to no discernible differences in the distributions.

As the above examples indicate, in the presence of a transient signal, the energy distribution is distinct from the noise-only case. Decimation reduces the sample correlation affected by the transient, enhancing the consistency and detectability of the distortion. This improvement leads to a more apparent statistical difference and better discrimination between transient and non-transient conditions.

3.5 Benchmark Using Likelihood Ratio Test

The previously reported broadband subspace detector, based on a syndrome approach and first introduced in [5], appears to work well for the discussed examples. Therefore, the next step is to compare its performance with that of a known optimal detector, the LRT. Although LRT requires more knowledge of the scenario than the syndrome approach, which relies on the covariance matrix of the transient signal, it can nonetheless provide a useful benchmark. Thus, we use LRT to evaluate the efficacy of the

syndrome-based approach, rather than as a practical method. We aim to determine how closely the syndrome method approaches these theoretical performance limits. We will begin with the LRT formulation.

3.5.1 Likelihood Ratio Test

To compare the subspace test with an LRT, we analyze a decision involving a vector $\mathbf{y}_n \in \mathbb{C}^K$. This vector $\mathbf{y}[n]$ can represent the measurement or syndrome vectors, $\mathbf{x}[n]$ or $\mathbf{s}[n]$, respectively. This vector comprises two components: $\mathbf{y}_{0,n} \in \mathbb{C}^K$, representing stationary noise, and $\mathbf{y}_{1,n} \in \mathbb{C}^K$, indicating a transient signal. Both components are assumed to be zero mean with the covariance matrices \mathbf{R}_0 and \mathbf{R}_1 . The goal is to distinguish between the following two hypotheses

$$\begin{aligned} H_0 : \mathbf{y}_n &= \mathbf{y}_{0,n} ; \\ H_1 : \mathbf{y}_n &= \mathbf{y}_{0,n} + \mathbf{y}_{1,n} . \end{aligned} \quad (3.12)$$

In this thesis, $\mathbf{y}_{0,n}$ represents the contribution of L stationary sources and additive noise. In contrast, $\mathbf{y}_{1,n}$ reflects the components of the transient signal. The PDF for \mathbf{y}_n , under the two hypotheses are defined as

$$p(\mathbf{y}_n | H_0) = (2\pi |\mathbf{R}_0|)^{-\frac{1}{2}} e^{-\frac{1}{2}\mathbf{y}_n^H \mathbf{R}_0^{-1} \mathbf{y}_n} \quad (3.13)$$

$$p(\mathbf{y}_n | H_1) = (2\pi |\mathbf{R}_0 + \mathbf{R}_1|)^{-\frac{1}{2}} e^{-\frac{1}{2}\mathbf{y}_n^H (\mathbf{R}_0 + \mathbf{R}_1)^{-1} \mathbf{y}_n} , \quad (3.14)$$

where $|\cdot|$ denotes the determinant of its matrix-valued argument.

The likelihood ratio $L(\mathbf{y}_n)$ is given by

$$L(\mathbf{y}_n) = \frac{p(\mathbf{y}_n | H_0)}{p(\mathbf{y}_n | H_1)} = \frac{|\mathbf{R}_0 + \mathbf{R}_1|^{\frac{1}{2}}}{|\mathbf{R}_0|^{\frac{1}{2}}} e^{-\frac{1}{2}\mathbf{y}_n^H \mathbf{A} \mathbf{y}_n} , \quad (3.15)$$

where

$$\mathbf{A} = \mathbf{R}_0^{-1} - (\mathbf{R}_0 + \mathbf{R}_1)^{-1} = \mathbf{Q} \mathbf{\Lambda} \mathbf{Q}^H , \quad (3.16)$$

with its EVD $\mathbf{A} = \mathbf{Q}\mathbf{\Lambda}\mathbf{Q}^H$ [120, 199], the likelihood ratio can be expressed further as

$$L(\mathbf{y}_n) = \frac{|\mathbf{R}_0 + \mathbf{R}_1|^{\frac{1}{2}}}{|\mathbf{R}_0|^{\frac{1}{2}}} e^{-\frac{1}{2}\|\mathbf{\Lambda}^{\frac{1}{2}}\mathbf{Q}^H\mathbf{y}_n\|_2^2}. \quad (3.17)$$

To accept or reject the hypothesis, we now need to find a threshold c such that

$$L(\mathbf{y}_n) \underset{H_0}{\overset{H_1}{\geq}} c. \quad (3.18)$$

Rearranging leads to

$$\|\mathbf{\Lambda}^{\frac{1}{2}}\mathbf{Q}^H\mathbf{y}_n\| \underset{H_0}{\overset{H_1}{\geq}} 2 \ln \left\{ \frac{|\mathbf{R}_0|^{\frac{1}{2}}}{|\mathbf{R}_0 + \mathbf{R}_1|^{\frac{1}{2}}} c \right\} = c', \quad (3.19)$$

where c' is a modified threshold. With the term $\|\mathbf{\Lambda}^{\frac{1}{2}}\mathbf{Q}^H\mathbf{y}_n\|$, the test statistic for LRT is defined.

3.5.2 Likelihood Ratio Test on Measurements

Applying the LRT directly to the measurement data $\mathbf{x}[n]$ utilizes all available information. To achieve temporal averaging of the test outcome for the LRT variable \mathbf{y}_n , we concatenate T snapshots of $\mathbf{x}[n]$,

$$\mathbf{y}_n^H = [\mathbf{x}_n^H, \mathbf{x}_{n-1}^H, \dots, \mathbf{x}_{n-T+1}^H], \quad (3.20)$$

such that $\mathbf{y}_n \in \mathbb{C}^{MT}$. For the covariance matrices in Sec. 3.2.2, we introduce extra subscripts to denote their reference to the measurement vector, via $\mathbf{R}_{\mathbf{x},0}$ and $\mathbf{R}_{\mathbf{x},1}$. For hypothesis H_0 , the associated covariance is given by

$$\mathbf{R}_{\mathbf{x},0} = \begin{bmatrix} \mathbf{R}[0] & \dots & \mathbf{R}[T-1] \\ \vdots & \ddots & \vdots \\ \mathbf{R}[1-T] & \dots & \mathbf{R}[0] \end{bmatrix}. \quad (3.21)$$

Similarly, \mathbf{R}_1 can be derived from the lag components of $\mathbf{R}_t[\tau]$ in (3.2).

The matrix $\mathbf{R}_t[\tau]$ has rank one, representing a single transient source through lags. In contrast, the matrix \mathbf{R}_1 , formed by stacking components of lag across multiple time indices, can achieve a rank of up to T [105], reflecting the temporal evolution of the transient signal and providing additional degrees of freedom. Although this distinction improves the temporal structure and detectability, it is not essential for subsequent derivations focusing on the richer information in the time-aggregated representation.

For dimensions, matrices $\mathbf{R}_i \in \mathbb{C}^{(MT) \times (MT)}$, for $i = 0, 1$, pose computational and numerical challenges for inversion at high values of M or T . We typically measure $\mathbf{R}_0 + \mathbf{R}_1$ when the transient signal is present. If we can calculate the inverse \mathbf{R}_0^{-1} , the low-rank update $(\mathbf{R}_0 + \mathbf{R}_1)^{-1}$ can be found using the matrix inversion lemma [120]. This issue will be addressed in Sec. 3.6.

3.5.3 Likelihood Ratio Test Applied to Subspace Data

To apply the LRT to successive samples T of the projected data vector $\mathbf{s}[n]$, we define a variable \mathbf{y}_n , similar to (3.16), as

$$\mathbf{y}_n^H = [\mathbf{s}_n^H, \mathbf{s}_{n-1}^H, \dots, \mathbf{s}_{n-T+1}^H] , \quad (3.22)$$

such that $\mathbf{y}_n \in \mathbb{C}^{(M-L)T}$. For its space-time covariance $\mathbf{R}'[\tau] = \mathcal{E} \{ \mathbf{y}[n] \mathbf{y}^H[n - \tau] \}$ and the corresponding CSD matrix $\mathbf{R}'(z) : \mathbb{C} \rightarrow \mathbb{C}^{(M-L) \times (M-L)}$, we can state

$$\mathbf{R}'(z) = \mathbf{Q}_\perp^P(z) \mathbf{R}(z) \mathbf{Q}_\perp(z) , \quad (3.23)$$

where primed variables refer to syndrome-vector rather than measurement-vector-based quantities. Concerning the CSD matrix of the measurement data, $\mathbf{R}(z)$, we can now obtain $\mathbf{R}_{s,0}$ from the coefficient valued by the matrix of $\mathbf{R}'_t[n] \circ \bullet \mathbf{R}'_t(z)$, similar to the process in Sec. 3.5.2.

For the transient component, we can define

$$\mathbf{R}'_t(z) = \mathbf{Q}_\perp^P(z) \mathbf{R}_t(z) \mathbf{Q}_\perp(z) . \quad (3.24)$$

Based on the rank-one term $\mathbf{R}_t(z)$ in (3.2), and similar to Sec. 3.5.2, we can derive a constant covariance matrix $\mathbf{R}_{s,0}$ from $\mathbf{R}'_t[n] \circ \bullet \mathbf{R}'_t(z)$. In the subspace-based scenario, we now have covariance matrices $\mathbf{R}_{s,i}, i = 0, 1$, of size $T(M - L) \times T(M - L)$.

In Sec. 3.5.2, we address stationary sources and transient signals similarly to the signal-plus-noise subspace of the LRT applied to the measurement data of $\mathbf{R}(z)$. However, for weak transient sources, two benefits emerge: 1) suppressing the dominant eigenvalues of $\mathbf{R}(z)$ in \mathbf{R}' , lowering the condition number of the matrices \mathbf{R}_i , and enhancing the performance of LRT in the syndrome compared to the measurement data; 2) smaller covariance matrices simplify matrix inversions, reducing numerical and computational challenges.

In Sec. 3.3.2, the energy in the syndrome vector, $\|\mathbf{s}[n]\|^2$ treats all components of the noise-only subspace equally, while the LRT weighs the contributions by the term $\Lambda^{\frac{1}{2}}$, accounting for the eigenvalues of the transient source and the additive noise variance σ_v^2 within the noise-only subspace of stationary sources. This means that subspace components with a stronger contribution from the transient signal will receive more weight, distinguishing the heuristic energy of the syndrome approach in [5] and the statistically optimal LRT.

3.5.4 Generalized Likelihood Ratio Test

The application of the LRT test mentioned above to the data typically assumes that the covariance matrices under the two hypotheses are known: \mathbf{R}_0 for hypothesis H_0 and the composite $(\mathbf{R}_0 + \mathbf{R}_1)$ for hypothesis H_1 regardless of whether these matrices are derived from measurements or subspace-projected data. The covariance matrices represent the precise ensemble statistics; the source model in Fig. 3.1 is known a priori. In practice, where only finite data is available for estimating the statistics, the estimated space-time covariance $\hat{\mathbf{R}}(z)$ will be subject to estimation errors that depend both on the sample size of the data and the ground truth $\mathbf{R}(z)$ [195, 200, 201], thus resulting in perturbed estimates $\hat{\mathbf{R}}_0$ and $(\hat{\mathbf{R}}_0 + \hat{\mathbf{R}}_1)$. This reliance on potentially inaccurate estimates turns the LRT into a generalized likelihood ratio test (GLRT).

This thesis explores the optimality of the test. In the application described in Sec. 3.1, we can estimate $\hat{\mathbf{R}}_0$, but we cannot measure $\hat{\mathbf{R}}_1$, independently or in conjunction with $\hat{\mathbf{R}}_0$, before detecting the change points. Understanding the optimal outcomes based on \mathbf{R}_i or $\hat{\mathbf{R}}_i$ serves as a benchmark for [5] and related applications such as [133, 134].

3.6 Analysis of Subspace-Based LRT

In this section, we explore the properties of the covariance matrices $\mathbf{R}_{\mathbf{x},i}$, $i = 0, 1$, which represent the measurements, and of $\mathbf{R}_{\mathbf{s},i}$, $i = 0, 1$, which pertain to the projected data that feed into the LRT discussed in Sec. 3.5.1.

3.6.1 Temporal Correlation

We focus on hypothesis H_0 , where only L stationary signals are present. If the mixing system uses FIR filters of length $(K + 1)$, then $\mathbf{R}(z)$ is a Laurent polynomial matrix of order $2K$, typically dense due to nonzero coefficients $\mathbf{R}[\tau]$ for $|\tau| \leq K$. As a result, when considering a temporal window $T < K$ in the LRT, $\mathbf{R}_{\mathbf{x},0}$ is a dense matrix. Only for the case $T > K$ will we start to see zero corner blocks appearing.

Examining the projected data based on H_0 , we have $\mathbf{R}'(z)$ given by (3.23). With the subspace partitioning in (3.4) and (3.5) this simplifies in the case of an ideal EVD to

$$\mathbf{R}'(z) = \sigma_v^2 \mathbf{I}_{M-L}, \quad (3.25)$$

since the projection is orthogonal to the signal subspace, i.e. $\mathbf{Q}_\perp^P(z)\mathbf{H}(z) = \mathbf{0}$. For the LRT, this leads

$$\mathbf{R}_{\mathbf{s},0} = \sigma_v^2 \mathbf{I}_{(M-L)T}. \quad (3.26)$$

Under hypothesis H_0 , according to (3.26) \mathbf{y}_n is uncorrelated both spatially and temporally, contrasting with $\mathbf{R}_{\mathbf{x},0}$ for the measurement data. Temporal correlation generally degrades a test variable [5], which thus is mitigated for the projected data under hypothesis H_0 .

Under hypothesis H_1 , we examine the covariance matrix $(\mathbf{R}_0 + \mathbf{R}_1)$. Both the measurement and projected data cases will produce dense matrices $\mathbf{R}_{\mathbf{x},1}$ and $\mathbf{R}_{\mathbf{s},1}$, with the input data for the LRT, \mathbf{y}_n , showing temporal and spatial correlations. The projected data, after passing through the filter bank $\mathbf{Q}_\perp^P(z)$, will exhibit correlations over a data window that is even longer than the measurement data.

To construct the matrix \mathbf{A} in (3.16) for the LRT, note that both $\mathbf{R}_t(z)$ and $\mathbf{R}'_t(z)$ are rank-one matrices, as shown by the outer products in (3.2) and (3.24). We can define $\mathbf{R}'_t(z) = \mathbf{Q}_\perp^P(z)\mathbf{h}_t(z)\mathbf{h}_t^P(z)\mathbf{Q}_\perp^P(z) = \mathbf{h}'_t(z)\mathbf{h}_t'^P(z)$ where $\mathbf{h}'_t(z) = \mathbf{Q}^P(z)\mathbf{h}_t(z) : \mathbb{C} \rightarrow \mathbb{C}^{M-L}$ is a vector of functions. As a result of the space-time covariance having rank one, at least theoretically the covariance matrices $\mathbf{R}_{\mathbf{x},1}$ and $\mathbf{R}_{\mathbf{s},0}$ will at most have rank T [105] and can be factorized as

$$\mathbf{R}_{\mathbf{x},1} = \mathbf{H}_t \mathbf{H}_t^H \quad (3.27)$$

$$\mathbf{R}_{\mathbf{s},1} = \mathbf{H}'_t \mathbf{H}'_t^H, \quad (3.28)$$

where $\mathbf{H}_t \in \mathbb{C}^{MT \times T}$ and $\mathbf{H}'_t \in \mathbb{C}^{(M-L)T \times T}$.

Using the Woodbury identity [120] for the low-rank update $(\mathbf{R}_0 + \mathbf{R}_1)^{-1}$, for (3.16) where the low rank term $\mathbf{R}_1 = \mathbf{H}_t \mathbf{H}_t^H$ admits the factorization

$$(\mathbf{R}_0 + \mathbf{H}_t \mathbf{H}_t^H)^{-1} = \mathbf{R}_0^{-1} - \mathbf{R}_0^{-1} \mathbf{H}_t (\mathbf{I}_T + \mathbf{H}_t^H \mathbf{R}_0^{-1} \mathbf{H}_t)^{-1} \mathbf{H}_t^H \mathbf{R}_0^{-1}. \quad (3.29)$$

Substituting this result into (3.16) yields

$$\mathbf{A} = \mathbf{R}_0^{-1} - (\mathbf{R}_0 + \mathbf{H}_1 \mathbf{H}_1^H)^{-1}. \quad (3.30)$$

Replacing the inverse using the Woodbury expansion, we obtain

$$\mathbf{A} = \mathbf{R}_0^{-1} \mathbf{H}_t (\mathbf{I}_T + \mathbf{H}_t^H \mathbf{R}_0^{-1} \mathbf{H}_t)^{-1} \mathbf{H}_t^H \mathbf{R}_0^{-1}. \quad (3.31)$$

Specifically for the measurement case, in (3.31), the dense nature of $\mathbf{R}_{\mathbf{x},0}$ prevents

further simplifications. For the projected data, denoted as \mathbf{A}_s , we have

$$\mathbf{A}_s = \frac{1}{\sigma_v^2} \mathbf{H}'_t (\sigma_v^2 \mathbf{I}_T + \mathbf{H}_t^{H} \mathbf{H}'_t)^{-1} \mathbf{H}'_t{}^H, \quad (3.32)$$

recalling that primed variables such as \mathbf{H}'_t refer to quantities that are projected on the nullspace of $\mathbf{R}(z)$. Although (3.31) and (3.32) do not represent how the processor for the test statistic in (3.19) is computed, since only \mathbf{R}_0 and $(\mathbf{R}_0 + \mathbf{R}_1)$ are available. However, (3.32) illustrates how the projected data case simplifies the procedure by presenting the outer product of a low-rank matrix \mathbf{H}'_t and its regularized left pseudo-inverse, that is free of temporal or spatial correlations imposed by the stationary sources captured in \mathbf{R}_0 .

3.6.2 Covariance Matrix Conditioning

We assess how the computation of the inverses for \mathbf{R}_0 and $(\mathbf{R}_0 + \mathbf{R}_1)$ impacts the application of the LRT to the measurements or projected data by examining the condition number of a matrix [120]. This metric indicates the sensitivity to random perturbations, such as estimation errors [195], during inversion.

In the measurement scenario, the condition number $\mathbf{R}_{\mathbf{x},0}$ is related to the spread of the eigenvalues [179] of the signal, which evaluates the ratio of the minimum and maximum spectral values and incorporates a spatial component. For the maximum eigenvalue, we have

$$\max \{\lambda_{\mathbf{x},0}\} \approx \max_{\Omega, m} \lambda \{ \mathbf{R}(e^{j\Omega}) \} \approx \max_{\Omega, m} \lambda \{ \mathbf{H}(e^{j\Omega}) \mathbf{H}^P(e^{j\Omega}) \} > \sigma_s^2, \quad (3.33)$$

where $\lambda\{\mathbf{R}(z)\}$ returns the analytic eigenvalues of the Parahermitian matrix $\mathbf{R}(z)$ [109], and σ_s^2 represents the maximum power of a stationary source in a measurement $x_m[n]$, assuming an SNR of $\sigma_s^2/\sigma_v^2 \gg 1$ is large. For the smallest eigenvalue, the noise floor in the noise-only subspace is defined by σ_v^2 , allowing us to obtain

$$\gamma_{\mathbf{x},0} > \sigma_s^2/\sigma_v^2 \quad (3.34)$$

for the condition number under hypothesis H_0 . The maximum eigenvalue under H_1 comes from a strong stationary component, while the minimum eigenvalue relates to the noise floor. Thus, we have approximately $\gamma_{\mathbf{x},1} = \gamma_{\mathbf{x},0}$.

In the projected data, ideally, there are no stationary signals. Here, the maximum eigenvalue is represented by

$$\begin{aligned} \max \{ \lambda_{\mathbf{s},0} \} &= \max_{\Omega, m} \lambda \{ \mathbf{R}'(e^{j\Omega}) \} = \max_{\Omega, m} \lambda \{ \mathbf{H}_t(e^{j\Omega}) \mathbf{H}_t^P(e^{j\Omega}) + \sigma_v^2 \mathbf{I}_{T(M-L)} \} \\ &> \sigma_t^2 + \sigma_v^2, \end{aligned} \quad (3.35)$$

where σ_t^2 represents the maximum power of the transient signal within any of the measurement signals $x_m[n]$. Note that this power does not increase when passing through $Q^P(z)$, since this matrix is paraunitary and hence it preserves energy. Because the smallest eigenvalue remains constrained by the noise floor, we have $\gamma_{\mathbf{s},0} > 1$ and

$$\gamma_{\mathbf{s},1} > \frac{\sigma_t^2 + \sigma_v^2}{\sigma_v^2} \quad (3.36)$$

for the condition number under hypotheses H_0 and H_1 . Note that the transient signal is significantly weaker than the stationary signals; the covariance matrices for the projected data will have a much lower bound for the condition number and will generally be much better conditioned than their equivalent quantities based on the measurement data.

3.7 Generalised Likelihood Ratio Test Implementation

The construction of Generalised LRT follows closely that of an LRT, but uses estimated covariance matrices instead of the expected ones. This section highlights the general approach in Sec. 3.7.1 followed by details on the covariance estimation in Sec. 3.7.2, and the mean and variance of this estimators in Secs. 3.7.3 and 3.7.4.

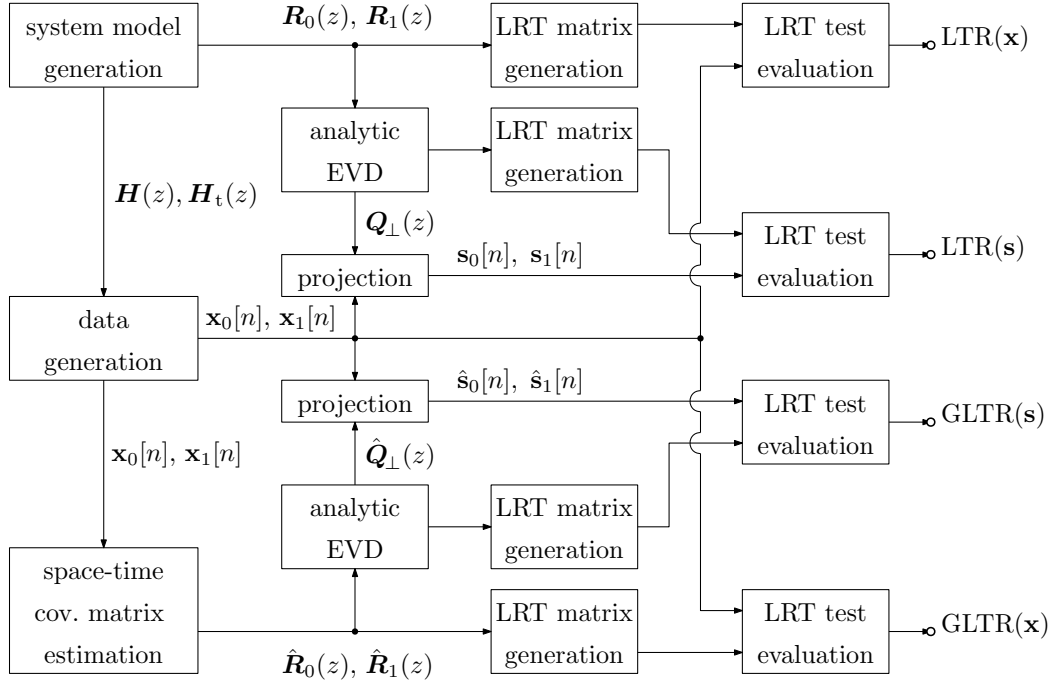


Figure 3.10: Block diagram for LRT/GLRT implementation.

3.7.1 Implementation Overview

The block diagram in Fig. 3.10 illustrates how ultimately results for LRT and for GLRT are obtained. Based on generated system components $\mathbf{H}(z)$ and $\mathbf{H}_t(z)$ as in Fig. 3.1, we can derive the space-time covariance matrices under the different hypotheses. From this, LRT test matrices $\mathbf{A}^{\frac{1}{2}} = \mathbf{\Lambda}^{\frac{1}{2}} \mathbf{Q}^H$ are built via (3.21) according to (3.16). With these test matrices, LRT test statistics (LRT(\mathbf{x})) based on the measurement data are produced with data generated from the source models $\mathbf{H}(z)$ and $\mathbf{H}_t(z)$. This is illustrated by the top branch in Fig. 3.10. In the same block diagram, an analytic EVD of the space-time covariance matrices leads not only to the subspace decomposition that allows the syndrome vector calculation via \mathbf{Q}_\perp , but also the modified covariance matrices from which syndrome-based LRT test statistics (LRT(\mathbf{s})) can be calculated.

By repeating the same procedures with estimated space-time covariances, the bottom half of the block diagram in Fig. 3.10 shows how the statistics for the generalised LRTs (GLRT(\mathbf{x}) and GLRT(\mathbf{s})) can be determined in the same fashion as the LRT

results. Thus, we will focus in more detail on space-time covariance estimation below.

3.7.2 Cross-Correlation Estimation

The space-time covariance matrix must be estimated from the data. If only a set of N snapshots of $\mathbf{x}[n], n = 0 \dots (N - 1)$ is available. Generally, the estimate for the space-time covariance matrix, $\hat{\mathbf{R}}[\tau]$, will experience estimation errors. We aim to focus on estimating the cross-correlation sequence.

The cross-correlation sequence between two signals $x_m[n]$ and $x_\mu[n]$, with $m, \mu \in \{1, \dots, M\}$, is defined as

$$r_{m\mu}[\tau] = \mathcal{E} \{x_m[n]x_\mu^*[n - \tau]\}. \quad (3.37)$$

Assuming strong ergodicity and therefore by implication stationarity for the signals involved [202], the estimation of $r_{m\mu}[\tau]$ over a set of N time snapshots can be performed in different ways.

3.7.3 Unbiased Estimation

The space-time covariance matrix consists of cross-correlation sequences, and we use a best linear unbiased estimator (BLUE) [195]. With lag-dependent normalization, the estimate of $r_{m\mu}[\tau]$ over a sample size N is defined as

$$\hat{r}_{m\mu}[\tau] = \begin{cases} \frac{1}{N-|\tau|} \sum_{n=0}^{N-|\tau|-1} x_m[n+\tau]x_\mu^*[n], & \tau \geq 0, \\ \frac{1}{N-|\tau|} \sum_{n=0}^{N-|\tau|-1} x_m[n]x_\mu^*[n-\tau], & \tau < 0, \end{cases} \quad (3.38)$$

which can be shown to be unbiased. For example, for $\tau \geq 0$,

$$\text{mean} \{\hat{r}_{m\mu}[\tau]\} = \mathcal{E} \{\hat{r}_{m\mu}[\tau]\} = \frac{1}{N-|\tau|} \sum_{n=0}^{N-|\tau|-1} \mathcal{E} \{x_m[n]x_\mu^*[n-\tau]\} \quad (3.39)$$

$$= \frac{1}{N-|\tau|} \sum_{n=0}^{N-|\tau|-1} r_{m\mu}[\tau] = r_{m\mu}[\tau], \quad (3.40)$$

i.e., the quantity estimated via (3.38) tends towards the true cross-correlation sequence.

3.7.4 Variance of Estimator

With a lag-dependent normalization, an estimate of $r_{m\mu}[\tau]$ in (3.38) over a sample size N is defined as

$$\text{var} \{ \hat{r}_{m\mu}[\tau] \} = \mathcal{E} \{ (\hat{r}_{m\mu}[\tau] - r_{m\mu}[\tau]) (\hat{r}_{m\mu}[\tau] - r_{m\mu}[\tau])^* \} \quad (3.41)$$

$$\begin{aligned} &= \mathcal{E} \{ \hat{r}_{m\mu}[\tau] \hat{r}_{m\mu}^*[\tau] \} - \mathcal{E} \{ \hat{r}_{m\mu}[\tau] \} r_{m\mu}^*[\tau] \\ &\quad - r_{m\mu}[\tau] \mathcal{E} \{ \hat{r}_{m\mu}^*[\tau] \} + r_{m\mu}[\tau] r_{m\mu}^*[\tau] \end{aligned} \quad (3.42)$$

$$= \mathcal{E} \{ \hat{r}_{m\mu}[\tau] \hat{r}_{m\mu}^*[\tau] \} - r_{m\mu}[\tau] r_{m\mu}^*[\tau]. \quad (3.43)$$

Inserting the estimation in (3.38) into $\mathcal{E} \{ \hat{r}_{m\mu}[\tau] \hat{r}_{m\mu}^*[\tau] \}$ results in (3.43) containing a fourth-order term involving the signals $x_m[n]$ and $x_\mu[n]$.

The fourth-order term above can be expressed in terms of cumulants, but for Gaussian signals, cumulants of order three and above are zero [203, 204]. This property also holds for the complex-valued case [205], such that this fourth-order term simplifies as

$$\mathcal{E} \{ x_m[n] x_\mu^*[n-\tau] x_m^*[n] x_\mu[n-\tau] \} = \mathcal{E} \{ x_m[n] x_\mu^*[n-\tau] \} \cdot \mathcal{E} \{ x_m^*[n] x_\mu[n-\tau] \} \quad (3.44)$$

$$+ \mathcal{E} \{ x_m[n] x_m^*[n] \} \cdot \mathcal{E} \{ x_\mu^*[n-\tau] x_\mu[n-\tau] \} \quad (3.45)$$

$$+ \mathcal{E} \{ x_m[n] x_\mu[n-\tau] \} \cdot \mathcal{E} \{ x_\mu^*[n-\tau] x_m^*[n] \}. \quad (3.46)$$

Therefore, for $\tau \geq 0$, the variance of the estimator in (3.38) becomes

$$\begin{aligned} \text{var} \{\hat{r}_{m\mu}[\tau]\} &= \frac{1}{(N - |\tau|)^2} \sum_{n,\nu=0}^{N-|\tau|-1} (\mathcal{E} \{x_m[n + \tau]x_\mu^*[n]\} \cdot \mathcal{E} \{x_m^*[\nu + \tau]x_\mu[\nu]\} \\ &\quad + \mathcal{E} \{x_m[n + \tau]x_m^*[\nu + \tau]\} \mathcal{E} \{x_\mu^*[n]x_\mu[\nu]\} \\ &\quad + \mathcal{E} \{x_m[n + \tau]x_\mu^*[\nu]\} \mathcal{E} \{x_\mu^*[n]x_\mu[\nu]\} - r_{m\mu}[\tau]r_{m\mu}^*[\tau]) \end{aligned} \quad (3.47)$$

$$\begin{aligned} &= \frac{1}{(N - |\tau|)^2} \sum_{n,\nu=0}^{N-|\tau|-1} (\mathcal{E} \{x_m[n]x_m^*[\nu]\} \cdot \mathcal{E} \{x_\mu^*[n]x_\mu[\nu]\} \\ &\quad + \mathcal{E} \{x_m[n]x_\mu[\nu - \tau]\} \mathcal{E} \{x_m^*[\nu]x_\mu^*[n - \tau]\}) . \end{aligned} \quad (3.48)$$

The same outcome can be obtained for $\tau < 0$, and it matches the results obtained in [206]. Note that the first term on the r.h.s. of (3.48) can be simplified as

$$\begin{aligned} \sum_{n,\nu=0}^{N-|\tau|-1} \mathcal{E} \{x_m[n]x_m^*[\nu]\} \cdot \mathcal{E} \{x_\mu^*[n]x_\mu[\nu]\} &= \sum_{n,\nu=0}^{N-|\tau|-1} r_{mm}[n - \nu] \cdot r_{\mu\mu}^*[n - \nu] \\ &= \sum_{t=-N+|\tau|+1}^{N-|\tau|-1} (N - |\tau| - |t|) r_{mm}[t] \cdot r_{\mu\mu}^*[t] \end{aligned} \quad (3.49)$$

$$(3.50)$$

The second term in (3.48) can be addressed similarly. With $\bar{r}_{m\mu}[\tau] = \mathcal{E} \{x_m[n]x_\mu[n - \tau]\}$ denoting the complementary cross-correlation sequence [205], the variance of the sample cross-correlation sequence becomes [195, 197]

$$\begin{aligned} \text{var} \{\hat{r}_{m\mu}[\tau]\} &= \frac{1}{(N - |\tau|)^2} \sum_{t=-N+|\tau|+1}^{N-|\tau|-1} (N - |\tau| - |t|) \\ &\quad \cdot (r_{mm}[t]r_{\mu\mu}^*[t] + \bar{r}_{m\mu}[\tau + t]\bar{r}_{m\mu}^*[\tau - t]) . \end{aligned} \quad (3.51)$$

Thus, for Gaussian input signals, we can characterize the variance of the cross-correlation sequence estimator, which depends on the sample size but also on the underlying auto- and cross-correlation sequences. Further, if the data is complex-symmetric Gaussian,

then all complementary cross-correlation terms are zero [205]. This provides some insight into the perturbation of the estimates required for the GLRT in Sec. 3.5.4 and its implementation in Sec. 3.7.1.

3.8 Simulation Results

This chapter compares three tests: the simple syndrome approach from Sec. 3.3.2, the LRT using measurement data from Sec. 3.5.2, and the syndrome-based LRT based on Sec. 3.5.3.

3.8.1 Performance Metrics, Algorithms, and Parameters

We evaluated the separation of distributions related to two hypotheses using the ROC metric. The ROC evaluates the probability of correctly detecting a transient signal versus the false alarm of incorrectly detecting a transient signal, i.e., with respect to the test in (3.19), the threshold c' is exceeded in the absence of any transient signal.

To measure how well two distributions with means μ_0 and μ_1 , and standard deviations σ_0 and σ_1 , separate under hypotheses H_0 and H_1 , we define the distance metric [46]

$$\delta = \frac{|\mu_1 - \mu_0|}{(\sigma_0 + \sigma_1)/2} \quad (3.52)$$

as a single value to characterize the effectiveness of separation. The normalisation by the mean standard deviation in (3.52) ensures that the spread of the distributions is considered when assessing the distance of their mean values.

The simulation parameters for the example scenario model in Fig. 3.1 are outlined for our test setup. We operate with $M = 8$ sensors and $L = 5$ stationary sources. The transient signal is within the noise floor, with a power equal to the variance σ_v^2 of additive noise $\mathbf{v}[n]$ in Fig. 3.1. The SNR γ of stationary sources and noise, excluding any transient source, is

$$\gamma = \frac{\text{tr}\{\mathbf{R}[0]\} - M\sigma_v^2}{M\sigma_v^2}. \quad (3.53)$$

With $\text{tr}\{\cdot\}$ the trace operator, in (3.53) $\text{tr}\{\mathbf{R}[0]\}$ measures the total signal power in the

received signals, while $M\sigma_v^2$ accounts for the sum of noise power across all sensors. This SNR γ is set to 10 dB or 20 dB. We also vary the order of the convolutive mixing system, with $K = 8$ or $K = 16$. The parameters $M = 8$ and $L = 5$ were selected to ensure an overdetermined sensing configuration ($M > L$), thereby guaranteeing sufficient spatial degrees of freedom for reliable covariance-based processing. The SNR values of 10 dB and 20 dB represent moderate and high signal to noise regimes, respectively, enabling evaluation of performance robustness across practical operating conditions. The trace operator is employed in the SNR definition to quantify total received signal power across the array in a spatially invariant manner. The convolutive mixing order $K \in \{8, 16\}$ models short and moderate channel memory effects, allowing assessment of algorithm robustness under increasing multipath complexity. The simple syndrome energy detector will be compared with a likelihood ratio test [186, 187], which requires significantly more knowledge of the scenario, as the covariance of the contribution of the transient signal to $x[n]$ must be known. The tests involve two variable parameters: the temporal window T and the dispersive of the mixing systems, indicated by the time domain support of $\mathbf{H}[n]$ and $\mathbf{h}_t[n]$, represented by the length K of their finite impulse response filters, as seen in Fig. 3.1.

We evaluated LRT for measurements and syndromes, labeled $\text{LRT}(\mathbf{x})$ and $\text{LRT}(\mathbf{s})$. To address the supervision of temporal correlation in the syndrome method [5], we refer to LRT using only $\mathbf{R}[0]$ and $\mathbf{R}_t[0]$, termed $\text{LRT}_2(\mathbf{x})$, i.e., it also ignores the temporal correlation of the data. Furthermore, we present results using space-time covariance matrices estimated from 10^3 and 10^5 samples through a BLUE [195], demonstrating the performance of a GLRT compared to a conventional LRT [187].

3.8.2 Simulation

Fig. 3.11 illustrates the separability δ , defined in (3.52), for various temporal windows $T = 1, \dots, 10$. For $T = 1$, there is no temporal correlation to consider, and both $\text{LRT}(\mathbf{x})$ and $\text{LRT}_2(\mathbf{x})$ show identical performance. As T increases, both methods rely on increased averaging, which improves separability; incorporating the relevant temporal

Table 3.2: Simulation parameters for the mixing system

Parameter	Value
Polynomial order, K	8, 16, and 20
Signal-to-noise ratio, γ	10 dB or 20 dB
Temporal window, T	1 to 10
Number of stationary sources	5
Transient source power: same as noise power σ_v^2	
Number of snapshots of data N	10^5

correlation leads to a more significant increase in δ for $\text{LRT}(\mathbf{x})$ than for $\text{LRT}_2(\mathbf{x})$. The results indicated by the circles reflect the statistics estimated from the 10^5 data snapshots rather than the signal model in Fig. 3.1, which therefore represents the GLRT test. The covariance matrices are sufficiently accurate to reveal no significant difference compared to the scenario where the ground truth is available (indicated by asterisks).

In comparison, syndrome-based methods exhibit greater separability for $T = 1$ than tests that operate on $\mathbf{x}[n]$. Given that $\text{LRT}(\mathbf{x})$ is statistically the optimal approach, this finding is surprising and likely arises from the temporal decorrelation associated with the stationary sources used by $\mathbf{Q}_\perp(z)$. However, as T increases, the performance advantage of $\text{LRT}(\mathbf{s})$ over $\text{LRT}(\mathbf{x})$ decreases, and the latter demonstrates the best performance for $T > 5$ in this context. Interestingly, the syndrome approach [5], which differs from $\text{LRT}(\mathbf{s})$ by not weighting contributions in the noise-only subspace or considering temporal correlation, performs well and significantly better than $\text{LRT}_2(\mathbf{x})$; once again, the decorrelating property of $\mathbf{Q}_\perp(z)$ may provide an advantage.

Since δ is a simplified assessment of the separation of the distributions, Fig. 3.12 illustrates the ROC curve for $T = 10$. The LRT approach has an advantage because it considers all available data in the measurements $\mathbf{x}[n]$ instead of the pre-processed syndrome $\mathbf{s}[n]$. The estimates of the covariance matrix in Figs. 3.11 and 3.12 are accurate enough to prevent performance drop.

3.8.3 Changing SNR and Support of Mixing System

To strengthen the argument that the use of the preprocessed syndrome vector $\mathbf{Q}_\perp(z)$ is beneficial in the presence of temporal correlation, we enhance this correlation by doubling the support of $\mathbf{H}(z)$ to $K = 16$. The results on separability in Fig. 3.13 show that the performance gap increases compared to Sec. 3.8.2. Furthermore, in the range $0 < T \leq 10$, the LRT applied directly to the measurement data no longer matches the performance of the syndrome-based LRT, as illustrated by the ROC curve for $T = 10$ in Fig. 3.14.

In the previous simulation, the difference in performance between LRT based on precise knowledge and GLRT based on estimated covariance matrices was negligible. In Fig. 3.15, a performance breakdown occurs for GLRT using the measurement data for $T > 8$. Here, for $T = 10$, the matrix \mathbf{R}_0 for LRT(\mathbf{s}) is 30×30 , while for LRT(\mathbf{x}), it is 80×80 , with a condition number that increases by three orders of magnitude compared to the case based on syndromes. Consequently, estimation errors tend to have a more severe impact, potentially leading to poor performance results.

In addition to increasing K regarding the experiment in Sec. 3.8.2, we also increase the power of the stationary sources from $\gamma = 10$ dB to $\gamma = 20$ dB. This has the effect of increasing the condition number of the covariance matrices based on $\mathbf{x}[n]$ but not the condition number of the covariance matrix based on $\mathbf{s}[n]$, where the large eigenvalues of the stationary users have been removed. Consequently, it becomes more challenging for LRT(\mathbf{x}) to extract information about the transient source from the signal subspace of stronger stationary sources. Taking into account the separability results in Fig. 3.15, the reason why it cannot perform as well as LRT(\mathbf{s}) is probably due to the decorrelating nature of $\mathbf{Q}_\perp(z)$. Together, these effects improve the advantage of the proposed LRT(\mathbf{s}) over LRT(\mathbf{x}). Note that while the simplistic measure δ suggests a marginally better separation for the syndrome approach in [5] than for LRT(\mathbf{x}) in $T = 10$, the ROC curve in Fig. 3.16 reveals somewhat reverse fortunes when considering the actual distributions, with LRT(\mathbf{x}) outperforming the syndrome approach at least as far as the logarithmic plot permits to judge this. However, this does not affect the superior performance of

LRT(\mathbf{s}) over LRT(\mathbf{x}).

For the setting with $K = 10$ and the transient signal 10 dB below the stationary signal in power, the results for the separability δ as defined in (3.52) are shown in Fig. 3.17 as a function of the temporal window $T, 1 \leq T \leq 10$. For small values of T , the decorrelating property of $\mathbf{Q}_{\perp}^{\text{P}}(z)$ gives an advantage to the LRT operating on the projected data. Evaluating the power of the projected data averaged over T snapshots, as done in [5, 133, 134] and denoted as power(s) in Fig. 3.17, also offers an advantage over the LRT applied directly to the measurement data. However, as T increases, the LRT for the measurement data surpasses those of the other methods by leveraging additional information about the transient source within the signal-plus-noise subspace. Increasing the temporal correlation with $K = 20$ and reducing the transient signal strength to match the noise floor, Fig. 3.18(a) illustrates the separability. The LRT applied to the measurements performs significantly worse compared to the LRT on the projected data across the T range. Notably, for $T > 8$, the GLRT measurement results decline sharply. For instance, at $T = 10$, the LRT involves inverting 80×80 matrices for the measurement case versus 30×30 matrices for the projected data. Additionally, the condition numbers $\gamma_{\mathbf{x},1}$ and $\gamma_{\mathbf{s},1}$ defined in Sec. 3.6.2 shows significant deviations. These deviations become evident in Fig. 3.18(b) for $T > 8$, correlating with the observed decline in the measurement LRT in Fig. 3.18(a).

3.9 Chapter Summary

This chapter presented a polynomial subspace detection method for weak, broadband transient signals. The syndrome energy approach was evaluated within a polynomial matrix framework and benchmarked against the likelihood ratio test (LRT), which served as the optimal detector under full channel knowledge. A broadband subspace projection was employed as a preprocessing step for the LRT, improving both the computational efficiency and the conditioning of the covariance matrix. Statistical analysis and simulations demonstrated favorable trade-offs in detection performance, decision time, and sample size. Subspace methods outperformed LRT in some scenarios, partic-

ularly when applied directly to the data $\mathbf{x}[n]$, producing better-conditioned estimates than those based on complete transient statistics $\mathbf{R}_1(z)$. We perform energy detection in the noise-only subspace, where the removal of strong signal components may make it easier to recognise the presence of a weak transient source. This detection approach was motivated by the goal of detecting trigger signals of improvised explosive devices (IEDs). Once we have detected a potential hostile source, we would like to suppress it using jamming, as described in the next chapter.

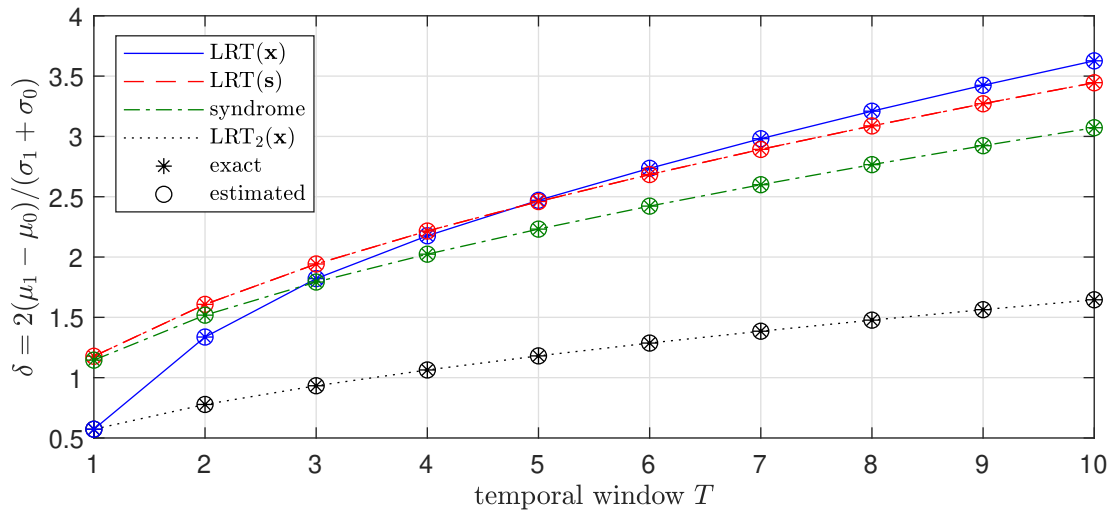


Figure 3.11: Separability of distributions for different approaches with $M = 8$ sensors, $L = 5$ stationary sources, a mixing system of order $K = 8$, and an SNR $\gamma = 10$ dB .

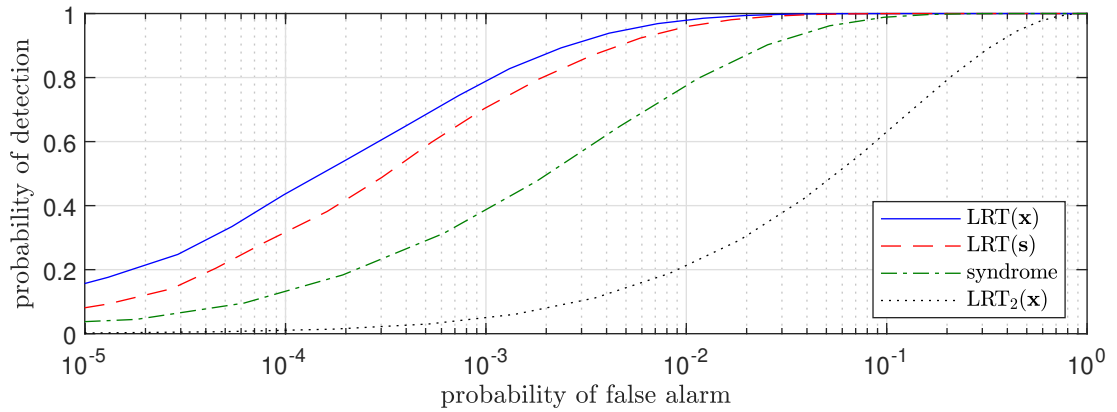


Figure 3.12: ROC curve for the case $T = 10$ in Fig. 3.11.

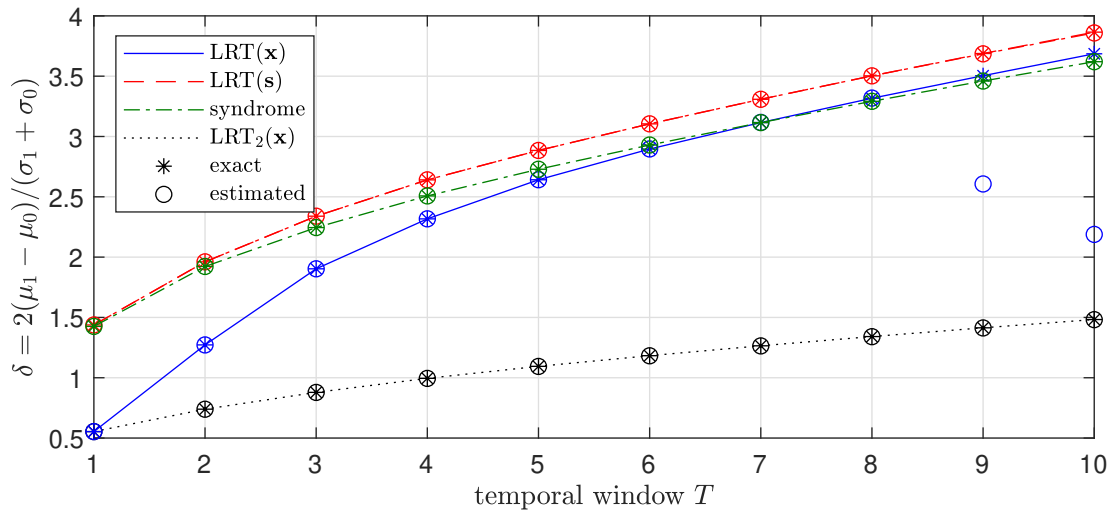


Figure 3.13: Separability with mixing matrix order $K = 16$ compared to Fig. 3.11.

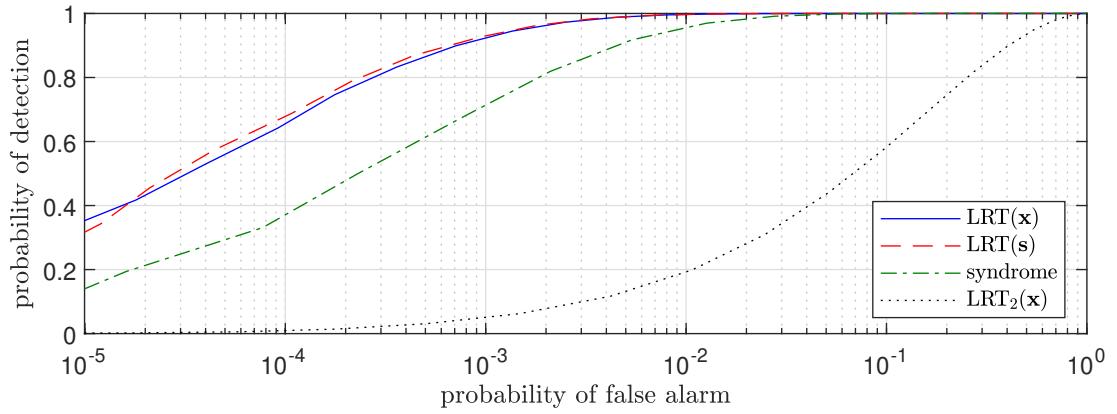


Figure 3.14: ROC curve for the case $T = 10$ in Fig. 3.13.

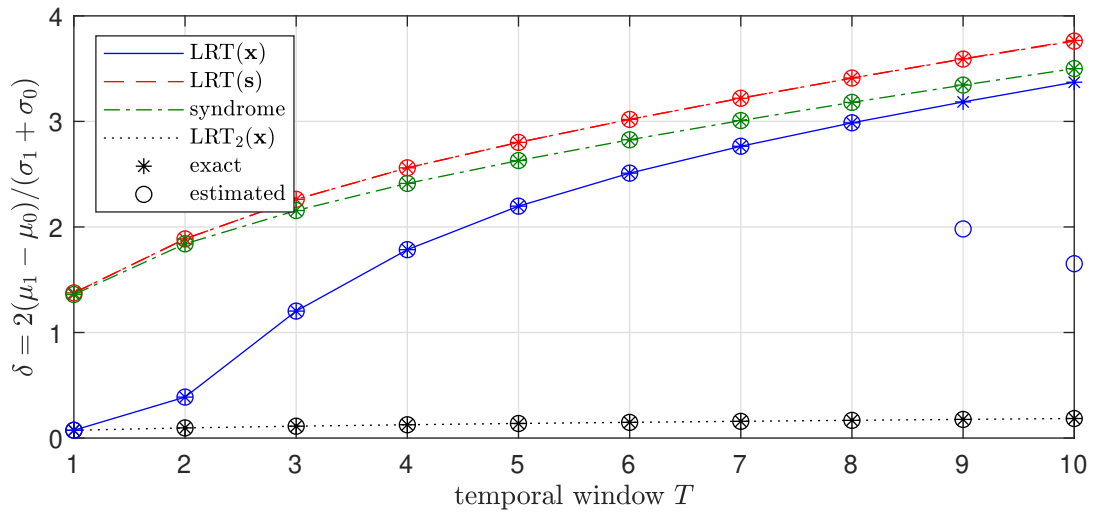


Figure 3.15: Separability with $K = 16$ and SNR $\gamma = 20$ dB compared to Fig. 3.11.

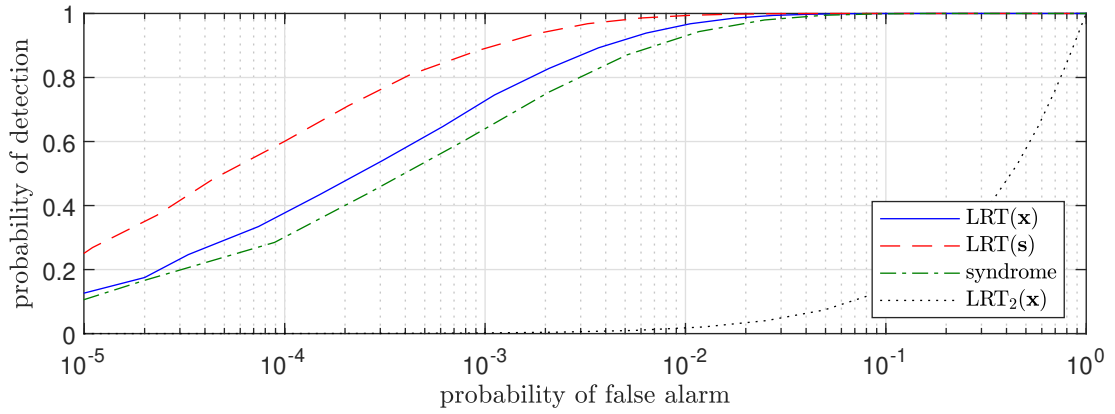


Figure 3.16: ROC curve for the case $T = 10$ in Fig. 3.15.

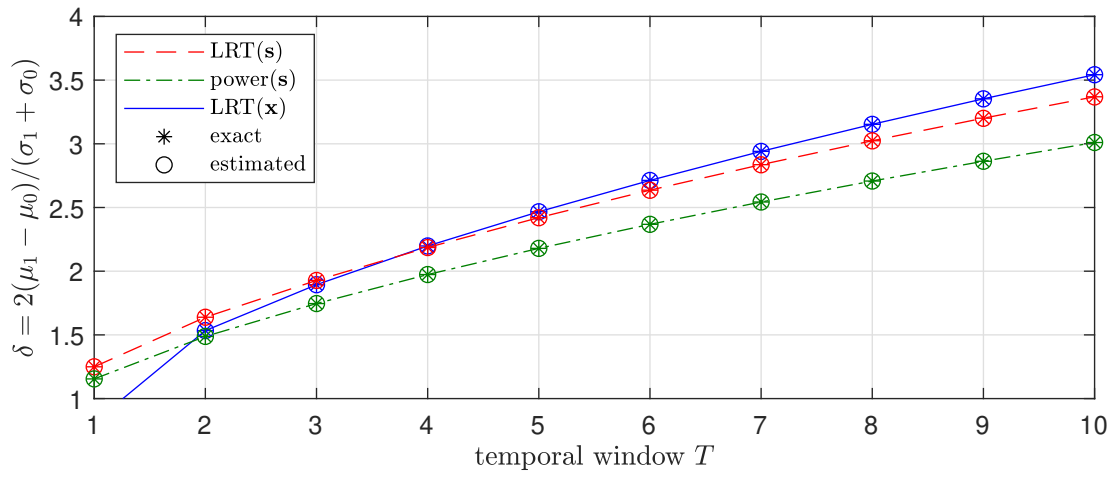


Figure 3.17: Separability of distributions for setting with $K = 10$ and the transient source 10 dB below the stationary sources.

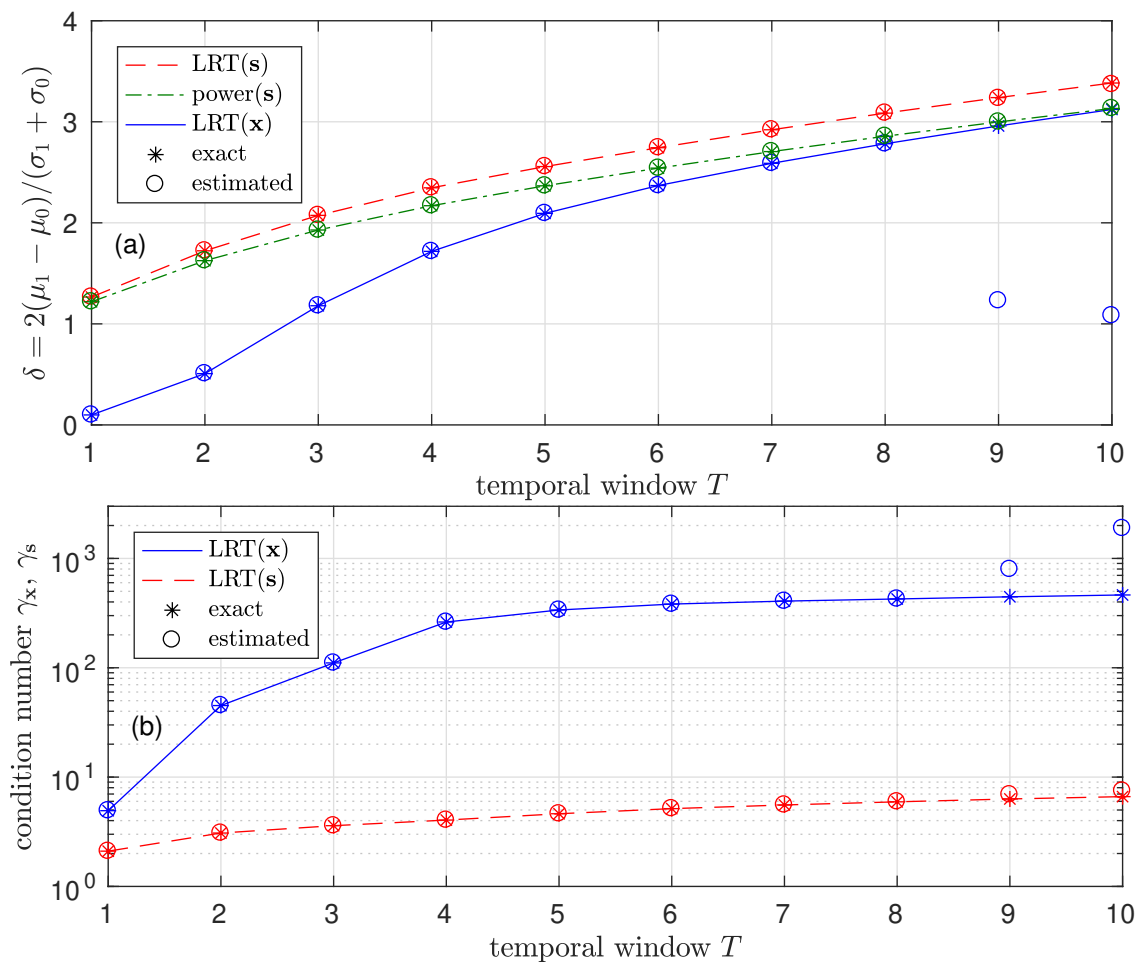


Figure 3.18: (a) Separability of distributions and (b) condition numbers of covariance matrices for setting with $K = 20$ and the transient source 20 dB below the stationary sources.

Chapter 4

Time Reversal Methods to Enable and Protect Primary Users

4.1 Introduction

The preceding Chapter 3 has introduced a polynomial subspace detector for weak transient signals in broadband, addressing the challenges posed by low-energy and short-duration signals often encountered in transient source detection [5, 44]. Building on the detection framework in [5, 44], we develop a signal that effectively blocks these potentially hostile or unauthorized transient sources, using channel reciprocity, also known as time reversal [207]. Time-reversal techniques exploit this reciprocity and have been applied in various propagation media ranging from sonar [208], to radio frequencies [209], biomedical imaging and therapy [210], and human recognition [211]. In this chapter, we adapt time-reversal techniques to serve as a broadband jamming method for MIMO systems. The proposed strategy assumes prior detection of hostile emitters through their earlier transmissions and then exploits channel reciprocity to redirect signal energy back to the source, effectively jamming it.

Time reversal [212–214] is to time-reverse, normalize, and retransmit received sig-

nals so that they concentrate energy back at the original emitter’s location. It accurately targets transmitting sources with the appropriate spatio-temporal structure to maximize power transfer from the transmit array to hostile emitters while minimizing interference with known users in the environment. Moreover, it avoids the requirement for full [215] or at least partial channel knowledge [216] that is often assumed in jammer design.

When full channel knowledge is available, narrowband downlink beamforming methods for MIMO systems [217–219] can be extended to the broadband case. This extension utilizes an analytic SVD [156] of the MIMO system’s transfer function matrices. Although broadband scenarios introduce complexity due to frequency-dependent channel behavior, we show that, under simplified assumptions, this adapted approach can define the performance limits of time-reversal signal processing.

The remainder of this chapter is organized as follows. Sec. 4.2 outlines the weak transient signal detection approach and the optimization problem behind the interference task. This optimization problem requires the maximization of output power, which we characterize via an innovation filter model in Sec. 4.3. Sec. 4.4 discusses the design of the broadband beamforming, while Sec. 4.5 explores the time-reversal method, which is evaluated in Sec. 4.6. A summary is provided in Sec. 4.7.

4.2 Scenario and Signal Model

4.2.1 Reception and Transient Signal Detection

Consider a scenario that contains a group of L_1 stationary transmitters and potentially L_2 transient sources that we aim to detect. The stationary transmissions are received by an array of elements M , represented by the measurement vector $\mathbf{x}_r[n]$. We model stationary contributions to $\mathbf{x}_r[n]$ via an innovation filter $\mathbf{G}_1[n] \in \mathbb{C}^{M \times L_1}$, which is excited by a complex uncorrelated complex Gaussian process with zero mean, unit variance $\mathbf{u}_{r,1}[n] \in \mathbb{C}^{L_1}$, with $\mathbf{u}_{r,1}[n] \in \mathcal{CN}(\mathbf{0}, \mathbf{I})$ [112]. The array is corrupted by additive Gaussian noise $\mathbf{v}[n] \in \mathcal{CN}(\mathbf{0}, \sigma_v^2 \mathbf{I})$, where σ_v^2 is the uncorrelated noise power, and \mathbf{I} [220]

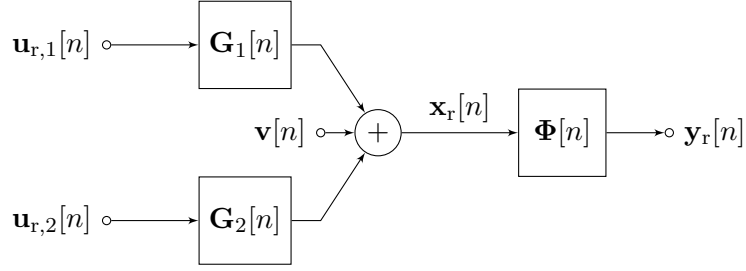


Figure 4.1: Signal model for an M element array with measurement vector $\mathbf{x}_r[n]$, with a processor $\Phi[n]$ to observe an potential transient contributions from $\mathbf{u}_{r,2}[n]$ in the presence of stationary signals $\mathbf{u}_{r,1}[n]$.

for the identity matrix. It may also receive signals from transient sources L_2 , modelled by $\mathbf{u}_{r,2}[n] \in \mathbb{C}^{L_2}$ and an innovation filter $\mathbf{G}_2[n] \in \mathbb{C}^{M \times L_2}$. This situation is shown in Fig. 4.1, which represents the reception stage of the proposed framework and is a reframing of the model in Fig. 3.1 of Chapter 3 using the variables used here: the received measurement vector $\mathbf{x}_r[n]$ contains stationary-users, the potential transient source contribution, as well as additive noise. The processor $\Phi[n]$ projects $\mathbf{x}_r[n]$ away from the subspace occupied by the stationary users, such that $\mathbf{y}_r[n]$ represents the syndrome vector of Chapter 3. The purpose of this chapter will be to use $\mathbf{y}_r[n]$ to project energy back to the transient sources while minimising or ideally nulling the interference to the stationary users.

To detect the presence of transient sources, a processor $\Phi[n]$ in Fig. 4.1 projects onto the nullspace of $\mathbf{G}_1^P(z)$ with $\mathbf{G}_1(z) = \sum_n \mathbf{G}_1[n]z^{-n}$, or simply $\mathbf{G}_1(z) \bullet \circ \mathbf{G}_1[n]$. As a result, $\mathbf{y}_r[n]$ ideally contains only contributions from noise and transient sources. The detection of these sources can be identified by an increase in power [5, 44].

The nullspace of such a matrix of transfer functions can be found using polynomial matrix algebra [105, 121] via an analytic SVD [121, 156], as outlined for subspace decompositions in Chapter 2,

$$\mathbf{G}_1(z) = \mathbf{U}_1(z)\mathbf{\Sigma}_1(z)\mathbf{V}_1^P(z), \quad (4.1)$$

where $\mathbf{U}_1(z) : \mathbb{C} \rightarrow \mathbb{C}^{M \times M}$ and $\mathbf{V}_1(z) : \mathbb{C} \rightarrow \mathbb{C}^{L_1 \times L_1}$ are analytic paraunitary matrices,

and $\mathbf{\Sigma}_1(z) : \mathbb{C} \rightarrow \mathbb{C}^{M \times L_1}$ is diagonal and analytic [5, 121]. As outlined in Chapter 2, paraunitarity implies that $\{\mathbf{U}_1(z)\}^{-1} = \mathbf{U}_1^P(z) = \{\mathbf{U}_1(1/z^*)\}^H$ with $\{\cdot\}^P$ representing the parahermitian transposition [108]. For the computation of (4.1), dedicated SVD algorithms [166, 168, 221] or two analytic EVDs [145, 146, 150, 222] can be invoked.

If $\mathbf{U}_{1,\parallel}(z)$ contains the L_1 left-singular vectors of $\mathbf{G}_1(z)$ corresponding to its non-zero singular values, then its orthogonal complement is $\mathbf{U}_{1,\perp}(z)$, such that the subspace partitioning $\mathbf{U}_1(z) = [\mathbf{U}_{1,\parallel}(z), \mathbf{U}_{1,\perp}(z)]$ enables us to construct the processor matrix as

$$\mathbf{\Phi}(z) = \mathbf{U}_{1,\perp}^P(z) . \quad (4.2)$$

For the space-time covariance of the received data vector, $\mathbf{R}_r[\tau] = \mathcal{E} \{ \mathbf{y}_r[n] \mathbf{y}_r^H[n - \tau] \}$, we now have $\mathbf{R}_r(z) \bullet\text{-}\circ \mathbf{R}_r[\tau]$

$$\mathbf{R}_r(z) = \mathbf{\Phi}(z) \mathbf{G}_2(z) \mathbf{G}_2^P(z) \mathbf{\Phi}^P(z) + \sigma_v^2 \mathbf{I} . \quad (4.3)$$

The first term on the right-hand side (rhs) reflects the power change that the emergence of a transient signal triggers in $\mathbf{y}_r[n]$. Its onset can be identified via a change detection, particularly when $\mathbf{u}_{r,2}[n]$ represents weak transient signals [5].

If $\mathbf{G}_2[n]$ is known, weak transient signal detection can rely on enhanced detectors such as the LRT. The assumption of perfect knowledge of $\mathbf{G}_2[n]$ is often idealized, as in practice it must be estimated, and any mismatch can degrade detection performance. Likewise, accurate characterization of the polynomial mixing model $\mathbf{G}_1^P(z)$ is essential for reliable nullspace construction; model uncertainties, finite-sample effects, and noise may distort this nullspace and cause leakage of strong stationary components. Nevertheless, in structured settings-such as calibrated sensor arrays or controlled communication systems-these parameters can often be estimated with sufficient accuracy, making nullspace projection effective for suppressing dominant interference and enhancing sensitivity to weak transient signals. In this case, restricting to the nullspace of $\mathbf{G}_1^P(z)$ can be advantageous both from the numerical [44] and computational aspects [46]. For simplicity, we define $\mathbf{G}_2(z)$ to lie in the nullspace of $\mathbf{G}_1^P(z)$ so that we

have

$$\mathbf{G}_1^P(z)\mathbf{G}_2(z) = \mathbf{0} \quad (4.4)$$

This implies that L_2 and $\mathbf{u}_{r,2}[n]$ only represent the number and innovations of the transient source components that reside within the nullspace of $\mathbf{G}_1^P(z)$.

Example 9 *As an example for the orthogonality condition in (4.4), assume a matrix $\mathbf{G}_1(z)$,*

$$\mathbf{G}_1(z) = \begin{bmatrix} \sqrt{2} & \frac{1+2z^{-1}+z^{-2}}{\sqrt{2}} \\ -1 & \frac{1+2z^{-1}+z^{-2}}{2} \\ z^{-1} & -\frac{z^{-1}+2z^{-2}+z^{-3}}{2} \end{bmatrix} = \frac{1}{2} \underbrace{\begin{bmatrix} \sqrt{2} & \sqrt{2}z^{-1} \\ -1 & z^{-1} \\ 1 & -z^{-1} \end{bmatrix}}_{\mathbf{U}_1(z)} \underbrace{\begin{bmatrix} 1 & 0 \\ 0 & \frac{z+2+z^{-1}}{2} \end{bmatrix}}_{\mathbf{\Sigma}_1(z)}, \quad (4.5)$$

where the factors $\mathbf{U}_1(z)$, $\mathbf{\Sigma}_1(z)$ and $\mathbf{V}_1(z) = \mathbf{I}_2$ represent its reduced analytic SVD. Note that the columns of $\mathbf{U}_1(z)$ are orthogonal, i.e. that $\mathbf{U}_1^P\mathbf{U}_1(z) = \mathbf{I}_2$. Now assume that we have second matrix $\tilde{\mathbf{G}}_2(z) = (1+z^{-1})[1, 1, 1]^H$ for a single transient user. Then we obtain the matrix $\mathbf{G}_2(z)$ as defined above via the projection $\mathbf{P}(z) = \{\mathbf{I}_3 - \mathbf{U}_1(z)\mathbf{U}_1^P(z)\}$, such that

$$\mathbf{G}_2(z) = \mathbf{P}(z)\tilde{\mathbf{G}}_2(z) = \frac{1+2z^{-1}+z^{-2}}{2} \begin{bmatrix} 0 \\ z \\ 1 \end{bmatrix}. \quad (4.6)$$

Note that because $\mathbf{P}(z)$ is a Laurent polynomial matrix, $\mathbf{G}_2(z)$, different from $\tilde{\mathbf{G}}_2(z)$, now contains non-causal filters.

With $\mathbf{G}_2[n] \circ\!\!\!\circ \mathbf{G}_2(z)$ and $\tilde{\mathbf{G}}_2[n] \circ\!\!\!\circ \tilde{\mathbf{G}}_2(z)$ we find that $\sum_n \|\tilde{\mathbf{G}}_2[n]\|_{\mathbb{F}}^2 = 6$ but $\sum_n \|\mathbf{G}_2[n]\|_{\mathbb{F}}^2 = 3$, i.e. that half of the energy of the transient source falls into the signal-plus-noise subspace of $\mathbf{G}_1^P(z)$ and is ignored for the purposes of maintaining assumption (4.4), while half of the transient source's energy will be captured in the syndrome vector.

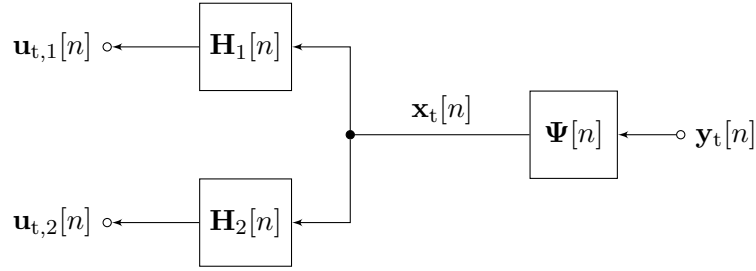


Figure 4.2: Signal model of the same M element array as in Fig. 4.1, but with the aim of maximum power transfer to the transient sources represented in $\mathbf{u}_{t,2}[n]$ while not interfering with the stationary sources represented by $\mathbf{u}_{t,1}[n]$. Compared to Fig. 4.1, the signals flow from right to left.

4.2.2 Transmission and Channel Reciprocity

Channel reciprocity implies that the impulse response from a point A to a point B is the same as the impulse response from B to A , because the multipath components are identical. For a MIMO system, an additional transposition of the MIMO channel matrix is involved if reciprocity holds. We now exploit this fact and aim to reverse the transmission link compared to Sec. 4.2.1 and use the MIMO system matrices $\mathbf{H}_1(z)$ and $\mathbf{H}_2(z)$, as illustrated in Fig. 4.2, to transmit from the M -element array to stationary users, as well as to any potentially present transient sources. The channel reciprocity means that for $\mathbf{H}_1(z) \bullet \circ \mathbf{H}_1[n]$, we have

$$\mathbf{H}_1[n] = \mathbf{G}_1^T[n], \quad (4.7)$$

and similarly, for $\mathbf{H}_2(z) \bullet \circ \mathbf{H}_2[n] = \mathbf{G}_2^T[n]$. The aim is the inverse of that in Sec. 4.2.2: we aim to maximize the transfer of power to the jammer while ideally suppressing the transient sources represented by $\mathbf{u}_{t,2}[n]$, while not interference with the stationary sources indicated by $\mathbf{u}_{t,1}[n]$. Thus, the optimization problem can be formulated as maximizing the energy transfer to $\mathbf{u}_{t,2}[n]$ in order to jam the transient users. This is subject to enforcing the stationary users to remain interference-free, and to maintaining an overall power budget P_0 for the transmission. Therefore, the overall goal is to solve

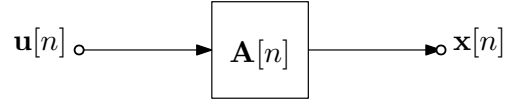


Figure 4.3: Model to explain the spatio-temporal correlation structure of a signal vector $\mathbf{x}[n]$ based on a spatially and temporally uncorrelated input vector $\mathbf{u}[n]$ and a spatio-temporal filter $\mathbf{A}[n]$.

the constrained optimization problem

$$\Psi_*(z) = \arg \max_{\Psi(z)} \mathcal{E} \left\{ \|\mathbf{u}_{t,2}[n]\|_2^2 \right\} \quad (4.8)$$

$$\text{s.t.} \quad \mathcal{E} \left\{ \|\mathbf{u}_{t,1}[n]\|_2^2 \right\} = 0 \quad (4.9)$$

$$\mathcal{E} \left\{ \|\mathbf{x}_t[n]\|_2^2 \right\} = P_0 \quad (4.10)$$

for the preprocessor matrix $\Psi[z] \bullet \rightarrow \Psi(n)$ in Fig. 4.2. Within this optimization problem, (4.8) maximizes the jamming power at the transient source, while (4.9) imposes nulls in the direction of stationary users, and (4.10) ensures that the transmit power constraint is limited to a transmit power budget P_0 .

4.3 Signal Power Based on Innovation Filter Model

In order to address the optimization problem in (4.8) to (4.10), we need to formulate the power of a vector of signals based on its innovation model [112], i.e. we need to tie the signal vector via a MIMO system to a vector of spatially and temporally uncorrelated unit variance zero mean Gaussian signal. This situation is depicted in Fig. 4.3, where $\mathbf{u}[n]$ with $\mathcal{E}\{\mathbf{u}[n]\mathbf{u}^H[n-\tau]\} = \mathbf{I}\delta[\tau]$ contains the inputs, and $\mathbf{A}[n]$ is a matrix of innovation filters that then explains the spatio-temporal structure of a signal vector $\mathbf{x}[n]$ whose power we are interested in.

For an innovation system $\mathbf{A}[n]$ excited by a signal vector $\mathbf{u}[n] \in \mathcal{CN}(\mathbf{0}, \mathbf{I})$, the output $\mathbf{x}[n] = \mathbf{A}[n] * \mathbf{u}[n]$ has the power

$$\mathcal{E} \left\{ \mathbf{x}^H[n]\mathbf{x}[n] \right\} = \text{tr} \left\{ \mathcal{E} \left\{ \mathbf{x}[n]\mathbf{x}^H[n] \right\} \right\} = \text{tr} \left\{ \mathbf{R}_x[0] \right\}, \quad (4.11)$$

which can thus be tied to the zero lag component of the space-time covariance matrix $\mathbf{R}_{\mathbf{x}}[\tau] = \mathcal{E} \{ \mathbf{x}[n] \mathbf{x}^H[n - \tau] \}$ of $\mathbf{x}[n]$. Its z -transform, the CSD matrix $\mathbf{R}_{\mathbf{x}}(z) \bullet \circ \mathbf{R}_{\mathbf{x}}[\tau]$, according to (2.29) is given by

$$\mathbf{R}_{\mathbf{x}}(z) = \mathbf{A}(z) \mathbf{A}^P(z) . \quad (4.12)$$

Thus, the power $\mathcal{E} \{ \mathbf{x}^H[n] \mathbf{x}[n] \}$ can be computed via

$$\xi_{\mathbf{x}} = \text{tr} \{ \mathbf{R}_{\mathbf{x}}[0] \} = \text{tr} \left\{ \sum_n \mathbf{A}[n] \mathbf{A}^H[n] \right\} = \sum_n \text{tr} \{ \mathbf{A}[n] \mathbf{A}^H[n] \} . \quad (4.13)$$

Since the trace $\text{tr} (\mathbf{A} \mathbf{A}^H) = \|\mathbf{A}\|_{\text{F}}^2$ can be related to the Frobenius norm $\|\cdot\|_{\text{F}}$, we obtain

$$\mathcal{E} \{ \mathbf{x}^H[n] \mathbf{x}[n] \} = \sum_n \|\mathbf{A}[n]\|_{\text{F}}^2 = \frac{1}{2\pi} \int_0^{2\pi} \|\mathbf{A}(e^{j\Omega})\|_{\text{F}}^2 d\Omega , \quad (4.14)$$

whereby the latter step exploits Parseval's theorem.

Based on the analytic SVD $\mathbf{A}(z) = \mathbf{U}(z) \mathbf{\Sigma}(z) \mathbf{V}^P(z)$, where $\mathbf{U}(z)$ and $\mathbf{V}(z)$ are paraunitary matrices, and $\mathbf{\Sigma}(z)$ is diagonal with the analytic singular values $\sigma_m(z)$ of $\mathbf{A}(z)$, we thus find that

$$\|\mathbf{A}(e^{j\Omega})\|_{\text{F}}^2 = \sum_m |\sigma_m(e^{j\Omega})|^2 . \quad (4.15)$$

Integrating over frequency Ω , or summing over the time domain coefficient based on Parseval, gives

$$\xi_{\mathbf{x}} = \sum_{n,m} |\sigma_m[n]|^2 \quad (4.16)$$

for the total power of $\mathbf{x}[n]$ based on the singular values $\sigma_m(z) \bullet \circ \sigma_m[n]$ of the innovation filter model $\mathbf{A}[n]$ explaining the spatio-temporal structure of $\mathbf{x}[n]$. We will use this link in Secs. 4.4 and 4.5 to determine the power terms in the optimization problem

(4.8) to (4.10).

4.4 Power Transfer with Known Channel

If the system $\mathbf{H}_2(z)$, that includes the channel matrix and any filters that explain the spatio-temporal correlation structure of the sources we seek to jam, is known, then the problem outlined by (4.8) - (4.10) is in parts a broadband extension of the narrowband MIMO downlink schemes referenced in e.g. [217, 223, 224]. This method designs $\Psi[n] \circ\bullet \Psi(z) = \Psi_1(z)\Psi_2(z)$ in two parts: the matrix $\Psi_1(z)$ is designed in Sec. 4.4.1 to null interference to desired users, while $\Psi_2(z)$ in Sec. 4.4.2 maximizes the power transfer to $\mathbf{u}_{t,2}[n]$.

4.4.1 Broadband Null Steering

First, the constraint (4.9) is enforced by restricting the design to the null space of $\mathbf{H}_1(z)$. Due to channel reciprocity [208, 209], we can write the analytical SVD of $\mathbf{H}_1(z)$ based on the factorization of $\mathbf{G}_1(z)$ in (4.1) as

$$\mathbf{H}_1(z) = \{\mathbf{V}_1(1/z^*)\}^* \Sigma_1^T(z) \mathbf{U}_1^T(z). \quad (4.17)$$

Thus, the null space of $\mathbf{H}_1(z)$ is spanned by those of rows of $\mathbf{U}_1^T(z)$ that correspond to zero singular values, that is, the columns of $\mathbf{U}_{1,\perp}^P(z)$. Therefore, in an initial step, we consider the preprocessor

$$\Psi_1(z) = \{\mathbf{U}_{1,\perp}^P(z)\}^T \quad (4.18)$$

shown in Fig. 4.2. This matrix serves as a broadband beamformer that positions nulls in the direction of sources indicated by $\mathbf{u}_{t,1}[n]$, such that $\mathbf{u}_{t,1}[n] = \mathbf{H}_1[n] * \left\{ \mathbf{U}_{1,\perp}^H[-n] \right\}^T * \mathbf{y}_t[n] = \mathbf{0}$, since $\left\{ \mathbf{H}_1(z) (\mathbf{U}_{1,\perp}^P(z))^T \right\}^T = \mathbf{U}_{1,\perp}^P(z) \mathbf{G}_1(z) = \mathbf{0}$, regardless of the choice of $\mathbf{y}_t[n] \in \mathbb{C}^{M-L_1}$, thus satisfying (4.9).

4.4.2 Maximizing Power Transfer

To address the remaining optimization problem described in (4.8) and (4.10), we will design a second preprocessor $\Psi_2(z)$ to work with the null processor of the first stage $\Psi_1(z)$ from (4.18). The goal is to create a transmit signal $\mathbf{x}_t[n]$ such that the power of $\mathbf{x}_t[n] = \mathbf{F}[n] * \mathbf{u}_{t,2}[n]$ is maximized, to maximize the energy delivery to a potentially hostile receiver while adhering to the interference constraints defined by the nullspace of $\mathbf{H}_1(z)$. For the transfer function $\mathbf{F}(z) \bullet\text{-}\circ \mathbf{F}[n]$ with $\mathbf{F}(z) : \mathbb{C} \rightarrow \mathbb{C}^{L_2 \times L_2}$, we have the general system transfer function

$$\mathbf{F}(z) = \mathbf{H}_2(z) \Psi_1(z) \Psi_2(z), \quad (4.19)$$

where $\mathbf{H}_2(z)$ represents the channel transfer function to the receiver (hostile emitter), $\Psi_1(z)$ enforces the projection onto the nullspace of known friendly signals, and the matrix $\Psi_2(z)$ is to be designed to maximize energy transfer through the projected channel.

The structure of the second channel to the desired receiver is assumed to take the form $\mathbf{H}_2(z) = \mathbf{U}_{1,\perp}^P(z) \mathbf{G}_2(z)$. This projects the output of the transmit signal onto the orthogonal complement of the dominant subspace of $\mathbf{U}_{1,\perp}(z)$, to ensure that transmissions avoid interfering with the desired sources.

Substituting (4.18) for $\Psi_1(z) = \{\mathbf{U}_{1,\perp}^P(z)\}^T$ into (4.19) yields

$$\mathbf{F}(z) = \mathbf{H}_2(z) \{\mathbf{U}_{1,\perp}^P(z)\}^T \Psi_2(z) = (\Psi_2^T(z) \mathbf{U}_{1,\perp}^P(z) \mathbf{H}_2^T(z))^T. \quad (4.20)$$

Assuming reciprocity of the channel such that $\mathbf{G}_2(z) = \mathbf{H}_2^T(z)$, the expression simplifies to

$$\mathbf{F}(z) = (\Psi_2^T(z) \mathbf{U}_{1,\perp}^P(z) \mathbf{G}_2(z))^T. \quad (4.21)$$

Substituting the analytic SVD of the projected channel $\mathbf{G}_2(z) = \mathbf{U}_2(z) \Sigma_2(z) \mathbf{V}_2^P(z)$, where $\mathbf{U}_2(z), \mathbf{V}_2(z)$ are analytic, paraunitary matrices and $\Sigma_2(z)$ is diagonal, with

singular values $\sigma_{2,m}(z)$, into (4.21), gives

$$\mathbf{F}(z) = (\boldsymbol{\Psi}_2^T(z) \mathbf{U}_{1,\perp}^P(z) \mathbf{U}_2(z) \boldsymbol{\Sigma}_2(z) \mathbf{V}_2^P(z))^T. \quad (4.22)$$

Partitioning $\mathbf{U}_2(z) = [\mathbf{U}_{2,\parallel}(z), \mathbf{U}_{2,\perp}(z)]$, due to the assumption (3.4), that the dominant subspace of $\mathbf{G}_2(z)$ is within the orthogonal complement of the signal detected by $\boldsymbol{\Psi}_1(z)$, we have a projection

$$(\mathbf{U}_{1,\perp}(z) \mathbf{U}_{1,\perp}^P(z)) \mathbf{U}_{2,\parallel}(z) = \mathbf{U}_{2,\parallel}(z). \quad (4.23)$$

Note that (4.23) is due to the dominant subspace $\mathbf{U}_{2,\parallel}(z)$ of the jammer channel lying within the nullspace of $\mathbf{H}_1(z)$, making the projection onto $\mathbf{U}_{1,\perp}(z)$ redundant. Here, $\mathbf{U}_{2,\parallel}(z)$ represents the signal's parallel component within the signal subspace. Therefore, for this choice,

$$\boldsymbol{\Psi}_2^T(z) = \boldsymbol{\Pi}(z) \mathbf{U}_{2,\parallel}^P(z) \mathbf{U}_{1,\perp}(z) \quad (4.24)$$

as preprocessor, we obtain

$$\mathbf{F}(z) = (\boldsymbol{\Pi}(z) \boldsymbol{\Sigma}_2(z) \mathbf{V}_2^P(z))^T, \quad (4.25)$$

where the diagonal matrix $\boldsymbol{\Pi}(z) = \text{diag}\{\pi_1(z), \dots, \pi_{L_2}(z)\}$ denotes a diagonal power allocation matrix to optimize. This formulation separates the channel modes, enabling tractable power allocation optimization.

Based on (4.16) from Sec. 4.3, we can determine the power of $\mathbf{u}_{t,2}[n]$ based on the eigenvalues of $\mathbf{F}(z)$ in (4.25). Thus, the transmit power is now given by $\boldsymbol{\Pi}(z)$, and the receive power is given by both $\boldsymbol{\Pi}(z)$ and $\boldsymbol{\Sigma}_2(z)$. This simplifies the remaining optimization problem of (4.8) and (4.10) to

$$\max_{\pi_m} \sum_{m=1, \dots, L_2} \sum_{m,n} |\pi_m[n] * \sigma_{2,m}[n]|^2 \quad \text{s.t.} \quad \sum_{m,n} |\pi_m[n]|^2 = P_0. \quad (4.26)$$

Thus, the transmit power for each mode is specified by $\pi_m(z)$, and the corresponding

received power is proportional to $|\pi_m[n] * \sigma_{2,m}[n]|^2$, where $*$ denotes convolution in time.

The total power is maximized under a transmit power constraint P_0 . This ideally involves spectral temporal shaping of the transmit signal, akin to water filling for power allocation in the narrowband case [225]. Thus, the terms $\pi_m(z)$ allocate power to the spatial and spectral components with the highest gains in the singular value $\sigma_m(z)$. The time-domain version are $\sigma_{2,m}[n]$ for the m -th singular value m -th in $\Sigma_2(z)$ and $\pi_m[n]$ for the power allocation function in mode m . Assuming a known channel $\mathbf{G}_2(z)$, $\Sigma_2(z) = \mathbf{I}$ is used for simplicity and tractability of a solution, since the optimal uniform power allocation now leads to $\mathbf{\Pi}(z) = \frac{P_0}{L_2} \mathbf{I}$ satisfying the power constraint in (4.10), the overall solution to the preprocess in (4.27) is given by

$$\Psi_1(z)\Psi_2(z) = \frac{P_0}{L_2} \left\{ \mathbf{U}_{2,\parallel}^{\text{P}}(z) \mathbf{U}_{1,\perp}(z) \mathbf{U}_{1,\perp}^{\text{P}}(z) \right\}^{\text{T}} \quad (4.27)$$

$$= \frac{P_0}{L_2} \left\{ \mathbf{U}_{2,\parallel}^{\text{P}}(z) \right\}^{\text{T}} . \quad (4.28)$$

for the preprocessor matrix to a zero mean, unit variance, uncorrelated signal $\mathbf{y}_t[n] \in \mathcal{CN}(0, \mathbf{I})$ of dimension L_2 . The step from (4.27) to (4.28) takes advantage of the assumption in (4.4).

4.5 Power Transfer Based on Time Reversal

4.5.1 Time Reversal Approach

If the channels $\mathbf{G}_2(z)$ and consequently $\mathbf{H}_2(z) = \mathbf{G}_2^{\text{T}}(z)$ are unknown, we explore time reversal processing as a technique to transfer energy to the sources represented by $\mathbf{u}_{t,2}[n]$. For the received signal as shown in Fig. 4.1, we operate with the receive processor matrix $\mathbf{\Phi}(z)$ in (4.2), such that

$$\mathbf{y}_r[n] = \mathbf{\Phi}[n] * (\mathbf{G}_2[n] * \mathbf{u}_{r,2}[n] + \mathbf{v}[n]) . \quad (4.29)$$

Thus, the received signal $\mathbf{y}_r[n]$ consists of the desired (hostile) signal $\mathbf{G}_2[n] * \mathbf{u}_{r,2}[n]$ and noise $\mathbf{v}[n]$. The processor matrix $\Phi[n]$ extracts the desired signal from this combined data.

The transmitted signal is the time-reversed complex conjugate of the received signal, processed through $\Psi_1[n]$ in (4.18), such that

$$\mathbf{x}_t[n] = \rho \Psi_1[n] * \mathbf{y}_t[n] = \rho \Psi_1[n] * \{\mathbf{y}_r[-n]\}^* . \quad (4.30)$$

This represents the signal transmission process, where $\mathbf{y}_r[n]$ is time-reversed, conjugated, and processed, resulting in $\mathbf{x}_t[n]$. The potential time delay for causality is omitted for simplicity, and the gain factor ρ is adjusted to satisfy the power constraint (4.10). Note that for the processor matrix $\Psi(z) = \Psi_1(z)\Psi_2(z)$, we operate with $\Psi_1(z)$ to protect friendly sources from interference by nullsteering as outlined in Sec. 4.4.1, while compared to Sec. 4.4, we set $\Psi_2(z) = \rho \mathbf{I}$, since $\mathbf{G}_2(z)$ is now unknown.

The received signal in Fig. 4.2 is

$$\mathbf{u}_{t,2}[n] = \mathbf{H}_2[n] * \mathbf{x}_t[n] . \quad (4.31)$$

To evaluate power transfer, Sec. 4.5.2 will characterize the transmit power of $\mathbf{x}_t[n]$ in (4.30) and adjust ρ , while Sec. 4.5.3 will assess the jamming power of $\mathbf{u}_{t,2}[n]$ in (4.31).

4.5.2 Transmit Power

In order to determine the transmit power $\mathcal{E} \{\mathbf{x}_t^H[n]\mathbf{x}_t[n]\}$, inserting (4.29) into (4.30) produces

$$\mathbf{x}_t[n] = \rho \Psi_1[n] * \Phi^*[-n] * (\mathbf{G}_2^*[-n] * \mathbf{u}_{r,2}^*[-n] + \mathbf{v}^*[-n]) \quad (4.32)$$

$$= \mathbf{A}_1^T[n] * \mathbf{u}_{r,2}^*[-n] + \mathbf{A}_2^T[n] * \mathbf{v}^*[-n] . \quad (4.33)$$

In (4.32), the expression $\Phi^*[-n]$ represents the filtering operation on the received signal, involving time-reversal and complex conjugation. Specifically, $\mathbf{G}_2^*[-n]$, $\mathbf{u}_{r,2}^*[-n]$, and

$\mathbf{v}^*[-n]$ denote the complex conjugates of the channel matrix, the transient source signal, and the observation noise, respectively. The expression (4.32) is simplified in (4.33) by defining transfer matrices $\mathbf{A}_1^T[n] = \rho \Psi_1[n] * \Phi^*[-n] * \mathbf{G}_2^*[-n]$ and $\mathbf{A}_2^T[n] = \rho \Psi_1[n] * \Phi^*[-n]$ for contributions attributable to the transient source and noise. These now each form an innovation model excited by zero-mean unit-variance spatially and temporally uncorrelated signals akin to that depicted in Fig. 4.3.

For $\mathbf{A}_i(z) \bullet \circ \mathbf{A}_i[n], i = 1, 2$, substituting (4.2) and (4.18), we have

$$\mathbf{A}_1(z) = \rho \mathbf{G}_2^P(z) \mathbf{U}_{1,\perp}(z) \mathbf{U}_{1,\perp}^P(z) = \rho \mathbf{G}_2^P(z) \quad (4.34)$$

$$\mathbf{A}_2(z) = \rho \mathbf{U}_{1,\perp}(z) \mathbf{U}_{1,\perp}^P(z) \quad (4.35)$$

Applying assumption (4.4) to (4.34) simplifies $\mathbf{A}_1(z)$ since $\mathbf{G}_2^P(z)$ lies in the nullspace of $\mathbf{G}_1(z)$ such that the projection matrix $\mathbf{U}_{1,\perp}(z) \mathbf{U}_{1,\perp}^P(z)$ is without consequence, leading to the simplified form $\mathbf{A}_1(z) = \rho \mathbf{G}_2^P(z)$.

Considering the excitation signals in (4.33) to be complex Gaussian symmetry and uncorrelated, the statistics of $\mathbf{u}_{r,2}^*[-n]$ and $\mathbf{v}^*[-n]$ mirror those of $\mathbf{u}_{r,2}[n]$ and $\mathbf{v}[n]$. Consequently, we computed the transmit power based on the innovation model approach in Sec. 4.3 using the analytic SVD of $\mathbf{G}_2(z)$ and used Sec. 4.5.1. The transmit power component due to $\mathbf{A}_1(z)$ is therefore according to (4.34) based on the analytic SVD of $\mathbf{G}_2(z)$. For the noise contribution to the transmit power due to $\mathbf{A}_2(z)$, note that $\mathbf{U}_{1,\perp}(z) \mathbf{U}_{1,\perp}^P(z)$ serves as a projection matrix onto a subspace of dimension $(M - L_1)$ for (4.35). This leads to

$$\mathcal{E}\{\mathbf{x}_t^H[n] \mathbf{x}_t[n]\} = \rho^2 \left\{ \sum_{m,n} |\sigma_{2,m}[n]|^2 + (M - L_1) \sigma_v^2 \right\} \quad (4.36)$$

for the transmit power, where $\sigma_{2,m}(z) \bullet \circ \sigma_{2,m}[n]$ are the singular values of $\mathbf{G}_2(z)$, and σ_v^2 is the observation noise power. Finally, the gain ρ in (4.30) must therefore be set to

$$\rho = \sqrt{P_0} \left(\sum_{m,n} |\sigma_{2,m}[n]|^2 + (M - L_1) \sigma_v^2 \right)^{-\frac{1}{2}} \quad (4.37)$$

in order to satisfy the transmit power constraint (4.10) of our optimization problem.

4.5.3 Received Power of Jamming Signal

For the signal $\mathbf{u}_{t,2}[n]$ received at the sources to be jammed, (4.31) expands with (4.33) to

$$\mathbf{u}_{t,2}[n] = \mathbf{H}_2[n] * (\mathbf{A}_1^T[n] * \mathbf{u}_{r,2}^*[-n] + \mathbf{A}_2^T[n] * \mathbf{v}^*[-n]) . \quad (4.38)$$

This describes the jamming signal received at the source location after the time-reversed signal has been transmitted and propagated back through the channel $\mathbf{H}_2[n]$. This can be simplified as

$$\mathbf{u}_{t,2}[n] = \mathbf{B}_1^T[n] * \mathbf{u}_{r,2}^*[-n] + \mathbf{B}_2^T[n] * \mathbf{v}^*[-n] \quad (4.39)$$

where $\mathbf{B}_1[n]$ corresponds to the signal path from the original transient source emission to the reception of the jamming signal, while $\mathbf{B}_2[n]$ is the transfer path for the observation noise. For $\mathbf{B}_i(z) \bullet \circ \mathbf{B}_i[n], i = 1, 2$, we find that with (4.34)

$$\mathbf{B}_1(z) = \rho \mathbf{G}_2^P(z) \mathbf{G}_2(z) \quad (4.40)$$

$$\mathbf{B}_2(z) = \rho \mathbf{U}_{1,\perp}(z) \mathbf{U}_{1,\perp}^P(z) \mathbf{G}_2(z) = \rho \mathbf{G}_2(z) , \quad (4.41)$$

where assumption (4.4) results in the projection of $\mathbf{G}_2(z)$ onto itself in (4.41). Note that this assumption idealistically implies that $\mathbf{G}_2(z)$ lies in the nullspace of $\mathbf{G}_1(z)$, which now has lead to tractable even so perhaps not most realistic result. In practice, part of $\mathbf{G}_2(z)$ may not lie entirely in the subspace of $\mathbf{G}_1(z)$, such that not all of the energy of the transient signal can be detected, and that the power transfer to the transient source as a result may be suboptimal.

Since $\mathbf{B}_i(z), i = 1, 2$ describes innovation models in the sense of Sec. 4.3, for the

power received in $\mathbf{u}_{t,2}[n]$, we obtain

$$\mathcal{E} \{ \mathbf{u}_{t,2}^H[n] \mathbf{u}_{t,2}[n] \} = \rho^2 \sum_{m,n} |\sigma_{m,2}[n] * \sigma_{m,2}^*[-n]|^2 + \rho^2 \sigma_v^2 \sum_{m,n} |\sigma_{m,2}[n]|^2 \quad (4.42)$$

with the allocated transmit gain ρ given in (4.37) in order to satisfy the transmit power constraint.

4.6 Results

4.6.1 Parameters and Metrics

The SNR γ_r of $\mathbf{y}_r[n]$ consists of the two terms on the right side of (4.29), which is also equivalent to the transmit power terms in (4.36) when $\rho = 1$. Therefore, we have

$$\gamma_r = \frac{\sum_{m,n} |\sigma_{2,m}[n]|^2}{(M - L_1) \sigma_v^2}. \quad (4.43)$$

This SNR highlights the challenge of identifying a change point associated with the transient signal $\mathbf{u}_{r,2}[n]$, as mentioned in Sec. 4.2.1.

The presence of noise with $\sigma_v^2 > 0$ also poses a challenge for the time-reversal approach, as not all transmit power may be directed toward the source. This occurs either because we transmit in an L_1 -dimensional subspace that exceeds the dimension of the target $\mathbf{u}_{t,2}[n]$, or because of the spatiotemporal structure of the time reversal signal related to the noise, which is neither spectrally shaped nor coherently aligned in order to contribute significantly to $\mathbf{u}_{t,2}[n]$. To assess the jamming efficiency,

$$\gamma_t = \frac{1}{P_0} \mathcal{E} \{ \mathbf{u}_{t,2}^H[n] \mathbf{u}_{t,2}[n] \} \quad (4.44)$$

measures the ratio of the jammer power indicated in (4.38) to the afforded transmit power P_0 .

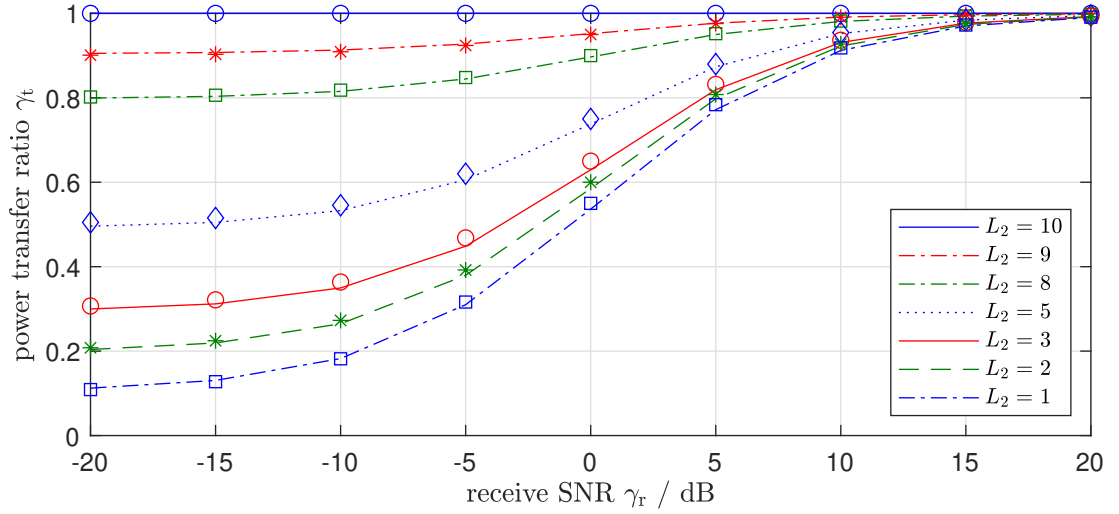


Figure 4.4: Power transfer γ_t vs. receive SNR γ_r for various dimensions L_2 of $\mathbf{u}_{t,2}[n]$ for $\Sigma_2(z) = \mathbf{I}$; lines indicate experimental values and markers represent theoretical values.

4.6.2 Simulations

For simulations with $M = 20$ sensors, $L_1 = 10$ stationary sources, and potentially $L_2 = 1 \dots, (M - L_1)$ transient sources to be jammed, the matrices $\mathbf{G}_i(z)$, for $i = 1, 2$, are constructed from known analytic SVD factors. Paraunitary matrices of order 5 are created from elementary paraunitary operations [108], with $U_{i,\parallel}(z)$, $i = 1, 2$, extracted from different columns of the same paraunitary matrix to satisfy (4.4). Simulations are carried out on 1000 samples, and experimental values for power transfer based on finite data [195, 197, 198] are compared to theoretical metrics when $\mathbf{G}_2(z)$ is known in (4.26), and for time reversal based on (4.42). The parameter values, particularly for M and L_i , $i = 1, 2$, have been chosen to be sufficiently large to justify the 'multiple' in 'MIMO', but still allow to simulate an ensemble with sufficient computational ease to reveal the effects that these parameters have on the simulation results.

In the first case, we set $\sigma_{2,m} = 1, m = 1, \dots, L_2$. Thus, if $\mathbf{H}_2(z)$ is known, the approach outlined in Sec. 4.4 can solve the optimisation problem (4.8) to (4.10) with a power allocation of $\mathbf{\Pi}(z) = \mathbf{I}$. In this scenario, the power transfer is constant at $\gamma = 1$, regardless of the received SNR, as the jamming signal depends only on $\mathbf{G}_2(z)$. The

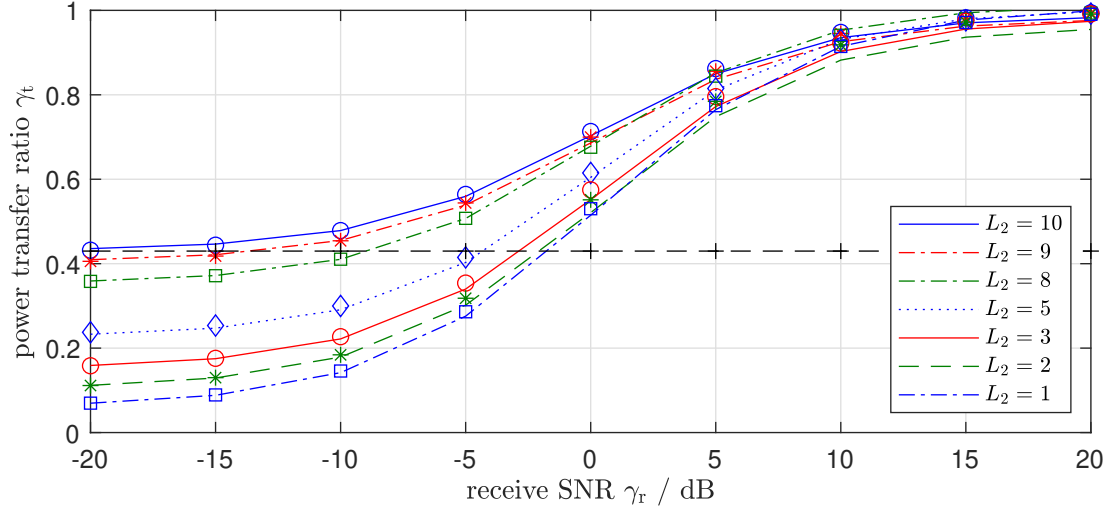


Figure 4.5: Parameters as in Fig. 4.4, but for a randomized $\Sigma_2(z)$ of order 3. The black horizontal line indicates the method of Sec. 4.4 with a suboptimal $\mathbf{\Pi}(z) = \mathbf{I}$.

theoretical and experimental values for the time reversal are shown in Fig. 4.4. The source signal dominates the time-reversed data for a high receive SNR γ_r , leading to $\gamma_t \rightarrow 1$. For a low receive SNR γ_r , noise takes precedence; however, since the noise occupies an $(M - L_1)$ -dimensional subspace and $\sigma_{2,m} = 1$, we find that $\gamma_t \rightarrow \frac{L_2}{M-L_1}$.

In a second case, we build the transfer matrices based on non-trivial singular values $\sigma_{2,m}(z) = a_m(z) + a_m^P(z)$ with a random system $a_m(z)$ of order 2, normalized such that $\left(\sum_n \|\Sigma_2[n] * \Sigma_2[n]\|_F^2 \right) / \left(\sum_n \|\Sigma_2[n]\|_F^2 \right) = 1$. This normalization ensures that the time reversal method for $\sigma_v^2 = 0$ yields a power transfer ratio $\gamma_t = 1$. For varying levels of SNR, the resulting power transfer γ_t is shown in Fig. 4.5. Here, as the receive SNR γ_r decreases, the power transfer ratio degrades more significantly compared to Fig. 4.4, since the noise in the time-reversed signal does not retain the correct spatio-temporal structure necessary to connect with the sources associated with $\mathbf{u}_{t,2}[n]$. If the channel $\mathbf{H}_2(z)$ is known and we utilize suboptimal power allocation $\mathbf{\Pi}(z) = \mathbf{I}$ as described in Sec. 4.4, the design is independent of noise $\mathbf{v}[n]$ in Fig. 4.1 and therefore independent of the receive SNR γ_r . For $L_2 = 10$, its constant level signifies the value to which the time reversal method approaches as the SNR decreases; this differs from Fig. 4.4, where $\mathbf{\Pi}(z) = \mathbf{I}$ was identical, and here the asymptote is approached from above.

4.7 Chapter Summary

Our objective was to disrupt hostile broadband sources, once their emissions were detected, while ensuring that other users remained interference-free. We developed a time-reversal scheme to create targeted interference and analysed it using the analytic SVD of the broadband channel matrices. The developed scheme does not rely on knowledge of the channel between the hostile user and the array, and performs well under moderate SNR conditions for the time-reversed signal, but deteriorates at higher noise levels. Compared to a scenario in which the channel to the hostile sources was known, a broadband beamforming approach extended from the narrowband case served as the upper performance limit for the time-reversal method in a simplified channel environment. The comparison to beamforming also clarified the specific performance characteristics of the time-reversal approach in more complex transmission channels.

Analytic techniques that provide broadband decomposition and rigorous noise handling improve PSD estimation by separating meaningful components from high dimensional noise. These methods impose structure on otherwise unstructured data. The challenges faced by time-reversal methods in noisy environments parallel those of low-rank PSD estimation as the source density increases. The next chapter will address optimized lag selection, rank-one and low-rank denoising strategies, and source-enumeration limits, which are central to improving environmental awareness and connecting interference control with precise signal interpretation.

As simulation results in Sec. 4.6 have shown, the additive noise in the reception stage of the time-reversal technique has a profound effect on the viability of the proposed approach — note that all results critically depend on the receive SNR. It is therefore best to deploy the time-reversal technique when the receive SNR is high. Since the statistics of the background noise may potentially change with time, e.g. due to mobility, atmospheric effects, etc, it may therefore be opportune to exploit ‘windows of opportunity’ when the noise power is low — either overall, or perhaps only in certain parts of the spectrum. For this reason, Chapter 5 will explore the estimation of power spectra density across an array under slowly time-varying conditions.

Chapter 5

Monitoring Time-Varying Noise Power Spectral Density and Identifying Windows of Opportunity

5.1 Introduction

5.1.1 Preliminaries

Chapter 3 has addressed the challenge of weak transient signal detection, e.g., of PUs. As established, the detection performance is, amongst other factors, dependent on the SNR between the weak signal and the background noise in the syndrome vector. In case this SNR fluctuates, an arising question is if we may be able to detect opportune moments when SNR is high in order to aid detection.

Chapter 4 has introduced jamming of an undesired source, which has previously been detected, for example, for the purpose of policing the spectrum in order to protect PUs. The proposed time-reversal method requires transmitting a previously acquired signal, and the power transfer, i.e., the effectiveness of directing energy towards the

undesired source, has been shown to depend again on the receive SNR. Hence, if SNR fluctuates and noting that a signal received at a higher SNR results in an improved power transfer, we are interested in establishing moments in time (and potentially frequency) when it is good to record a received signal for use in time-reversal processing.

Thus, in order to potentially extend the utility of the methods discussed in Chapters 3 and 4, this chapter explores the possibility of monitoring noise power, and thus SNR, in the case of a rank-one noise source. We assume that a number of sensors are available, and that we want to know the noise power or, since this thesis is generally concerned with broadband systems, the noise power spectral density in case these quantities fluctuate over time and frequency. This can then help to identify windows and frequency bands of opportunity where noise power or noise power spectral density is low [48].

5.1.2 Background and Overview

If noise statistics — particularly noise power — change over time, windows of opportunity may arise when it becomes possible to observe potentially weaker signals in the environment. In the image processing domain, this phenomenon is called 'lucky imaging' [226]. In underwater broadband scenarios, where signals may span several octaves in frequency, these windows of opportunity may be limited to specific frequency bands over time. In the context of CR, which is investigated in this thesis, we are interested in detecting the emergence of a weak PU signal.

Typically, such fluctuating noise characteristics can be assigned to time variations in the channel through which the noise illuminates the sensors [227, 228]. In the underwater domain, this time-varying effect is also referred to as a loss of coherence [229–232], which is exacerbated by the generally larger aperture when processing in subarrays [233, 234]. These fluctuations must be taken into account during processing, including maximum likelihood [235, 236], direction of arrival estimation [231, 235, 237], or time-reversal [47, 238] and matched field processing [5, 44, 46, 131, 239, 240]

To reduce estimation errors from multiple sensors receiving a noise source, we pro-

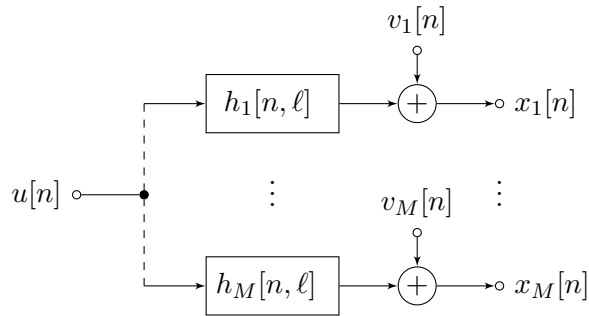
pose a space-time covariance estimation approach. This involves optimizing the lag support, as described in [196, 197] and applying a rank-one approximation of the space-time covariance for denoising, similar to rank-constrained estimation for spatial-only correlation presented in [241, 242].

This chapter introduces the system model and parsimonious channel models, focusing on the basis expansion model (BEM) for time-varying channels in Sec. 5.2. Sec. 5.3 derives the cross-spectral density matrix and applies Welch’s periodogram method for the estimation of power spectral density (PSD) from N data snapshots. Classical Welch treats each frequency bin independently and does not exploit structural properties of time-varying channels. In contrast, the proposed method introduces lag optimization to minimize estimation bias under finite observations and enforces a rank-one constraint motivated by dominant Doppler eigenmodes. This reduces estimation variance and stabilizes the CSD matrix, which directly improves BEM basis extraction. In Sec. 5.4, the space-time covariance matrix is discussed, noting its higher computational cost and potential performance benefits. Sec. 5.5 optimizes the lag support of the space-time covariance estimate to reduce the deviation from the true covariance $\mathbf{R}[\tau]$. Performance comparisons with the Welch method are presented in Sec. 5.6, followed by a chapter summary in Sec. 5.7.

5.2 Signal Model

5.2.1 Innovation Filter Model

We assume that a sensor array observing a single non-stationary source is composed of M sensors, each recording a time series $x_m[n]$, $m = 1, \dots, M$. The model is illustrated in Fig. 5.1, where the source is represented as a Gaussian process with zero mean unit variance $u[n]$, and non-stationary statistics are imposed by time-varying innovation filters [112]. In general, we also assume that each channel exhibits different non-stationary behavior, such as fluctuations in the propagation environment, which may occur, for instance, in underwater acoustics. Thus, each channel is governed by its innovation filters

Figure 5.1: Model for M measurements observing a single non-stationary source.

$h_m[n, \ell]$, where ℓ is the coefficient index, and n represents the time dependency of the innovation filter. Each measurement $x_m[n]$ is expected to represent a Gauss-Markov process [243], which captures the channel temporal variation through symbol-by-symbol updating; corrupted by additive observation noise $v_m[n]$, which is spatially and temporally uncorrelated with variance σ_v^2 such that $\mathcal{E}\{v_m[n]v_\mu^*[n-\tau]\} = \sigma_v^2\delta[m-\mu]\delta[\tau]$, with $\mathcal{E}\{\cdot\}$ being the expectation operator and $\delta[n]$ the Kronecker delta function.

5.2.2 Basis Expansion Model

In order to model the time-varying filters $h_m[n, \ell]$ in Fig. 5.1, we will rely on a BEM, which is a common technique to model time-varying channels within the communication community, or to estimate time-varying channels by fitting a BEM [244]. A BEM can approximate channels over a range of time variations, including effectively modelling and estimating fast-varying channels [245]. The variability of the channel can be effectively yet accurately modelled using BEM, via a superposition of basis waveforms modulated by suitable functions such as complex exponentials. Typically, a model with internal paths $Q = 10$ (to be explicitly defined further below) is considered sufficient to capture most channels that are estimated in practice [246]. Most BEMs are used in combination with complex exponential as modulation sequences.

Various BEM methods have been explored in the literature. The authors in [246] proposed complex exponential basis functions (CE-BEM), which significantly reduce the computational complexity of channel estimation. Improvements in CE-BEM for

enhanced tracking accuracy have been introduced in [247]. In [248], a notable advancement over CE-BEM was achieved by uniformly distributing complex exponentials to the normalized Doppler frequency in the double selective channel. Furthermore, [249] introduced fixed CE-BEM, which offers similar tracking performance without prior knowledge of the Doppler frequency, but experiences performance degradation in high-mobility situations. In [250], discrete prolate spheroidal (DPS) sequences are used in DPS-BEM, which provides good tracking for band-limited Doppler spread but requires significant computational resources. The discrete Karhunen-Loève BEM (DKL-BEM) is designed to track time variations in the bath-tube-shaped Doppler spectrum [251]. The Karhunen-Loève decomposition BEM in [252] is based on channel statistics. Polynomial BEM (P-BEM) utilizes polynomials for channel time variation but is affected by Doppler frequency, with the channel approximation becoming more accurate as the polynomial order increases [253].

In the following, we will utilize a simple complex exponential BEM as an innovation filter to implement a Gauss-Markov process. Motivated by signal processing, communications, propagation and information theory communities, where there may be Q different transmit paths with varying Doppler shifts (i.e., paths are assumed to shorten or lengthen with time), we express the BEM of $h_m[n, \ell]$ as

$$h_m[n, \ell] = \sum_{q=1}^Q b_{m,q}[n] h_{m,q}[\ell], \quad (5.1)$$

which reduces the time variation to time-varying basis functions for $b_{m,q}[n]$, $q = 1, \dots, Q$ which modulate a set of Q time-invariant filters $h_{m,q}[\ell]$. We consider a complex exponential $b_{m,q}[n] = e^{j\Omega_{m,q}n}$, which is a very commonly selected basis function (CE-BEM) [244, 246, 254]. CE-BEM offers several practical advantages, enabling the rapid generation of basis vectors independent of channel statistics while ensuring orthogonality. The modulation frequencies $\Omega_{q,m}$ are not harmonically related and are typically drawn from a random distribution; we choose a uniform distribution such that $|\Omega_{m,q}| \leq \Omega_{\max}$.

The BEM effectively models multipath propagation and communication over time-varying channels, characterizing them as doubly-dispersive systems. With respect to (w.r.t). temporal dispersion, multiple paths with a delay spread greater than a symbol duration result in broadband propagation, with the channel's impulse response thus extending beyond one symbol period. However, a Doppler shift is a narrowband phenomenon that in a broadband setting should be described as a scaling (i.e., a compression or expansion of a signal). Using several, i.e. Q , paths with different Doppler shifts, results in Doppler spread, which can accurately model a variety of complex channel scenarios, especially for $Q > 10$ [246].

5.3 Expected Noise Power Spectral Density

5.3.1 Space-Time Covariance and Cross Spectral Density Matrices

We focus on the space-time covariance matrix [107–109] for broadband signals, defined as $\mathbf{R}[\tau, n] = \mathcal{E} \{ \mathbf{x}[n] \mathbf{x}^H[n - \tau] \}$, where $\mathbf{x}[n] = [x_1[n], \dots, x_M[n]]^T \in \mathbb{C}^M$ represents the measurement vector of the M sensors in the discrete time index n . We must consider explicit delays because phase shifts, as captured by ordinary covariance matrices, do not retain accurate spatial information for broadband sources. Second-order statistics are captured by the space-time covariance matrix $\mathbf{R}[\tau] = \mathcal{E} \{ \mathbf{x}[n] \mathbf{x}^H[n - \tau] \} \in \mathbb{C}^{M \times M}$, with the discrete lag parameter $\tau \in \mathbb{Z}$ containing the required delay, with $\mathcal{E} \{ \cdot \}$ indicating the expectation operator, and $\{ \cdot \}^H$ denoting the Hermitian transposition [120]. The entries of this matrix require the estimation of general cross-correlation sequences $r_{m\mu}[\tau, n] = \mathcal{E} \{ x_m[n] x_\mu^*[n - \tau] \}$, which reflects the correlation between the signal at sensor m at time n and the signal at sensor μ at a delayed time $n - \tau$. Such a cross-correlation sequence can be connected to time-varying filters in the innovation model of Fig. 5.1 as

$$r_{m\mu}[\tau, n] = \sum h_m[n, \ell] h_\mu^*[n - \tau, \ell - \tau]. \quad (5.2)$$

Inserting the BEM model of (5.1) yields

$$r_{m\mu}[\tau, n] = \sum_{\ell} \left(\sum_{p=1}^Q e^{j\Omega_{m,p}n} h_{m,p}[\ell] \right) \left(\sum_{q=1}^Q e^{-j\Omega_{\mu,q}(n-\tau)} h_{\mu,q}^*[\ell - \tau] \right) \quad (5.3)$$

$$= \sum_{p,q=1}^Q e^{j(\Omega_{m,p}-\Omega_{\mu,q})n} e^{j\Omega_{\mu,q}\tau} (h_{m,p}[\tau] * h_{\mu,q}^*[-\tau]) . \quad (5.4)$$

The formulation in (5.4) now includes the cross-correlations between all possible pairs of the Q paths in the sensor channels, modulated by differences in Doppler shifts w.r.t. the time index n , and modulated by the Doppler shifts in the μ th sensor paths w.r.t. the lag parameter τ .

The time-varying CSD matrix is defined as $\mathbf{R}(e^{j\Omega}, n) = \sum_{\tau} \mathbf{R}[\tau, n] e^{-j\Omega\tau}$, with $H_{m,n}(e^{j\Omega}) \bullet \circ h_{m,p}[n] e^{-j\Omega n}$. Its entry in the m th row and μ th column can be obtained from transforming (5.4),

$$R_{m\mu}(e^{j\Omega}, n) = \sum_{p,q=1}^Q e^{j(\Omega_{m,p}-\Omega_{\mu,q})n} H_{m,p}(e^{j(\Omega-\Omega_{\mu,q})}) H_{\mu,q}^*(e^{j(\Omega-\Omega_{\mu,q})}) , \quad (5.5)$$

whereby $e^{j(\Omega_{m,p}-\Omega_{\mu,q})n}$ from (5.4) remains as a time-varying term, and $e^{j\Omega_{\mu,q}\tau}$ in (5.4) causes a frequency shift of the time-invariant path filters $H_{\mu,q}(e^{j\Omega}) \bullet \circ h_{\mu,q}[\ell]$ within the BEM in (5.1). Thus, (5.5) illustrates how Doppler effects and channel dynamics induce modulations and frequency shifts, thus causing variations in both time and frequency as expected from a doubly-dispersive channel.

5.3.2 Power Spectral Density

The CSD, defined by its element in (5.5), includes the PSD terms along its diagonal. Therefore, when $m = \mu$, we can derive the PSD $R_{mm}(e^{j\Omega}, n)$ of the signal $x_m[n]$ on the m th sensor as

$$R_{mm}(e^{j\Omega}, n) = \sum_{p,q=1}^Q e^{j(\Omega_{m,p}-\Omega_{m,q})n} H_{m,p}(e^{j(\Omega-\Omega_{m,q})}) H_{m,q}^*(e^{j(\Omega-\Omega_{m,q})}) , \quad (5.6)$$

which through the modulation terms $e^{j(\Omega_{m,p}-\Omega_{m,q})n}$ is also time-dependent. Thus, the expression (5.6) represents the power distribution over frequency for the sensor m at time n , incorporating the non-stationary structure of the BEM.

Example 10 *In order to illustrate the theoretical result discussed above, and highlight the time- and frequency-variations imposed by the BEM, we consider an example with $Q = 10$, with filters $h_{1,q}[n]$ having length $L = 5$ and the coefficients are drawn from a complex Gaussian distribution with zero mean and unit variance. The frequency components $\Omega_{1,q}$ are sampled from a uniform distribution on the interval $[-\Omega_{\max}, \Omega_{\max}]$, with $\Omega_{\max} = 10^{-4}$. Fig. 5.2 shows the power spectral density $R_{11}(e^{j\Omega}, n)$ as a function of the time index n and the normalized angular frequency Ω .*

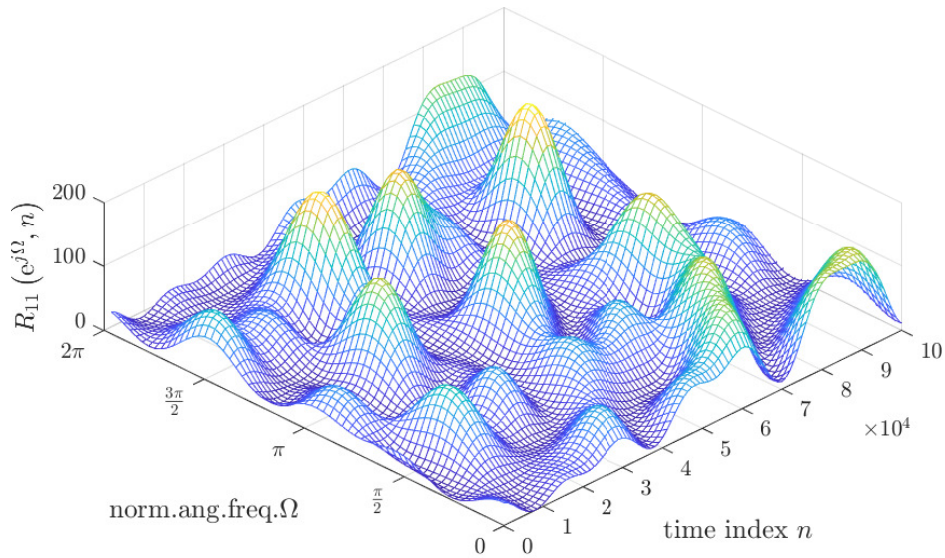


Figure 5.2: Time-varying PSD of Example 10 generated by a BEM.

Note that while the resulting PSD of Example 10 in Fig. 5.2 is random, its variability with time and frequency can be influenced by the BEM parameters. A higher value for Ω_{\max} will result in faster time evolution. At the same time, longer filters $h_{\mu,q}[n]$, i.e., higher values of L , can cause a more frequency-selective behaviour, resulting in faster frequency variation Ω .

5.4 Estimated Noise Power Spectral Density

The expected PSD in (5.6) is now to be estimated from a finite number of N data snapshots. We briefly review the periodogram method by Welch [4] as the state-of-the-art in Sec. 5.4.1, and also discuss a space-time covariance matrix estimation approach in Sec. 5.4.2.

5.4.1 Spectral Estimation

For a spectral resolution of K frequency bins, the well-known Welch method [4] averages the squared modulus of Fourier coefficients obtained from shorter segments of length K , into which the longer data sequence of length N is subdivided. To reduce a lag error in estimating the time-varying statistics, we calculate an estimate $\hat{R}_{\text{Welch},mm}(\mathrm{e}^{\mathrm{j}\Omega_k}, n)$, $\Omega_k = 2\pi k/K$ with $k = 0, \dots, (K-1)$, over a window of data on the interval $[n - \frac{N}{2}; n + \frac{N}{2})$, with N even, when comparing it to the expected PSD $R_{mm}(\mathrm{e}^{\mathrm{j}\Omega}, n)$. We use a rectangular window because we do not expect periodic components in $x_m[n]$ that could otherwise cause severe spectral leakage, and we avoid overlap between data segments to prevent potential redundancy and data incest. Consequently, the $\lfloor N/K \rfloor$ segments are used to average the result bin-wise, where $\lfloor \cdot \rfloor$ denotes the floor operator.

Example 11 For the scenario in Example 10, we calculate the power spectral density estimates $\hat{R}_{\text{Welch},mm}(\mathrm{e}^{\mathrm{j}\Omega_k}, n)$ with $K = 32$ frequency bins, using a sample size of $N = 2^{10}$. The averaging is performed across the $N/K = 32$ segments. The result is shown in Fig. 5.3.

In order to measure the least-squares mismatch between the spectral estimate $\hat{R}_{\text{Welch},mm}(\mathrm{e}^{\mathrm{j}\Omega_k}, n)$ and the expected PSD $R_{mm}(\mathrm{e}^{\mathrm{j}\Omega}, n)$ based on the BEM, we define a normalised error,

$$e_{\text{Welch}}[n] = \sum_{m=1}^M \frac{\sum_{k=0}^{K-1} |R_{mm}(\mathrm{e}^{\mathrm{j}\Omega_k}, n) - \hat{R}_{\text{Welch},mm}(\mathrm{e}^{\mathrm{j}\Omega_k}, n)|^2}{\sum_{k=0}^{K-1} |R_{mm}(\mathrm{e}^{\mathrm{j}\Omega_k}, n)|^2}. \quad (5.7)$$

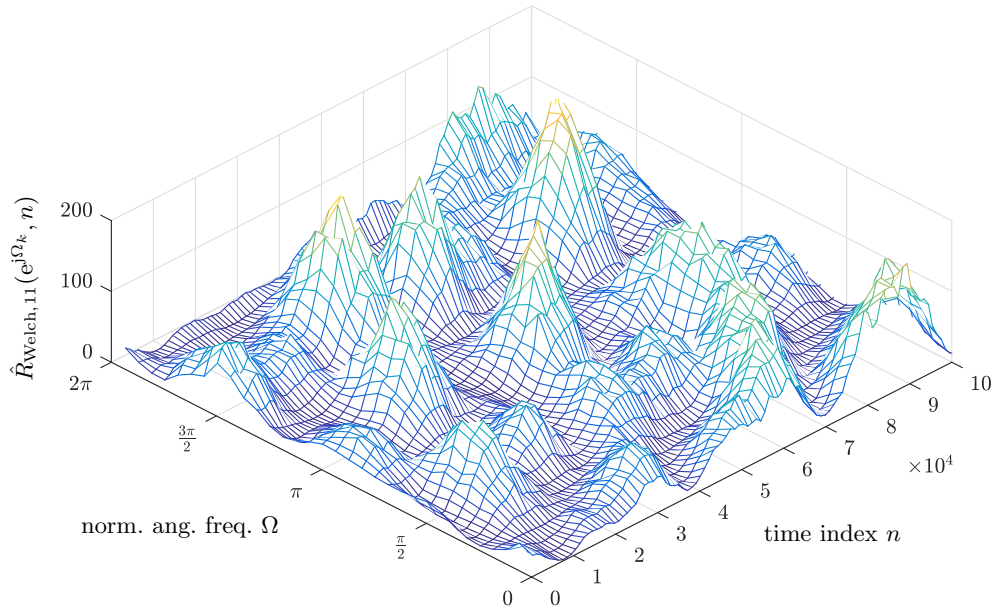


Figure 5.3: Example 11 for time-varying PSD using the Welch method [4], estimating the PSD of Example 10 in Fig. 5.2.

This error captures the spectral mismatch at time n in all sensors and across all frequency bins Ω_k for which the Welch estimate is calculated, with $R_{mm}(e^{j\Omega_k}, n)$ being the expected PSD evaluated in those frequency bins. Thus, (5.7) can evaluate the consistency between the Welch-estimated PSD and the expected PSD based on the BEM.

Without normalisation by $|R_{mm}(e^{j\Omega_k}, n)|^2$, the metric in (5.7) would resemble the squared moment error terms in [255], where a trade-off between squared bias and variance arises. Intuitively, this reflects a trade-off between estimation errors caused by an insufficient sample size N and the fact that the time average over a window N could obscure and blur the underlying dynamics of the time-varying quantities [256].

5.4.2 Space-Time Covariance Matrix Estimation

An alternative to the Welch method is to estimate sensor PSDs as part of space-time covariance estimation as outlined earlier in Secs. 3.7.3 and 3.7.4, which here is refreshed for convenience, and adjusted to fit the centred window used in the Welch estimate in

Sec. 5.4.1. In multichannel signal processing, estimating the space-time covariance matrix is essential for tasks such as beamforming [257], spectral estimation [104], and signal detection [5, 44]. This matrix is derived from cross-correlation sequences $r_{m\mu}[\tau]$, which indicate the statistical dependence between sensor signals m and μ over different time lags τ . To estimate these from snapshots of N data, the best linear unbiased estimator (BLUE) [195, 197] is given by

$$\hat{r}_{m\mu}[\tau, n] = \begin{cases} \frac{1}{N-|\tau|} \sum_{\nu=n-\frac{N}{2}}^{n+\frac{N}{2}-|\tau|-1} x_m[\nu+\tau]x_{\mu}^*[\nu], & \tau \geq 0; \\ \frac{1}{N-|\tau|} \sum_{\nu=n-\frac{N}{2}}^{n+\frac{N}{2}-|\tau|-1} x_m[\nu]x_{\mu}^*[\nu-\tau], & \tau < 0. \end{cases} \quad (5.8)$$

The formulation (5.8) ensures that for each τ , the estimator uses the maximally available number of overlapping samples and adjusts the averaging length accordingly. However, the varying number of terms in the summation means that for larger values of $|\tau|$, i.e., longer lags, the estimate is based on fewer samples, thus reducing the estimator's confidence. Note that different from (3.38), the estimation in (5.8) operates with a window that is centred around the current time instance n in order to be somewhat robust to time-variations of the underlying statistics.

For stationary Gaussian data, the variance of this estimate can be expressed [195, 197] as

$$\text{var} \{ \hat{r}_{m\mu}[\tau] \} = \frac{1}{(N-|\tau|)^2} \sum_{t=-N+|\tau|+1}^{N-|\tau|-1} (N-|\tau|-|t|) \cdot (r_{mm}[t]r_{\mu\mu}^*[t] + \bar{r}_{m\mu}[\tau+t]\bar{r}_{m\mu}^*[\tau-t]), \quad (5.9)$$

where $\bar{r}_{m\mu}[\tau] = \mathcal{E} \{ x_m[n]x_{\mu}[n-\tau] \}$ is the complementary cross-correlation sequence, which becomes relevant for noncircular or improper complex signals [205]. Due to the bias-free nature of the estimate in (5.8), the variance in (5.9) therefore equals the power of the estimation error. It relies on the sample size, N , the lag τ , and the underlying

auto- and cross-correlation sequences of the sensor signals.

With (5.8) for the diagonal terms, we have $\hat{R}_{\text{STC},mm}(e^{j\Omega}, n) \bullet\text{--}\circ \hat{r}_{mm}[\tau, n]$ for the estimated PSD based on the space-time covariance. This is generally more computationally expensive than the Welch method in Sec. 5.4.1, but offers some advantages that will be explored below in Sec. 5.5. To quantify the error between the true and the estimated PSD via (5.8), $\hat{R}_{\text{STC},mm}(e^{j\Omega}, n)$, we can define a normalised error

$$e_{\text{STC}}[n] = \sum_{m=1}^M \frac{\int_{-\pi}^{\pi} |R_{mm}(e^{j\Omega}, n) - \hat{R}_{\text{STC},mm}(e^{j\Omega}, n)|^2 d\Omega}{\int_{-\pi}^{\pi} |R_{mm}(e^{j\Omega}, n)|^2 d\Omega}. \quad (5.10)$$

This metric captures the mean squared relative error; its computation can be performed via Parseval's theorem in the time domain, summing over the discrete coefficients of the auto-correlation and estimated auto-correlation terms.

In the stationary case, applying Parseval's theorem [258], the expected value of the numerator will equal $\sum_{\tau} \text{var} \{\hat{r}_{mm}[\tau]\}$; thus, the error depends not only on the ground truth space-time covariance and the sample size N , but also on the lag support $|\tau| < T$ over which the variance terms are summed. In the non-stationary case, (5.8) will represent a time-averaged version [256], introducing an additional source of error due to the blurring effect on the expected underlying auto- and cross-correlations.

5.5 PSD Via Enhanced Covariance Estimation

The space-time covariance method for estimating the sensor PSDs in Sec. 5.4.2 is more computationally intensive than the approach in Sec. 5.4.1, but presents opportunities for improved performance, which we discuss below.

5.5.1 Optimized Lag Support

The lag support T for the space-time covariance estimate directly impacts on the quality of the autocorrelation (and consequently the PSD) estimates. In the stationary case,

a lag support that is too short results in truncation errors, while one that is too long introduces extra noise to the estimate. This issue is further exacerbated in the non-stationary case by the averaging effect across time-varying statistics over the time window of length N . Therefore, an optimal lag exists that minimizes the error in (5.10). Generally, we find that if the innovation filter $h_{m,q}[n]$ has a length L , then for the optimal lag support, we have $T_{\text{opt}} < (L - 1)$. In the stationary case, this optimal lag support can be estimated based on the decay pattern of any auto- or cross-correlation term [196, 197], which we utilize here.

5.5.2 Rank One Approximation

By either reparameterizing the CSD matrix in Sec. 5.3.1 with $z = e^{j\Omega}$ or by evaluating the z transform $\mathbf{R}(z, n) = \sum_{\tau} \mathbf{R}[\tau, n]z^{-\tau}$, we obtain a matrix of analytic functions in the z domain, vital for signal processing and systems theory. Assuming sufficiently small time variations $|\Omega_{m,q}| \ll 1$, and small values for L , i.e. slow variation with frequency, the frequency shifts are such that in (5.6), $H_{m,p}(e^{j(\Omega - \Omega_{m,q})}) \approx H_{m,p}(e^{j\Omega})$, i.e. $e^{j\Omega_{m,q}} \approx 1$. Despite this assumption, the modulation term $e^{j(\Omega_{m,p} - \Omega_{\mu,q})n}$ can still take on significant phase values as n increases. Thus, we have

$$R_{m\mu}(z, n) \approx \sum_{p,q=1}^Q e^{j(\Omega_{m,p} - \Omega_{\mu,q})n} H_{m,p}(z) H_{\mu,q}^{\text{P}}(z), \quad (5.11)$$

where $R_{m\mu}(z, n)$ denotes the CSD between channels m and μ . The transfer function from source p to channel m is represented by $H_{m,p}(z)$, while $\Omega_{m,p}$ is the time-varying frequency modulation term for channel m and path p , influencing the time-dependent PSD of the sensor signals.

With the approximation in (5.11), $\mathbf{R}(z, n) \approx \mathbf{h}(z, n)\mathbf{h}^{\text{H}}(z, n)$ imposes a rank-one structure on the CSD matrix, which implicitly corresponds to a single dominant source or a fully coherent source field. Although the original formulation allows multiple sources, this separable representation is exact only under source coherence or when a single source dominates. Hence, the approximation constitutes a strong simplification

that may not hold in general multi-source scenarios, where $\mathbf{R}(z, n)$ is inherently higher rank and can be expressed as a rank one outer product, where

$$\mathbf{h}^P(z, n) = \sum_q [e^{j\Omega_{1,q}n} H_{1,q}(z), \dots, e^{j\Omega_{M,q}n} H_{M,q}(z)]^P. \quad (5.12)$$

In contrast, due to noise and estimation errors, the estimated CSD matrix will almost surely possess full rank [200], i.e., this means with probability one. Therefore, based on the analytic EVD [105, 109, 121, 156, 160] of $\hat{\mathbf{R}}(z, n) = \sum_m \mathbf{q}_m(z, n) \lambda_m(z, n) \mathbf{q}_m^P(z, n)$ calculated using algorithms from, e.g. [145–147, 150, 151, 222, 259], we form a rank-one approximation

$$\hat{\mathbf{R}}_1(z, n) = \mathbf{q}_1(z, n) \lambda_1(z, n) \mathbf{q}_1^P(z, n), \quad (5.13)$$

assuming that $\{\lambda_1(z, n), \mathbf{q}_1(z, n)\}$ is the dominant eigenpair of $\hat{\mathbf{R}}(z, n)$. We can then obtain denoised estimates $\hat{R}_{1,mm}(e^{j\Omega}, n)$ by evaluating the diagonal terms of (5.13) on the unit circle, i.e. $\hat{R}_{1,mm}(e^{j\Omega}, n) = q_{1,m}(z, n) \lambda_m(z, n) q_{1,m}^P(z, n)$, where $q_{1,m}(z, n)$ is the m th element of the principal eigenvector $\mathbf{q}_1(z, n)$.

With $\hat{R}_{1,mm}(e^{j\Omega}, n)$, we associate the normalized PSD error

$$e_{R-1}[n] = \sum_{m=1}^M \frac{\int_{-\pi}^{\pi} |R_{mm}(e^{j\Omega}, n) - \hat{R}_{1,mm}(e^{j\Omega}, n)|^2 d\Omega}{\int_{-\pi}^{\pi} |R_{mm}(e^{j\Omega}, n)|^2 d\Omega}, \quad (5.14)$$

which can again be evaluated based on Parseval and the corresponding time-domain quantities. The expression (5.14) thus evaluates the effectiveness of the rank one approximation in matching the actual signal PSD at time n .

Example 12 *For the scenario in Example 10 and with $M = 4$ sensors, we determine $\hat{R}_{1,mm}(e^{j\Omega}, n)$ in $K = 32$ bins for a sample size of $N = 2^{10}$, with the result shown in Fig. 5.4. This estimate looks like a closer match to the ground truth in Fig. 5.2 than the PSD estimate via the Welch method in Fig. 5.3.*

In order to quantify the result of Example 12 systematically, some ensemble simu-

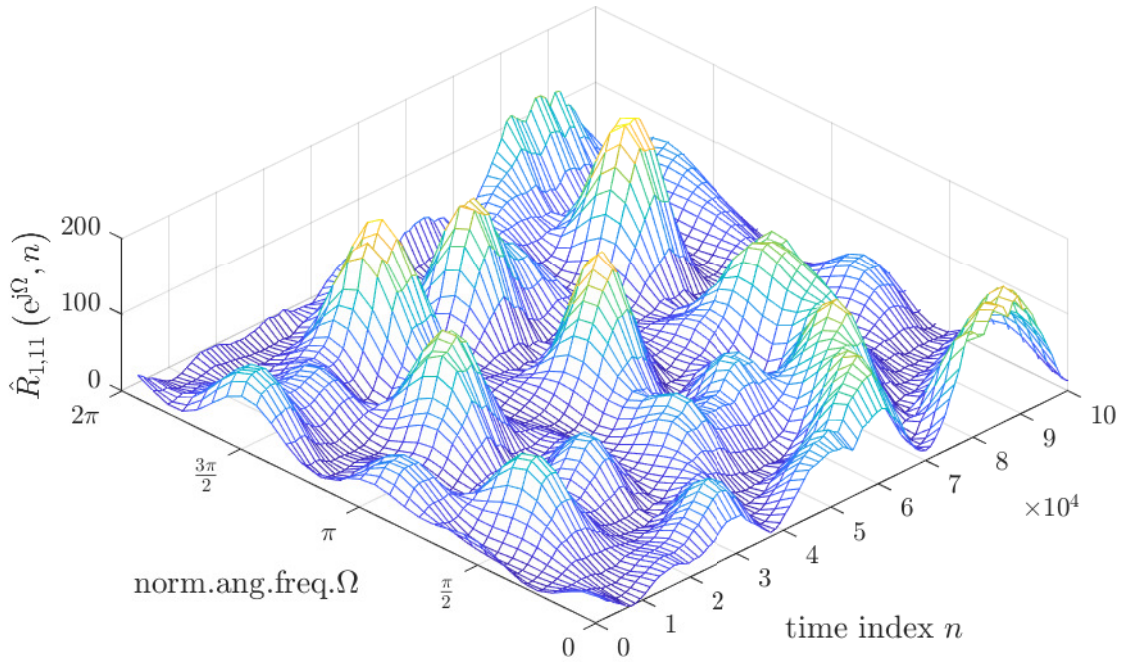


Figure 5.4: Result of Example 12 for time-varying PSD estimation based on rank-one space-time covariance matrix estimations.

lations are presented next.

5.6 Results

Some initial result for the rank one PSD estimation with optimized space-time covariance support has been presented in Fig. 5.4 in comparison to the Welch estimate in Fig. 5.3. To investigate the proposed method for a wider range of situations, this section will present a number of ensemble results over different randomized instances of the BEM. First, Sec. 5.6.1 will layout simulation parameters and performance metrics, followed by results for the PSD estimation in Sec. 5.6.2.

5.6.1 Parameters and Metrics

We aim to investigate the dependency on the spatial dimension M , on the lag support T of the space-time covariance estimate when it is not optimally chosen, and on the rate of non-stationarity loosely defined by Ω_{\max} , which limits the uniform distribution from which Doppler frequencies are sampled. We operate with $Q = 10$ paths in the BEM based on sufficiency comments in [246], each with a temporal dimension of $L = 5$.

For the assessment, we will utilise the normalised error metrics in (5.7), (5.10), and (5.14), averaging the results over an ensemble of randomised signals and BEM instantiations. This yields the metrics \bar{e}_{Welch} , \bar{e}_{STC} and $\bar{e}_{\text{R-1}}$ for the Welch PSD estimate [4], the space-time covariance approach, and its rank one approximation, respectively.

5.6.2 Ensemble Results

In the first test, we examine the performance benefits of the methods in Sec. 5.5 when operating in a stationary environment with $\Omega_{\max} = 0$. We select a lag support $T \in [0, 15]$ for the space-time covariance matrix estimate, and use the Welch approach with a fixed value of $K = 32$ as a reference. For $M \in \{4, 8\}$ and sample size $N \in \{64, 512\}$, Fig. 5.5 shows three different ensemble mean PSD errors. The impact of the spatial dimension M is minimal, with little difference between the curves for $M = 4$ and $M = 8$, particularly for the larger sample size N . The lag support indicates approximately minimal mean square error values of $T \approx 3$ for $N = 64$ and $T \approx 4$ for $N = 512$, which is consistent with the findings in [197]: for small T , the error is dominated by truncation effects, while for large T , the error is mostly affected by estimation errors in zero-padded autocorrelation coefficients. The rank-one approximation provides an advantage as the analytic EVD is not distorted by excessive estimation errors, unlike, for example, when $T \rightarrow 0$.

Next, we investigate the impact of non-stationary statistics by varying Ω_{\max} across a range of values. Generally, we assume that Doppler shifts of the $Q = 10$ paths in the BEM are small in order to satisfy the approximation in (5.11). For $M = 4$

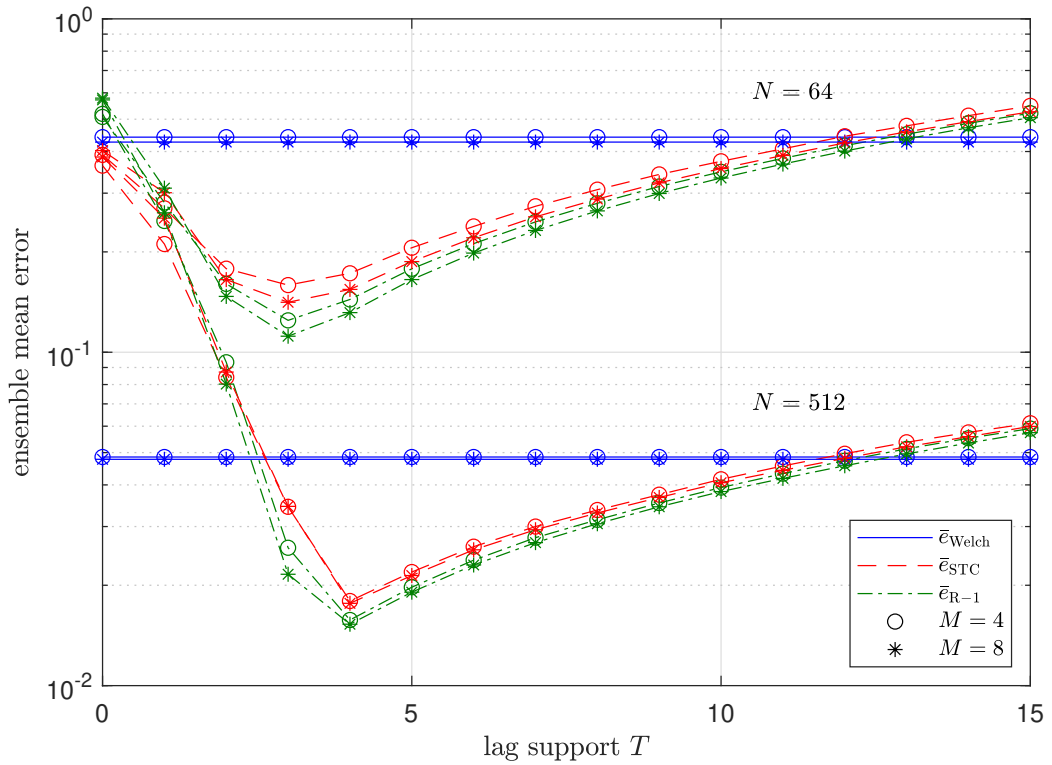


Figure 5.5: Ensemble mean PSD errors, where \bar{e}_{STC} and $\bar{e}_{\text{R-1}}$ depend on different lag supports T for the space-time covariance estimate. The two groups of curves are for different sample sizes of $N = 64$ and $N = 512$.

and different sample sizes $N = 2^6, \dots, 2^{14}$, Fig. 5.6 illustrates the results for the mean errors for three different ensembles in the PSD estimates, with the lag support adjusted according to [196, 197].

For small values of N , estimation errors from insufficient sample sizes dominate the error curves, and the optimum support generates a significant performance advantage, with a small added bonus for a rank-one approximation, which appears to act as a denoising method. As N increases, this observation remains true for sufficiently small Doppler shifts Ω_{max} . But as both Ω_{max} and N increase, a ‘sweet spot’ for the PSD estimation errors exists w.r.t. a trade-off between (i) noise terms due to an insufficient sample size N and (ii) the averaging over the ground-truth time-varying statistics (as limited by Ω_{max}) as N increase. Thus, the performance advantage for the space-time

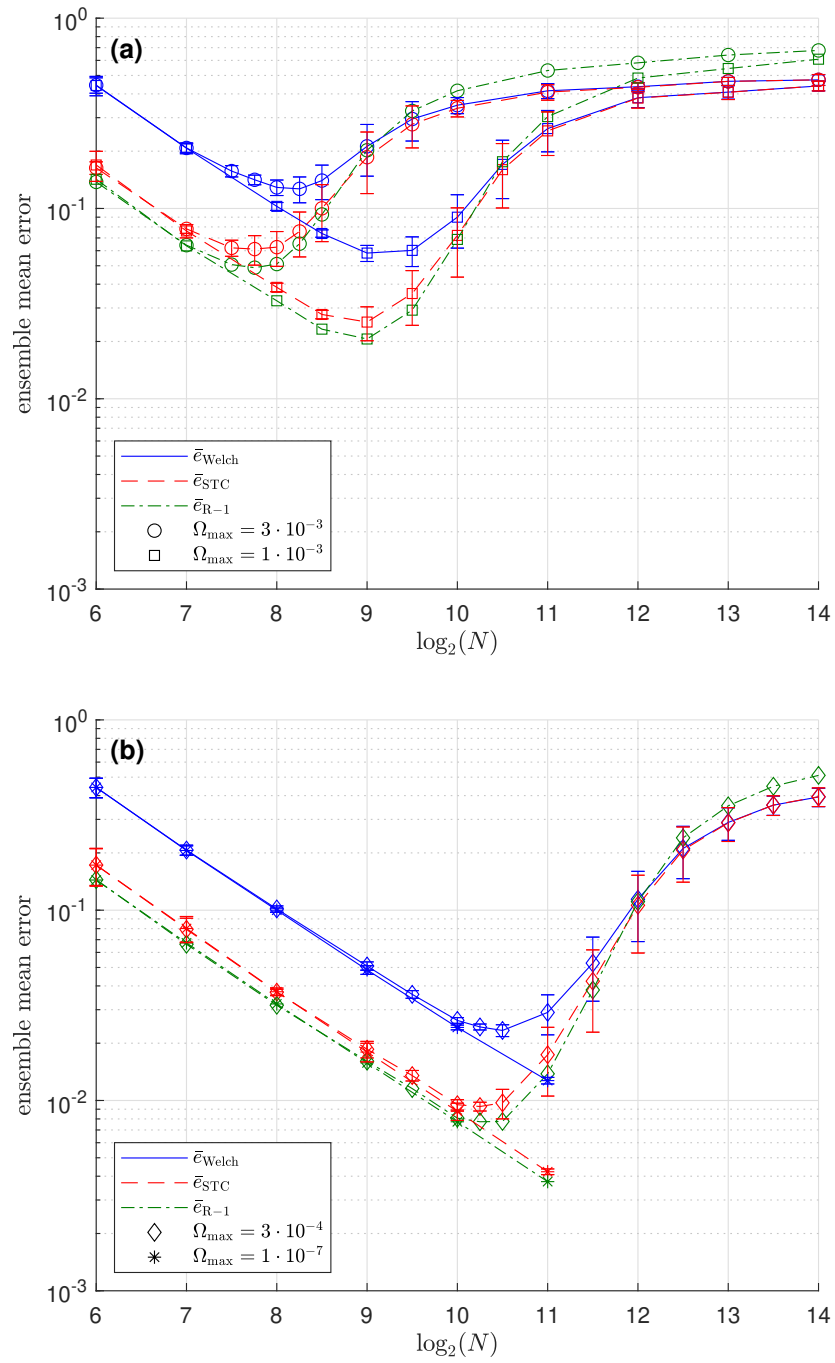


Figure 5.6: Ensemble mean errors for PSD estimates as a function of sample size N for maximum Doppler frequency Ω_{max} in the BEM. Error bars represent one standard deviation of the ensemble distribution. (a) Higher Ω_{max} ; (b) Lower Ω_{max} .

covariance estimation with optimum support size proposed in Sec. 5.5 decreases with increasing N and Ω_{\max} and converges towards the same performance as the Welch approach, since both rely on the same sample size N and errors are dominated by averaging across time-varying statistics.

W.r.t. the proposed rank-one approximation, as N and Ω_{\max} increase in Fig. 5.6, and the advantage offered by the rank-one approximation for low values of N is negated. This is likely due to the perturbation of the analytic EVD. The performance of \bar{e}_{STC} already points to a large error term in the space-time covariance estimate, which subsequently translates into a subspace perturbation and subsequent errors in the rank-one approximation. Also, the effect is already more pronounced at smaller values of N for larger Doppler shift limits Ω_{\max} , which will impose fast-changing statistics that can already be felt when averaging over shorter time intervals N .

However, with optimal sample size selection N , specifically at the minimum of the curves shown, the proposed methods of adjusting the lag support and performing denoising with a rank-one approximation can reduce PSD estimation errors. Since Fig. 5.6 also shows error bars indicating the standard deviation for the experiments, note that at the minima of the ensemble error curves, the means \bar{e}_{STC} and $\bar{e}_{\text{R-1}}$ are separated of by at least one standard deviation, and hence the performance improvement is significant.

Among the evaluated estimators, the R-1 estimator demonstrates superior performance, achieving the lowest mean errors when the sample size N is adjusted optimally. The space-time covariance method outperforms the classical, lower-cost Welch method, though it lags behind the rank-one estimator, indicating a trade-off between computational complexity and accuracy.

5.7 Chapter Summary

This chapter has examined the estimation of time-varying PSDs due to a single source using a sensor array. The model used a stationary source and assigned the time-varying behavior to the transfer paths, for which we employed a BEM. This model allows control over time variation by limiting the maximum Doppler shift and can adjust frequency

selectivity by selecting different filter orders for the fixed, time-invariant filters in each BEM path. Our investigation, grounded in space–time covariance estimation, demonstrated the advantages of (i) optimizing lag support to reduce estimation error and (ii) applying denoising through rank-one approximation via an analytic EVD. For slowly varying systems, even though computationally more expensive, these approaches can offer substantial performance improvements.

The proposed method can be adapted to accommodate multiple noise sources by estimating the number of dominant sources and applying a low-rank approximation accordingly. Source enumeration is not a straightforward task even when using covariance matrices in the narrowband case [260–262]. For the broadband case, the topic of source enumeration for space–time covariance matrices in the presence of unstructured additive noise has been explored in [5]; similar strategies could be adopted here. However, unstructured noise will impose a lower bound on any PSD, limiting the effectiveness of low-rank denoising as the number of sources increases.

In the wider context of this thesis and of detecting and protecting PUs, the method proposed in this chapter opens the possibility of detecting opportune moments and frequency bands when noise power is low and, hence, potential SNR is high. For the method in Chap. 3, where we wanted to detect the emergence of weak (e.g., distant) PUs, the SNR between the signal to be detected and the background noise was crucial for both the probability of detection and the time required to establish a reliable detection. For the method in Chap. 4, the ability to jam an undesired source depended on the receive SNR — the ratio between the power of the undesired source’s signal and the power of the noise; thus, the method proposed in this chapter points a way to detect when the receive SNR is opportune to enable jamming such an undesired source via the time reversal technique.

Chapter 6

Conclusions and Future Work

6.1 Summary and Conclusions

In the context of CRNs, this thesis has addressed a number of problems. Firstly, we have investigated energy detection of PU or other sources. Secondly, interference control has been addressed through targeted jamming in order to deny service or enforce spectral policing w.r.t. undesired sources while protecting the integrity of desired users. Finally, this thesis has investigated estimation techniques for fluctuating PSD due to a noise source in order to identify suitable windows of opportunity, e.g., where weak emerging PUs can be detected or signals to be used for jamming via time reversal can be acquired. The last chapter of this thesis now provides a summary of the work presented in Chapters 3 to 5, and puts forward a number of ideas of how this research could be taken further.

Chapter 3 has addressed the problem of detecting weak broadband transient signals, such as from emerging PUs. A polynomial subspace detection framework was presented and analyzed using the syndrome-energy approach within a polynomial matrix formulation. To better understand the potential of this subspace approach, we benchmarked its performance against the LRT, which represents the optimal detector with full channel knowledge. For this, both the LRT and the GLRT, the latter based on estimated space-time covariance matrices, were derived and tested on both

the array measurements, but also on the subspace data. For short-time averaging over syndrome energy, the LRT/GLRT performs substantially better than the polynomial subspace approach. However, for longer data windows and in cases of high temporal correlation of the received data, it becomes surprisingly advantageous to operate on the lower-dimensional subspace data rather than the array data due to the poor conditioning and large matrix dimensions that result from the latter. Thus, by incorporating a broadband subspace projection as a preprocessing step into the LRT/GLRT, both the conditioning of the covariance matrix and the computational efficiency of the LRT/GLRT were significantly improved; further, the subspace approach whitens the data due to the strong decorrelation property of the analytic EVD. The improvement in conditioning is due to the suppression of the dominant eigenvalues when projected onto the noise-only subspace, thereby reducing the condition number of the covariance matrix. The subspace projection is also responsible for the dimensionality reduction. Finally, the strong decorrelation property of the analytic EVD, which drives the subspace partitioning, leads to temporally uncorrelated subspace data. Since temporal correlation increases the variance of an estimate, removing such temporal correlation results in lower variance and better discrimination of statistics. This therefore explains why in broadband scenarios with temporally correlated data, it is advantageous to operate on the subspace data rather than on the raw array data. We have thus explored and motivated the use of the simple syndrome energy detection.

The above broadband subspace detection approach was initially motivated by the detection of hostile broadband trigger signals, such as those associated with improvised explosive devices. Thus, Chapter 4 investigated the transition from detection to active countermeasures, i.e. the jamming and suppression of such a source. In a CR context, such a technique could also be used to suppress uncooperative SUs or to police the spectrum. To achieve this, a time-reversal-based jamming strategy was developed to generate targeted interference without affecting desired users and without requiring explicit knowledge of the hostile source–array channel. To analyse the performance of such a time-reversal technique, we used an analytic SVD of the broadband channel

matrices. The performance of the time reversal scheme was characterized and compared with that of a broadband beamforming approach. The latter, in practice, assumes that all channel matrices are known and defines the upper performance bound for the time reversal method. The results demonstrated that time reversal performs well under moderate receive SNR conditions but degrades as the signal noise power used for time reversal increases. This highlights the critical role of the received SNR in determining the operational viability of the proposed jamming strategy.

Since both the transient signal detection in Chapter 3 and the time reversal approach in Chapter 4 depend on the SNR, Chapter 5 introduced techniques for estimating the PSD under slowly time-varying conditions. The purpose of this estimation is then to identify windows of opportunity where the noise power is sufficiently low. The time-varying nature of the noise was ascribed to a time-varying transmission channel via a BEM to represent the nonstationary propagation environment. Such a BEM can represent complex scenarios and allows explicit control over Doppler spread and frequency selectivity. Specifically, this thesis presented an array-based PSD approach, based on space-time covariance estimations. The estimation accuracy could be enhanced by optimising support for this space-time covariance matrix, combined with a rank-one approximation via an analytic EVD. Compared to the classical Welch method for PSD estimation, the approach — albeit at an increased computational cost — provides significant performance advantages. Together, the methods developed in this thesis establish a coherent processing chain that links weak-signal detection, environmental awareness through PSD estimation, and targeted broadband interference via time reversal. In the broader context of protecting PUs and suppressing hostile emitters, the proposed framework enables the identification of "windows of opportunity" in terms of time–frequency regions where the noise power is low and the receive SNR may be sufficiently high to support both reliable detection and recording signals for effective jamming via time reversal techniques. This closes an important conceptual gap between passive sensing and active interference control in dynamic broadband environments.

6.2 Suggestions for Future Work

This section outlines potential future research directions based on the findings presented in this thesis.

Robust Detection and Model Mismatch. The polynomial subspace framework performs well under the assumptions of Gaussian data and of stationary users defining the signal-plus-noise subspace, but it only considers how well distributions are separable without deriving any precise detection thresholds. Future work should investigate how detection thresholds can be determined and how the approach behaves when the channels become time-varying. This can be expected to result in subspace leakage [197], which has also been experienced in Chapter 3 through estimation errors. The BEM in Chapter 5 would form a useful simulation tool, and could reveal the sensitivity of the syndrome approach to channel variations. Extensions to adaptive or learning-based subspace tracking methods may further enhance detection reliability in highly dynamic environments.

Further deviations from the assumptions could include non-Gaussian signals, such that the syndrome energy no longer follows a χ^2 distribution, and their impact on the variance of the estimates and on the discrimination between the cases of absence or presence of a transient source. Also, the additive noise component in the model could be coloured or otherwise structured.

Joint Detection and Jamming Optimization. In this work, detection and jamming were treated as sequential stages. Future work could focus on a unified optimization framework that jointly optimizes detection thresholds, time reversal waveform design, and power allocation under SNR, latency, and interference-avoidance constraints. A joint framework enables global co-design of detection thresholds, waveform, and power allocation, in contrast to the locally optimal and decoupled nature of sequential approaches. By explicitly accounting for their mutual coupling, it can achieve improved detection–jamming trade-offs, more efficient resource allocation, and greater

robustness to channel and interference uncertainties. Consequently, it is expected to provide non-trivial performance gains over separate-stage designs.

PSD Prediction. The estimation approach in Chapter 5 is based on a smooth evolution of PSD across an array over time. It therefore lends itself to a prediction approach, i.e. using a Wiener filter [179, 263, 264], where upcoming windows of opportunity might be determined in order to plan for real-time detection or acquisition of signals for jamming via time reversal techniques, which could be extended from the current estimation to prediction of low rank rather than rank one. In the presence of known, structured, stronger signals, the noise PSD estimation could be performed on the noise-only subspace, using a broadband subspace projection technique as outlined in Chapter 3.

Enhanced PSD Estimation. The approach in Chapter 5 assumed only a single noise source in the environment. If the noise is in the presence of strong, desired user signals, it should be possible to operate the PSD estimation technique in the noise subspace, as identified in Chapter 3. Further, even if there are multiple noise sources, the approach can still employ a support optimisation technique. If it is possible to enumerate the noise sources, e.g., by determining the number of dominant analytic eigenvalues, then a low-rank rather than a rank-one approximation can be performed. The denoising effect may decrease with the number of noise sources, but an advantage may still be achieved. A key extension is to generalize the PSD estimation framework to handle multiple noise sources. This requires moving beyond rank-one approximations to low-rank, adaptive subspace models, where the number of active noise components can be estimated and tracked over time. Incorporating regularization, subspace separation, and spatio-temporal smoothing can improve robustness under limited samples, closely spaced sources, or strong desired signals. While denoising gains may diminish as the number of noise sources increases, such a framework is expected to retain significant advantages over conventional full-rank estimation and provide a principled basis for handling complex, dynamic interference scenarios.

Hardware Implementation and Experimental Validation. In order to investigate whether the proposed techniques are technically feasible, and to move towards real-world testing, a hardware implementation is required. An implementation could e.g. be attempted on the Zynq Ultrascale+ RFSoc platform [265]. This platform offer 8 input and 8 output channels with ADCs and DACs operating at beyond 5 Gsps. For polynomial matrix techniques, a number of numerical [266] and implementation tricks [222] can be exploited for such an implementation. One challenge in experimental validation is accurately modeling multi-source noise and interference. The current work uses simplified assumptions, like a single noise source, for clearer analysis. However, incorporating multiple noise sources raises issues such as model order uncertainty, correlated interferers, and higher computational demands. Realistic simulations require well-designed channel models, interference statistics, and increased scenario diversity, leading to longer simulation times. This has led to a more controlled initial evaluation, with the intention of integrating hardware prototyping and enhanced simulation environments in future work for real-world deployment.

Bibliography

- [1] M. H. Islam, C. L. Koh, S. W. Oh, X. Qing, Y. Y. Lai, C. Wang, Y. C. Liang, B. E. Toh, F. Chin, G. L. Tan, and W. Toh, “Spectrum survey in singapore: Occupancy measurements and analyses,” in *2008 3rd International Conference on Cognitive Radio Oriented Wireless Networks and Communications (CrownCom 2008)*. IEEE, May 2008, pp. 1–7.
- [2] J. Mitola and G. Q. Maguire, “Cognitive radio: making software radios more personal,” *IEEE personal communications*, vol. 6, no. 4, pp. 13–18, 1999.
- [3] I. F. Akyildiz, W.-Y. Lee, M. C. Vuran, and S. Mohanty, “A survey on spectrum management in cognitive radio networks,” *IEEE Communications Magazine*, vol. 46, no. 4, pp. 40–48, 2008.
- [4] P. D. Welch, “The use of fast Fourier transform for the estimation of power spectra: A method based on time averaging over short, modified periodograms,” *IEEE Transactions on Audio and Electroacoustics*, vol. 15, no. 2, pp. 70–73, 1967.
- [5] S. Weiss, C. Delaosa, J. Matthews, I. K. Proudler, and B. A. Jackson, “Detection of weak transient signals using a broadband subspace approach,” in *2021 Sensor Signal Processing for Defence Conference (SSPD)*, Edinburgh, UK, September 2021, pp. 1–5.
- [6] M. Matinmikko-Blue, S. Yrjölä, and P. Ahokangas, “Spectrum management in the 6g era: The role of regulation and spectrum sharing,” in *2nd 6G Wireless Summit*, Levi, Finland, 2020, pp. 1–5.

Bibliography

- [7] J. Reed, M. Vassiliou, and S. Shah, “The role of new technologies in solving the spectrum shortage [point of view],” *Proceedings of the IEEE*, vol. 104, no. 6, pp. 1163–1168, 2016.
- [8] F. C. Commission *et al.*, “Fcc opens 6 ghz band to wi-fi and other unlicensed uses,” *FCC Report and Order*, 2020.
- [9] L. Zhang, M. Xiao, G. Wu, M. Alam, Y.-C. Liang, and S. Li, “A survey of advanced techniques for spectrum sharing in 5G networks,” *IEEE Wireless Communications*, vol. 24, no. 5, pp. 44–51, 2017.
- [10] F. Hu, B. Chen, and K. Zhu, “Full spectrum sharing in cognitive radio networks toward 5G: A survey,” *IEEE Access*, vol. 6, pp. 15 754–15 776, 2018.
- [11] S. Anusha, V. Mohanraj, Y. Suresh, and J. Senthil, “Cooperative spectrum sensing in wireless sensor networks using forager bee’s intelligence,” *Journal of Ambient Intelligence and Humanized Computing*, vol. 12, pp. 5553–5560, 2021.
- [12] Cisco, “Cisco visual networking index: Global mobile data traffic forecast update, 2015–2020,” <http://www.cisco.com/c/en/us/solutions/collateral/service-provider/visual-networking-index-vni/mobilewhite-paper-c11-520862.html>, 2016, retrieved May 2016.
- [13] Federal Communications Commission, “Spectrum Policy Task Force Report,” Federal Communications Commission, Technical Report 02-135, Nov. 2002, available: http://hraunfoss.fcc.gov/edocs_public/attachmatch/DOC-228542A1.pdf.
- [14] M. A. McHenry, P. A. Tenhula, D. McClosky, D. A. Roberson, and C. S. Hood, “Chicago spectrum occupancy measurements & analysis and a long-term studies proposal,” in *Proceedings of the First International Workshop on Technology and Policy for Accessing Spectrum (TAPAS’06)*, Boston, MA, August 2006.

Bibliography

- [15] I. F. Akyildiz, W.-Y. Lee, M. C. Vuran, and S. Mohanty, “Next generation/dynamic spectrum access/cognitive radio wireless networks: A survey,” *Computer Networks*, vol. 50, no. 13, pp. 2127–2159, 2006.
- [16] N. Singh, Y. Tang, Z. Zhang, and C. Zheng, “Covid-19 waste management: Effective and successful measures in wuhan, china,” *Resources, conservation, and recycling*, vol. 163, p. 105071, 2020.
- [17] M. McHenry, “NSF Spectrum Occupancy Measurements Project Summary,” Shared Spectrum Company (SSC), Technical Report, Aug. 2005, available: <http://www.sharespectrum.com/>.
- [18] A. Ghasemi and E. S. Sousa, “Spectrum sensing in cognitive radio networks: requirements, challenges and design trade-offs,” *IEEE Communications magazine*, vol. 46, no. 4, pp. 32–39, 2008.
- [19] S. Haykin, “Cognitive radio: Brain-empowered wireless communications,” *IEEE Journal on Selected Areas in Communications*, vol. 23, no. 2, pp. 201–220, Feb. 2005.
- [20] I. J. Mitola, “Software radios: Survey, critical evaluation and future directions,” *IEEE Aerospace and Electronic Systems Magazine*, vol. 8, no. 4, pp. 25–36, Apr. 1993.
- [21] A. Shukla, A. Alptekin, J. Bradford, E. Burbridge, D. Chandler, M. Kennett, P. Levine, and S. Weiss, “Cognitive radio technology — a study for OFCOM,” OFCOM, London, UK, Tech. Rep., Feb. 2007.
- [22] Working Group on Wireless Regional Area Networks, “IEEE Std. 802.22,” <http://www.ieee802.org/22/>, n.d., [Online].
- [23] Y. Zhao, L. Morales, J. Gaeddert, K. K. Bae, J.-S. Um, and J. H. Reed, “Applying radio environment maps to cognitive wireless regional area networks,” in *2007 2nd*

Bibliography

- IEEE International Symposium on New Frontiers in Dynamic Spectrum Access Networks*. IEEE, 2007, pp. 115–118.
- [24] M. R. Brew, F. Darbari, L. H. Crockett, M. B. Waddell, M. Fitch, S. Weiss, and R. W. Stewart, “Uhf white space network for rural smart grid communication,” in *2nd IEEE Smart Grid Communications Conference*, Brussels, Belgium, October 2011, pp. 138–142.
- [25] C. McGuire, M. R. Brew, F. Darbari, S. Weiss, and R. W. Stewart, “Enabling rural broadband via tv ”white space”,” in *International Symposium on Communications, Control and Signal Processing*, Rome, Italy, May 2012.
- [26] R. Elliot, M. Enderwitz, K. Thompson, L. Crockett, S. Weiss, and R. Stewart, “Wideband TV white space transceiver design and implementation,” *IEEE Transactions on Circuits and Systems II: Express Briefs*, vol. 63, no. 1, pp. 24–28, January 2016.
- [27] C. Cordeiro, K. Challapali, and D. Birru, “IEEE 802.22: An introduction to the first wireless standard based on cognitive radios,” *Journal of Communications*, vol. 1, no. 1, pp. 38–47, Apr. 2006.
- [28] C. M. Cordeiro, M. Ghosh, D. Cavalcanti, and K. Challapali, “Spectrum sensing for dynamic spectrum access of TV bands,” in *Proceedings of the International Conference on Cognitive Radio Oriented Wireless Networks and Communications (CrownCom)*, Orlando, FL, Aug. 2007.
- [29] S. J. Shellhammer, S. S. N, R. Tandra, and J. Tomcik, “Performance of power detector sensors of DTV signals in IEEE 802.22 WRANs,” in *Proceedings of the ACM International Workshop on Technology and Policy for Accessing Spectrum (TAPAS)*, Boston, MA, Aug. 2006.
- [30] L. Lv, J. Chen, Q. Ni, Z. Ding, and H. Jiang, “Cognitive non-orthogonal multiple access with cooperative relaying: A new wireless frontier for 5g spectrum sharing,” *IEEE Communications Magazine*, vol. 56, no. 4, pp. 188–195, 2018.

Bibliography

- [31] S. Oh and W. Choi, “A hybrid cognitive radio system: A combination of underlay and overlay approaches,” *IEEE Transactions on Cognitive Radio*, 2009.
- [32] Y. Qian and W. Chen, “Wideband spectrum sensing in cognitive radio with structured bayesian compressed sensing by variational bayesian approach,” in *9th International Congress on Image and Signal Processing, BioMedical Engineering and Informatics (CISP-BMEI)*. IEEE, 2016, pp. 1128–1132.
- [33] P. Leaves, K. Moessner, R. Tafazolli, D. Grandblaise, D. Bourse, R. Tönjes, and M. Breveglieri, “Dynamic spectrum allocation in composite reconfigurable wireless networks,” *IEEE Communications Magazine*, vol. 42, no. 5, pp. 72–81, 2004.
- [34] Y. Zou, Y.-D. Yao, and B. Zheng, “Cognitive transmissions with multiple relays in cognitive radio networks,” *IEEE Transactions on Wireless Communications*, vol. 10, no. 2, pp. 648–659, 2011.
- [35] F. K. Jondral, “Software-defined radio—basics and evolution to cognitive radio,” *EURASIP journal on wireless communications and networking*, vol. 2005, no. 3, p. 652784, 2005.
- [36] K. R. Liu and B. Wang, *Cognitive radio networking and security: A game-theoretic view*. Cambridge University Press, 2010.
- [37] C. Stevenson, G. Chouinard, Z. Lei, W. Hu, S. Shellhammer, and W. Caldwell, “IEEE 802.22: The first cognitive radio wireless regional area network standard,” *IEEE Communications Magazine*, vol. 47, no. 1, pp. 130–138, Jan. 2009.
- [38] B. Wang and K. R. Liu, “Advances in cognitive radio networks: A survey,” *IEEE Journal of selected topics in signal processing*, vol. 5, no. 1, pp. 5–23, 2010.
- [39] M. Sherman, A. Mody, R. Martinez, R. Reddy, and C. Rodriguez, “IEEE standards supporting cognitive radio and networks, dynamic spectrum access, and coexistence,” *IEEE Communications Magazine*, pp. 72–79, 2008.

Bibliography

- [40] M. Ali and H. Nam, “Optimization of spectrum utilization in cooperative spectrum sensing,” *Sensors*, vol. 19, no. 8, p. 1922, 2019.
- [41] A. N. Akhtar, F. Arif, and A. M. Siddique, “Spectrum decision framework to support cognitive radio based IoT in 5G,” in *Cognitive Radio in 4G/5G Wireless Communication Systems*, S. S. Moghaddam, Ed. London: IntechOpen, 2018, ch. 4.
- [42] A. M. Elmahdy, A. El-Keyi, T. ElBatt, and K. G. Seddik, “Optimizing cooperative cognitive radio networks performance with primary QoS provisioning,” *IEEE Transactions on Communications*, vol. 65, no. 4, pp. 1451–1463, 2016.
- [43] Y.-C. Liang, *Dynamic spectrum management: From cognitive radio to blockchain and artificial intelligence*. Springer Nature, 2020.
- [44] C. A. Pahalson, L. H. Crockett, and S. Weiss, “Detection of weak transient broadband signals using a polynomial subspace and likelihood ratio test approach,” in *32nd European Signal Processing Conference (EUSIPCO)*, Lyon, France, 2024, pp. 1312–1316.
- [45] —, “Detection of weak transient broadband signals: subspace and likelihood ratio test approaches,” *Science Talks*, vol. 14, p. 100451, 2025.
- [46] —, “Computational and numerical properties of a broadband subspace-based likelihood ratio test,” in *IEEE High Performance Extreme Computing Conference*, Waltham, MA, September 2024.
- [47] C. A. D. Pahalson and S. Weiss, “Broadband array time reversal method for jamming with protective constraints,” in *Proceedings of the 23rd IEEE Statistical Signal Processing Workshop (SSP)*, Edinburgh, Scotland, Jun. 2025, pp. 1–5.
- [48] C. A. Pahalson, S. Weiss, T. Clarke, J. L. Deeks, and D. P. Williams, “Estimation of fluctuating power spectral density across a sensor array,” in *ITG 28th Interna-*

Bibliography

- tional Workshop on Smart Antennas*, Erlangen, Germany, September 2025, pp. 7–12.
- [49] Y.-C. Liang, K.-C. Chen, G. Y. Li, and P. Mahonen, “Cognitive radio networking and communications: An overview,” *IEEE transactions on vehicular technology*, vol. 60, no. 7, pp. 3386–3407, 2011.
- [50] S. Haykin, D. J. Thomson, and J. H. Reed, “Spectrum sensing for cognitive radio,” *Proceedings of the IEEE*, vol. 97, no. 5, pp. 849–877, 2009.
- [51] J. A. Hanley and B. J. McNeil, “The meaning and use of the area under a receiver operating characteristic (roc) curve.” *Radiology*, vol. 143, no. 1, pp. 29–36, 1982.
- [52] R. D. Boddu, “Experimental validation of spectrum sensing on various transceivers using software defined radio,” *Wireless Personal Communications*, vol. 109, no. 3, pp. 1615–1630, 2019.
- [53] S. K. Yoo, P. C. Sofotasios, S. L. Cotton, S. Muhaidat, O. S. Badarneh, and G. K. Karagiannidis, “Entropy and energy detection-based spectrum sensing over composite fading channels,” *IEEE Transactions on Communications*, vol. 67, no. 7, pp. 4641–4653, 2019.
- [54] F. F. Digham, M.-S. Alouini, and M. K. Simon, “On the energy detection of unknown signals over fading channels,” in *IEEE International Conference on Communications, 2003. ICC’03.*, vol. 5. Ieee, 2003, pp. 3575–3579.
- [55] A. Ghasemi and E. S. Sousa, “Collaborative spectrum sensing for opportunistic access in fading environments,” in *First IEEE International Symposium on New Frontiers in Dynamic Spectrum Access Networks, 2005. DySPAN 2005.* IEEE, 2005, pp. 131–136.
- [56] I. Kakalou, D. Papadopoulou, T. Xifilidis, K. E. Psannis, K. Siakavara, and Y. Ishibashi, “A survey on spectrum sensing algorithms for cognitive radio net-

Bibliography

- works,” in *2018 7th International Conference on Modern Circuits and Systems Technologies (MOCASST)*. IEEE, 2018, pp. 1–4.
- [57] S. Agrawal, A. Samant, and S. Yadav, “Spectrum sensing in cognitive radio networks and metacognition for dynamic spectrum sharing between radar and communication system: A review,” *Physical Communication*, p. 101673, 2022.
- [58] F. Benedetto and G. Giunta, “A novel pu sensing algorithm for constant energy signals,” *IEEE Transactions on Vehicular Technology*, vol. 67, no. 1, pp. 827–831, 2017.
- [59] A. J. Onumanyi, A. M. Abu-Mahfouz, and G. P. Hancke, “A comparative analysis of local and global adaptive threshold estimation techniques for energy detection in cognitive radio,” *Physical Communication*, vol. 29, pp. 1–11, 2018.
- [60] K. Arshid, Z. Jianbiao, I. Hanif, R. Munir, M. Yaqub, and U. Tariq, “Energy detection based spectrum sensing strategy for crn,” in *2020 IEEE international conference on artificial intelligence and information systems (ICAIS)*. IEEE, 2020, pp. 107–112.
- [61] Y. Arjoune and N. Kaabouch, “A comprehensive survey on spectrum sensing in cognitive radio networks: Recent advances, new challenges, and future research directions,” *Sensors*, vol. 19, no. 1, p. 126, 2019.
- [62] J. Vartiainen, H. Karvonen, M. Matinmikko-Blue, A. Matos, and C. Silva, “Cooperative sensing with WIBA energy detection under rural area channel conditions,” in *2019 IEEE 90th Vehicular Technology Conference (VTC2019-Fall)*. IEEE, 2019, pp. 1–6.
- [63] H. Oh and H. Nam, “Energy detection scheme in the presence of burst signals,” *IEEE Signal Processing Letters*, vol. 26, no. 4, pp. 582–586, 2019.

Bibliography

- [64] N.-S. Kim and J. M. Rabaey, “A dual-resolution wavelet-based energy detection spectrum sensing for uwb-based cognitive radios,” *IEEE Transactions on Circuits and Systems I: Regular Papers*, vol. 65, no. 7, pp. 2279–2292, 2017.
- [65] A. Ranjan, B. Singh *et al.*, “Design and analysis of spectrum sensing in cognitive radio based on energy detection,” in *2016 International Conference on Signal and Information Processing (IconSIP)*. IEEE, 2016, pp. 1–5.
- [66] R. Verma and A. Mahapatro, “Cognitive radio: Energy detection using wavelet packet transform for spectrum sensing,” in *2017 Third International Conference on Advances in Electrical, Electronics, Information, Communication and Bio-Informatics (AEEICB)*. IEEE, 2017, pp. 168–172.
- [67] L. Gahane, P. Sharma, N. Varshney, T. A. Tsiftsis, and P. , “An improved energy detector for mobile cognitive users over generalized fading channels,” *IEEE Transactions on Communications*, vol. 66, no. 2, pp. 534–545, 2017.
- [68] A. Nafkha, “Standard condition number based spectrum sensing under asynchronous primary user activity,” *IEEE Access*, vol. 8, pp. 159 234–159 243, 2020.
- [69] A. Kumar, P. Thakur, S. Pandit, and G. Singh, “Analysis of optimal threshold selection for spectrum sensing in a cognitive radio network: an energy detection approach,” *Wireless Networks*, vol. 25, no. 7, pp. 3917–3931, 2019.
- [70] B. Sarala, S. R. Devi, and J. J. J. Sheela, “Spectrum energy detection in cognitive radio networks based on a novel adaptive threshold energy detection method,” *Computer Communications*, vol. 152, pp. 1–7, 2020.
- [71] A. Nasrallah, A. Hamza, T. Boukaba, G. Baudoin, and A. Messani, “Energy detection with adaptive threshold for cognitive radio,” in *2018 International Conference on Communications and Electrical Engineering (ICCEE)*. IEEE, 2018, pp. 1–5.

Bibliography

- [72] M. Z. Alom, T. Godder, M. N. Morshed, and A. Maali, “Enhanced spectrum sensing based on energy detection in cognitive radio network using adaptive threshold,” in *2017 International Conference on Networking, Systems and Security (NSysS)*. IEEE, 2017, pp. 138–143.
- [73] A. Martian, M. J. A. Al Sammarraie, C. Vlădeanu, and D. C. Popescu, “Three-event energy detection with adaptive threshold for spectrum sensing in cognitive radio systems,” *Sensors*, vol. 20, no. 13, p. 3614, 2020.
- [74] S. Madbushi and M. Rukmini, “Mitigation of primary user emulation attack using a new energy detection method in cognitive radio networks,” *Journal of Central South University*, vol. 29, no. 5, pp. 1510–1520, 2022.
- [75] G. Verma and O. Sahu, “Intelligent selection of threshold in cognitive radio system,” *Telecommunication systems*, vol. 63, pp. 547–556, 2016.
- [76] W. A. Gardner, “Exploitation of spectral redundancy in cyclostationary signals,” *IEEE Signal Processing Magazine*, vol. 8, no. 2, pp. 14–36, Apr. 1991.
- [77] M. Ghozzi, F. Marx, M. Dohler, and J. Palicot, “Cyclostationarity-based test for detection of vacant frequency bands,” in *2006 1st International Conference on Cognitive Radio Oriented Wireless Networks and Communications*. IEEE, 2006, pp. 1–5.
- [78] M. Oner and F. Jondral, “Cyclostationarity based air interface recognition for software radio systems,” in *Proceedings. 2004 IEEE Radio and Wireless Conference (IEEE Cat. No. 04TH8746)*. IEEE, 2004, pp. 263–266.
- [79] M. Subhedar and G. Birajdar, “Spectrum sensing techniques in cognitive radio networks: A survey,” *International Journal of Next-Generation Networks*, vol. 3, no. 2, pp. 37–51, 2011.
- [80] J. G. Proakis and M. Salehi, *Digital Communications*, 5th ed. McGraw-Hill, 2008.

Bibliography

- [81] T. Yucek and H. Arslan, “A survey of spectrum sensing algorithms for cognitive radio applications,” *IEEE communications surveys & tutorials*, vol. 11, no. 1, pp. 116–130, 2009.
- [82] A. M. Wyglinski, M. Nekovee, and Y. T. Hou, *Cognitive Radio Communications and Networks: Principles and Practice*. Elsevier, 2010.
- [83] Y. Zeng and Y.-C. Liang, “Spectrum-sensing algorithms for cognitive radio based on statistical covariances,” *IEEE transactions on Vehicular Technology*, vol. 58, no. 4, pp. 1804–1815, 2008.
- [84] —, “Covariance based signal detections for cognitive radio,” in *2007 2nd IEEE International Symposium on New Frontiers in Dynamic Spectrum Access Networks*. IEEE, 2007, pp. 202–207.
- [85] A.-Z. Chen and Z.-P. Shi, “A real-valued weighted covariance-based detection method for cognitive radio networks with correlated multiple antennas,” *IEEE Communications Letters*, vol. 22, no. 11, pp. 2290–2293, 2018.
- [86] A.-Z. Chen, Z.-P. Shi, and J. Xiong, “Generalized real-valued weighted covariance-based detection methods for cognitive radio networks with correlated multiple antennas,” *IEEE Access*, vol. 7, pp. 34 373–34 382, 2019.
- [87] A. M. Tulino and S. Verdú, *Random matrix theory and wireless communications*. Now Publishers Inc, 2004.
- [88] R. Couillet and M. Debbah, *Random matrix methods for wireless communications*. Cambridge University Press, 2011.
- [89] K. Bouallegue, I. Dayoub, M. Gharbi, and K. Hassan, “Blind spectrum sensing using extreme eigenvalues for cognitive radio networks,” *IEEE Communications Letters*, vol. 22, no. 7, pp. 1386–1389, 2017.

Bibliography

- [90] R. Ahmed, Y. Chen, and B. Hassan, "Deep learning-driven opportunistic spectrum access (osa) framework for cognitive 5g and beyond 5g (b5g) networks," *Ad Hoc Networks*, vol. 123, p. 102632, 2021.
- [91] H. S. Fouda, A. H. Hussein, and M. A. Attia, "Efficient GLRT/DOA spectrum sensing algorithm for single primary user detection in cognitive radio systems," *AEU-International Journal of Electronics and Communications*, vol. 88, pp. 98–109, 2018.
- [92] A. Zaimbashi and J. Li, "Tunable adaptive target detection with kernels in collocated mimo radar," *IEEE Transactions on Signal Processing*, vol. 68, pp. 1500–1514, 2020.
- [93] J. Singh and A. Shukla, "Spectrum sensing in mimo cognitive radio networks using likelihood ratio tests with unknown csi," in *Intelligent Communication, Control and Devices: Proceedings of ICICCD 2018*. Springer, 2020, pp. 185–193.
- [94] M. Al-Amidie, A. Al-Asadi, A. C. Micheas, and N. E. Islam, "Spectrum sensing based on bayesian generalised likelihood ratio for cognitive radio systems with multiple antennas," *IET Communications*, vol. 13, no. 3, pp. 305–311, 2019.
- [95] A. Patel, H. Ram, A. K. Jagannatham, and P. K. Varshney, "Robust cooperative spectrum sensing for mimo cognitive radio networks under csi uncertainty," *IEEE Transactions on Signal Processing*, vol. 66, no. 1, pp. 18–33, 2017.
- [96] A. Kumar, A. S. Khan, N. Modanwal, and S. Saha, "Experimental studies on energy and eigenvalue based spectrum sensing algorithms using USRP devices in OFDM systems," *Radio Science*, vol. 55, no. 8, pp. 1–11, 2020.
- [97] M. Lin, W. Wang, X. Hong, and W. Zhang, "Glrt approach for multi-antenna-based spectrum sensing under interference," *IEEE Communications Letters*, vol. 24, no. 7, pp. 1524–1528, 2020.

Bibliography

- [98] C. Liu, H. Li, J. Wang, and M. Jin, “Optimal eigenvalue weighting detection for multi-antenna cognitive radio networks,” *IEEE Transactions on Wireless Communications*, vol. 16, no. 4, pp. 2083–2096, 2016.
- [99] T. M. Getu, W. Ajib, and R. Landry, “Simple f -test-based spectrum sensing techniques for multi-antenna cognitive radios,” *IEEE Transactions on Communications*, vol. 66, no. 11, pp. 5081–5096, 2018.
- [100] T. M. Getu, W. Ajib, R. Landry, and G. Kaddoum, “Toward overcoming a hidden terminal problem arising in mimo cognitive radio networks: a tensor-based spectrum sensing algorithm,” *IEEE Transactions on Vehicular Technology*, vol. 68, no. 10, pp. 9833–9847, 2019.
- [101] Z. O. Dawood and H. M. Fadhil, “Improvement of energy consumption in MIMO with cognitive radio networks,” *Bulletin of Electrical Engineering and Informatics*, vol. 11, no. 2, pp. 862–869, 2022.
- [102] M. S. Miah, M. Schukat, and E. Barrett, “Sensing and throughput analysis of a mu-mimo based cognitive radio scheme for the internet of things,” *Computer Communications*, vol. 154, pp. 442–454, 2020.
- [103] B. Soni, D. K. Patel, Z. Ding, Y. L. Guan, and S. Sun, “On sensing performance of multi-antenna mobile cognitive radio conditioned on primary user activity statistics,” *IEEE Transactions on Wireless Communications*, vol. 21, no. 5, pp. 3381–3394, 2021.
- [104] S. Redif, S. Weiss, and J. G. McWhirter, “Relevance of polynomial matrix decompositions to broadband blind signal separation,” *Signal Processing*, vol. 134, pp. 76–86, 2017.
- [105] V. Neo, S. Redif, J. McWhirter, J. Pestana, I. Proudler, S. Weiss, and P. Naylor, “Polynomial eigenvalue decomposition for multichannel broadband signal processing,” *IEEE Signal Processing Magazine*, vol. 40, no. 7, pp. 18–37, Nov. 2023.

Bibliography

- [106] S. Redif, J. G. McWhirter, and S. Weiss, “Design of FIR paraunitary filter banks for subband coding using a polynomial eigenvalue decomposition,” *IEEE Transactions on Signal Processing*, vol. 59, no. 11, pp. 5253–5264, 2011.
- [107] J. G. McWhirter, P. D. Baxter, T. Cooper, S. Redif, and J. Foster, “An EVD algorithm for para-hermitian polynomial matrices,” *IEEE Transactions on Signal Processing*, vol. 55, no. 5, pp. 2158–2169, 2007.
- [108] P. P. Vaidyanathan, *Multirate Systems and Filter Banks*. Englewood Cliffs: Prentice Hall, 1993.
- [109] S. Weiss, J. Pestana, and I. K. Proudler, “On the existence and uniqueness of the eigenvalue decomposition of a parahermitian matrix,” *IEEE Transactions on Signal Processing*, vol. 66, no. 10, pp. 2659–2672, 2018.
- [110] S. Weiss, J. Pestana, I. K. Proudler, and F. K. Coutts, “Corrections to “on the existence and uniqueness of the eigenvalue decomposition of a parahermitian matrix”,” *IEEE Transactions on Signal Processing*, vol. 66, no. 23, pp. 6325–6327, Dec. 2018.
- [111] T. Betcke, N. J. Higham, V. Mehrmann, C. Schröder, and F. Tisseur, “NLEVP: A collection of nonlinear eigenvalue problems,” *ACM Transactions on Mathematical Software*, vol. 39, no. 2, pp. 7:1–7:28, Feb. 2013.
- [112] A. Papoulis, *Probability, Random Variables, and Stochastic Processes*, 3rd ed. New York: McGraw-Hill, 1991.
- [113] O. T. Waheed, A. Shabra, and I. A. M. Elfadel, “Impact of fractional bandwidth on the bit error rate of a beamforming system,” in *IEEE 59th International Midwest Symposium on Circuits and Systems*, Abu Dhabi, United Arab Emirates, October 2016, pp. 1–4.
- [114] R. T. Compton, *Adaptive Antennas*. Prentice Hall, 1988.

Bibliography

- [115] M. Zatman, “How narrow is narrowband?” *IEE Proceedings - Radar, Sonar and Navigation*, vol. 145, pp. 85–91(6), April 1998. [Online]. Available: https://digital-library.theiet.org/content/journals/10.1049/ip-rsn_19981670
- [116] R. T. Compton, ““The Bandwidth Performance of a Two-Element Adaptive Array with Tapped Delay-Line Processing”,” *IEEE Transactions on Antennas and Propagation*, vol. Vol.36, no. No.1, pp. pp.4–14, January 1988.
- [117] E. W. Vook and R. T. Compton, Jr., “Bandwidth Performance of Linear Adaptive Arrays with Tapped Delay-Line Processing,” *IEEE Transactions on Aerospace and Electronic Systems*, vol. Vol.28, no. No.3, pp. pp.901–908, July 1992.
- [118] T. Qin, H. Zhang, and X. Zhang, “Criterion for narrowband beamforming,” *Electronics Letters*, vol. 40, pp. 846–847(1), July 2004. [Online]. Available: https://digital-library.theiet.org/content/journals/10.1049/el_20040577
- [119] M. Oudin and J. P. Delmas, “Robustness of adaptive narrowband beamforming with respect to bandwidth,” *IEEE Transactions on Signal Processing*, vol. 56, no. 4, pp. 1532–1538, April 2008.
- [120] G. Golub and C. V. Loan, *Matrix Computations*, 3rd ed. Baltimore, Maryland: John Hopkins University Press, 1996.
- [121] G. Barbarino and V. Noferini, “On the Rellich eigendecomposition of para-hermitian matrices and the sign characteristics of*-palindromic matrix polynomials,” *Linear Algebra and its Applications*, vol. 672, pp. 1–27, 2023.
- [122] M. Vetterli, “A theory of multirate filter banks,” *IEEE Transactions on Acoustics, Speech, and Signal Processing*, vol. 35, no. 3, pp. 356–372, Mar. 1987.
- [123] P. P. Vaidyanathan, “Theory of optimal orthonormal subband coders,” *IEEE Transactions on Signal Processing*, vol. 46, no. 6, pp. 1528–1543, Jun. 1998.
- [124] S. Redif, S. Weiss, and J. G. McWhirter, “An approximate polynomial matrix eigenvalue decomposition algorithm for para-hermitian matrices,” in *Proceedings*

Bibliography

- of the IEEE 11th International Symposium on Signal Processing and Information Technology (ISSPIT)*, Bilbao, Spain, 2011, pp. 421–425.
- [125] R. H. Lambert, M. Joho, and H. Mathis, “Polynomial singular values for number of wideband source estimation and principal components analysis,” in *Proceedings of the International Conference on Independent Component Analysis (ICA)*, 2001, pp. 379–383.
- [126] V. W. Neo, C. Evers, and P. A. Naylor, “Speech enhancement using polynomial eigenvalue decomposition,” in *IEEE Workshop on Applications of Signal Processing to Audio and Acoustics (WASPAA)*, New Paltz, NY, October 2019, pp. 125–129.
- [127] M. Alrmah, S. Weiss, and S. Lambbotharan, “An extension of the MUSIC algorithm to broadband scenarios using polynomial eigenvalue decomposition,” in *19th European Signal Processing Conference*, Barcelona, Spain, August 2011, pp. 629–633.
- [128] S. Weiss, M. Alrmah, S. Lambbotharan, J. McWhirter, and M. Kaveh, “Broadband angle of arrival estimation methods in a polynomial matrix decomposition framework,” in *IEEE 5th International Workshop on Computational Advances in Multi-Sensor Adaptive Processing*, Dec 2013, pp. 109–112.
- [129] M. Alrmah, J. Corr, A. Alzin, K. Thompson, and S. Weiss, “Polynomial subspace decomposition for broadband angle of arrival estimation,” in *Sensor Signal Processing for Defence*, Edinburgh, Scotland, Sept 2014, pp. 1–5.
- [130] S. Weiss, N. J. Goddard, S. Somasundaram, I. K. Proudler, and P. A. Naylor, “Identification of broadband source-array responses from sensor second order statistics,” in *Sensor Signal Processing for Defence Conference*, London, UK, 2017, pp. 1–5.
- [131] A. O. Hogg, V. W. Neo, S. Weiss, C. Evers, and P. A. Naylor, “A polynomial eigenvalue decomposition MUSIC approach for broadband sound source local-

Bibliography

- ization,” in *IEEE Workshop on Applications of Signal Processing to Audio and Acoustics (WASPAA)*, New Paltz, NY, October 2021, pp. 326–330.
- [132] P. A. Regalia and P. Loubaton, “Rational subspace estimation using adaptive lossless filters,” *IEEE Transactions on Signal Processing*, vol. 40, no. 10, pp. 2392–2405, October 1992.
- [133] V. W. Neo, S. Weiss, and P. A. Naylor, “A polynomial subspace projection approach for the detection of weak voice activity,” in *Sensor Signal Processing for Defence Conference (SSPD)*, London, UK, Sep. 2022, pp. 1–5.
- [134] V. W. Neo, S. Weiss, S. W. McKnight, A. O. T. Hogg, and P. A. Naylor, “Polynomial eigenvalue decomposition-based target speaker voice activity detection in the presence of competing talkers,” in *17th International Workshop on Acoustic Signal Enhancement (IWAENC)*, Bamberg, Germany, Sep. 2022.
- [135] T. Blumensath, M. Yaghoobi, and M. E. Davies, “Iterative hard thresholding and l0 regularisation,” in *IEEE International Conference on Acoustics, Speech and Signal Processing*, vol. 3, Honolulu, Hawaii, 2007, pp. III-877–III-880.
- [136] M. Yaghoobi, S. Nam, R. Gribonval, and M. E. Davies, “Constrained overcomplete analysis operator learning for cospase signal modelling,” *IEEE Transactions on Signal Processing*, vol. 61, no. 9, pp. 2341–2355, 2013.
- [137] Z. Wang, J. G. McWhirter, J. Corr, and S. Weiss, “Multiple shift second order sequential best rotation algorithm for polynomial matrix EVD,” in *23rd European Signal Processing Conference*, Nice, France, September 2015, pp. 844–848.
- [138] S. Redif, S. Weiss, and J. G. McWhirter, “Sequential matrix diagonalization algorithms for polynomial EVD of parahermitian matrices,” *IEEE Transactions on Signal Processing*, vol. 63, no. 1, pp. 81–89, 2015.
- [139] J. Corr, K. Thompson, S. Weiss, J. McWhirter, S. Redif, and I. Proudler, “Multiple shift maximum element sequential matrix diagonalisation for parahermitian

Bibliography

- matrices,” in *Proceedings of the IEEE Workshop on Statistical Signal Processing (SSP)*, Gold Coast, Australia, June 2014, pp. 312–315.
- [140] V. W. Neo and P. A. Naylor, “Second order sequential best rotation algorithm with householder reduction for polynomial matrix eigenvalue decomposition,” in *Proceedings of the IEEE International Conference on Acoustics, Speech and Signal Processing (ICASSP)*, Brighton, UK, May 2019, pp. 8043–8047.
- [141] J. G. McWhirter and Z. Wang, “A novel insight to the SBR2 algorithm for diagonalising para-hermitian matrices,” in *11th IMA Conference on Mathematics in Signal Processing*, Birmingham, UK, December 2016.
- [142] S. Icart and P. Comon, “Some properties of laurent polynomial matrices,” in *Proceedings of the 9th IMA Conference on Mathematics in Signal Processing*, Birmingham, UK, Dec. 2012.
- [143] F. Coutts, K. Thompson, S. Weiss, and I. Proudler, “Impact of fast-converging PEVD algorithms on broadband AoA estimation,” in *Sensor Signal Processing for Defence Conference*, London, UK, December 2017, pp. 1–5.
- [144] M. Tohidian, H. Amindavar, and R. A. M. Reza, “A dft-based approximate eigenvalue and singular value decomposition of polynomial matrices,” *EURASIP Journal on Advances in Signal Processing*, vol. 2013, no. 1, pp. 1–16, 2013.
- [145] S. Weiss, I. K. Proudler, F. K. Coutts, and J. Pestana, “Iterative approximation of analytic eigenvalues of a parahermitian matrix EVD,” in *IEEE International Conference on Acoustics, Speech and Signal Processing*, Brighton, UK, 2019, pp. 8038–8042.
- [146] S. Weiss, I. K. Proudler, and F. K. Coutts, “Eigenvalue decomposition of a parahermitian matrix: extraction of analytic eigenvalues,” *IEEE Transactions on Signal Processing*, vol. 69, pp. 722–737, January 2021.

Bibliography

- [147] F. A. Khattak, I. K. Proudler, and S. Weiss, “Scalable analytic eigenvalue extraction algorithm,” *IEEE Access*, vol. 12, pp. 166 652–166 659, Dec. 2024.
- [148] S. J. Schlecht and S. Weiss, “Reconstructing analytic dinosaurs: Polynomial eigenvalue decomposition for eigenvalues with unmajorised ground truth,” in *32nd European Signal Processing Conference*, Lyon, France, August 2024, pp. 1287–1291.
- [149] F. K. Coutts, K. Thompson, J. Pestana, I. Proudler, and S. Weiss, “Enforcing eigenvector smoothness for a compact DFT-based polynomial eigenvalue decomposition,” in *10th IEEE Workshop on Sensor Array and Multichannel Signal Processing*, July 2018, pp. 1–5.
- [150] S. Weiss, I. K. Proudler, F. K. Coutts, and J. Deeks, “Extraction of analytic eigenvectors from a parahermitian matrix,” in *Sensor Signal Processing for Defence Conference*, Edinburgh, UK, September 2020, pp. 1–5.
- [151] S. Weiss, I. K. Proudler, F. K. Coutts, and F. A. Khattak, “Eigenvalue decomposition of a parahermitian matrix: Extraction of analytic eigenvectors,” *IEEE Transactions on Signal Processing*, vol. 71, pp. 1642–1656, Apr. 2023.
- [152] E. F. Deprettere, *SVD and signal processing: algorithms, applications and architectures*. North-Holland Publishing Co., 1989.
- [153] R. J. Vaccaro, *SVD and Signal Processing II: Algorithms, analysis and applications*. Elsevier Science Inc., 1991.
- [154] M. Moonen and B. De Moor, *SVD and signal processing, III: Algorithms, architectures and applications*. Elsevier, 1995.
- [155] M. Vu and A. Paulraj, “Mimo wireless linear precoding,” *IEEE Signal Processing Magazine*, vol. 24, no. 5, pp. 86–105, 2007.

Bibliography

- [156] S. Weiss, I. K. Proudler, G. Barbarino, J. Pestana, and J. G. McWhirter, “On properties and structure of the analytic singular value decomposition,” *IEEE Transactions on Signal Processing*, vol. 72, pp. 2260–2275, Apr. 2024.
- [157] B. De Moor and S. Boyd, “Analytic properties of singular values and vectors,” *KU Leuven, Tech. Rep.*, 1989.
- [158] A. Bunse-Gerstner, R. Byers, V. Mehrmann, and N. K. Nichols, “Numerical computation of an analytic singular value decomposition of a matrix valued function,” *Numerische Mathematik*, vol. 60, no. 1, pp. 1–39, Dec. 1991.
- [159] G. Barbarino, “On the periodicity of singular vectors and the holomorphic block-circulant SVD on the unit circumference,” *Linear Algebra and its Applications*, vol. 721, pp. 465–483, Sep. 2025.
- [160] S. Weiss and G. Barbarino, “Relations between analytic spectral and singular-value decompositions,” in *33rd European Signal Processing Conference*, Palermo, Italy, Sep. 2025, pp. 2272–2276.
- [161] C. H. Ta and S. Weiss, “A design of precoding and equalisation for broadband mimo systems,” in *Proc. 44th Asilomar Conference on Signals, Systems and Computers*, Pacific Grove, CA, USA, Nov. 2007, pp. 1616–1620.
- [162] —, “A Jointly Optimal Precoder and Block Decision Feedback Equaliser Design With Low Redundancy,” in *15th European Signal Processing Conference*, Poznan, Poland, September 2007, pp. 489–492.
- [163] N. Moret, A. Tonello, and S. Weiss, “Mimo precoding for filter bank modulation systems based on PSVD,” in *Proc. IEEE 73rd Vehicular Technology Conference (VTC Spring)*, Budapest, Hungary, May 2011, pp. 1–5.
- [164] A. I. Pérez-Neira, M. Caus, R. Zakaria, D. L. Ruyet, E. Kofidis, M. Haardt, X. Mestre, and Y. Cheng, “Mimo signal processing in offset-qam based filter

Bibliography

- bank multicarrier systems,” *IEEE Transactions on Signal Processing*, vol. 64, no. 21, pp. 5733–5762, Nov. 2016.
- [165] Z. Wang, A. Sandmann, J. G. McWhirter, and A. Ahrens, “Multiple shift sbr2 algorithm for calculating the svd of broadband optical mimo systems,” in *Proc. 39th International Conference on Telecommunications and Signal Processing (TSP)*. Vienna, Austria: IEEE, Jun. 2016, pp. 433–436.
- [166] J. G. McWhirter, “An algorithm for polynomial matrix svd based on generalised kogbetliantz transformations,” in *Proceedings of the 18th European Signal Processing Conference (EUSIPCO)*, Aalborg, Denmark, Aug. 2010, pp. 457–461.
- [167] F. Khattak, I. Proudler, J. McWhirter, and S. Weiss, “Generalised sequential matrix diagonalisation for the SVD of polynomial matrices,” in *International Conference on Defence for Signal Processing*, Edinburgh, Scotland, Sep. 2023.
- [168] M. A. Bakhit, F. A. Khattak, I. K. Proudler, S. Weiss, and G. W. Rice, “Compact order polynomial singular value decomposition of a matrix of analytic functions,” in *9th IEEE International Workshop on Computational Advances in Multi-Sensor Adaptive Processing*, Los Sueños, Costa Rica, Dec. 2023, pp. 416–420.
- [169] S. Weiss, S. Schlecht, O. Das, and E. De Sena, “Polynomial Procrustes problem: Paraunitary approximation of matrices of analytic functions,” in *31st European Signal Processing Conference*, Helsinki, Finland, 2023, pp. 1629–1633.
- [170] S. Weiss, S. J. Schlecht, and M. Moonen, “Polynomial procrustes solution for randomly perturbed near-paraunitary systems,” in *23rd IEEE Statistical Signal Processing Workshop*, Edinburgh, Scotland, Jun. 2025, pp. 231–235.
- [171] S. Weiss, S. Schlecht, and M. Moonen, “Best least squares paraunitary approximation: Analytic procrustes problem,” *IEEE Transactions on Signal Processing*, pp. 904–919, February 2026.

Bibliography

- [172] —, “Best least squares paraunitary approximation for an extended range of polynomial matrices,” in *European Signal Processing Conference*, Bruges, Belgium, Sep. 2026.
- [173] Z. Quan, S. Cui, H. V. Poor, and A. H. Sayed, “Collaborative wideband sensing for cognitive radios,” *IEEE Signal Processing Magazine*, vol. 25, no. 6, pp. 60–73, 2008.
- [174] E. Axell, G. Leus, E. G. Larsson, and H. V. Poor, “Spectrum sensing for cognitive radio: State-of-the-art and recent advances,” *IEEE Signal Processing Magazine*, vol. 29, no. 3, pp. 101–116, 2012.
- [175] M. H. Al-Ali and K. Ho, “Objective bayesian approach for binary hypothesis testing of multivariate gaussian observations,” *IEEE Transactions on Information Theory*, vol. 69, no. 2, pp. 1337–1354, 2022.
- [176] B. Friedlander and B. Porat, “Detection of transient signals by the Gabor representation,” *IEEE transactions on acoustics, speech, and signal processing*, vol. 37, no. 2, pp. 169–180, 1989.
- [177] —, “Performance analysis of transient detectors based on a class of linear data transforms,” *IEEE transactions on information theory*, vol. 38, no. 2, pp. 665–673, 1992.
- [178] B. Porat and B. Friedlander, “Performance analysis of a class of transient detection algorithms—a unified framework,” *IEEE Transactions on Signal Processing*, vol. 40, no. 10, pp. 2536–2546, 1992.
- [179] S. Haykin, *Adaptive Filter Theory*, 2nd ed. Englewood Cliffs: Prentice Hall, 1991.
- [180] L. L. Scharf and B. Friedlander, “Matched subspace detectors,” *IEEE Transactions on signal processing*, vol. 42, no. 8, pp. 2146–2157, 1994.

Bibliography

- [181] P. Strobach, “Low rank detection of multichannel gaussian signals using a constrained inverse,” in *Proceedings of IEEE International Conference on Acoustics, Speech and Signal Processing*, vol. 4, 1994, pp. IV–245.
- [182] D. Lundstrom, M. Viberg, and A. Zoubir, “Multiple transient estimation using bootstrap and subspace methods,” in *Ninth IEEE Signal Processing Workshop on Statistical Signal and Array Processing (Cat. No. 98TH8381)*. IEEE, 1998, pp. 184–187.
- [183] Z. Wang and P. Willett, “A performance study of some transient detectors,” *IEEE Transactions on Signal Processing*, vol. 48, no. 9, pp. 2682–2685, 2000.
- [184] Z. Wang and P. K. Willett, “All-purpose and plug-in power-law detectors for transient signals,” *IEEE Transactions on Signal Processing*, vol. 49, no. 11, pp. 2454–2466, 2001.
- [185] F. Labeau, J.-C. Chiang, M. Kieffer, P. Duhamel, L. Vandendorpe, and B. Macq, “Oversampled filter banks as error correcting codes: Theory and impulse noise correction,” *IEEE Transactions on Signal Processing*, vol. 53, no. 12, pp. 4619–4630, 2005.
- [186] O. Besson, “Maximum likelihood covariance matrix estimation from two possibly mismatched data sets,” *Signal Processing*, vol. 167, p. 107285, 2020.
- [187] E. Lehmann and J. Romano, *Testing Statistical Hypotheses*, 4th ed. Springer, 2022.
- [188] C. H. Ta and S. Weiss, “Shortening the order of paraunitary matrices in SBR2 algorithm,” in *6th International Conference on Information, Communications & Signal Processing*, Singapore, December 2007, pp. 1–5.
- [189] J. Corr, K. Thompson, S. Weiss, I. K. Proudler, and J. G. McWhirter, “Row-shift corrected truncation of paraunitary matrices for PEVD algorithms,” in *23rd*

Bibliography

- European Signal Processing Conference (EUSIPCO)*, Nice, France, September 2015, pp. 849–853.
- [190] J. Corr, K. Thompson, S. Weiss, I. Proudler, and J. McWhirter, “Shortening of paraunitary matrices obtained by polynomial eigenvalue decomposition algorithms,” in *2015 Sensor Signal Processing for Defence (SSPD)*, Edinburgh, Scotland, September 2015, pp. 1–5.
- [191] D. Hammarwall, M. Bengtsson, and B. Ottersten, “Acquiring partial CSI for spatially selective transmission by instantaneous channel norm feedback,” *IEEE Transactions on Signal Processing*, vol. 56, no. 3, pp. 1188–1204, Mar 2008.
- [192] E. Bjornson, D. Hammarwall, and B. Ottersten, “Exploiting quantized channel norm feedback through conditional statistics in arbitrarily correlated mimo systems,” *IEEE Transactions on Signal Processing*, vol. 57, no. 10, pp. 4027–4041, Oct 2009.
- [193] A. Das and W. S. Geisler, “Methods to integrate multinormals and compute classification measures,” *arXiv preprint arXiv:2012.14331*, 2020.
- [194] H. Solomon and M. A. Stephens, “Distribution of a sum of weighted chi-square variables,” *Journal of the American Statistical Association*, vol. 72, no. 360a, pp. 881–885, 1977.
- [195] C. Delaosa, J. Pestana, N. J. Goddard, S. Somasundaram, and S. Weiss, “Sample space-time covariance matrix estimation,” in *IEEE International Conference on Acoustics, Speech and Signal Processing*, Brighton, UK, 2019, pp. 8033–8037.
- [196] C. Delaosa, J. Pestana, N. J. Goddard, S. D. Somasundaram, and S. Weiss, “Support estimation of a sample space-time covariance matrix,” in *Sensor Signal Processing for Defence Conference*, Brighton, UK, 2019, pp. 1–5.

Bibliography

- [197] C. Delaosa, J. Pestana, I. K. Proudler, and S. Weiss, “Impact of space–time covariance matrix estimation on bin-wise eigenvalue and eigenspace perturbations,” *Signal Processing*, vol. 233, p. 109946, 2025.
- [198] C. Delaosa, F. K. Coutts, J. Pestana, and S. Weiss, “Impact of space-time covariance estimation errors on a parahermitian matrix EVD,” in *IEEE 10th Sensor Array and Multichannel Signal Processing Workshop (SAM)*, Sheffield, UK, 2018, pp. 164–168.
- [199] T. Kato, *Perturbation Theory for Linear Operators*. Berlin: Springer, 1980.
- [200] F. A. Khattak, S. Weiss, I. K. Proudler, and J. G. McWhirter, “Space-time covariance matrix estimation: Loss of algebraic multiplicities of eigenvalues,” in *56th Asilomar Conference on Signals, Systems, and Computers*, Pacific Grove, CA, November 2022, pp. 975–979.
- [201] M. Bakhit, F. A. Khattak, I. K. Proudler, and S. Weiss, “Impact of estimation errors of a matrix of transfer functions onto its analytic singular values and their potential algorithmic extraction,” in *High Performance Embedded Computing Conference*, Waltham, MA, September 2024.
- [202] W. A. Gardner, “Introduction to random processes: with applications to signals and systems,” (*No Title*), 1990.
- [203] W. Bär and F. Dittrich, “Useful formula for moment computation of normal random variables with nonzero means,” *IEEE Transactions on Automatic Control*, vol. 16, no. 3, pp. 263–265, 1971.
- [204] J. M. Mendel, “Tutorial on higher-order statistics (spectra) in signal processing and system theory: Theoretical results and some applications,” *Proceedings of the IEEE*, vol. 79, no. 3, pp. 278–305, 1991.

Bibliography

- [205] P. J. Schreier and L. L. Scharf, *Statistical Signal Processing of Complex-Valued Data: The Theory of Improper and Non-Circular Signals*. Cambridge University Press, 2010.
- [206] D. D. Ariananda and G. Leus, “Compressive wideband power spectrum estimation,” *IEEE Transactions on Signal Processing*, vol. 60, no. 9, pp. 4775–4789, 2012.
- [207] Y. Chen, F. Han, Y. H. Yang, and H. Ma, “Time-reversal wireless paradigm for green internet of things: An overview,” *IEEE Internet of Things Journal*, vol. 1, no. 1, pp. 81–98, Feb. 2014.
- [208] Z. Liu, L. E. Emokpae, J. A. Schindall, and G. F. Edelmann, “Experimental study of acoustic channel reciprocity in the shallow ocean,” *IEEE Journal of Oceanic Engineering*, vol. 46, no. 3, pp. 1034–1044, 2020.
- [209] H. Xu, J. Zhang, P. Tang, L. Tian, Q. Wang, and G. Liu, “An empirical study on channel reciprocity in TDD and FDD systems,” *IEEE Open Journal of Vehicular Technology*, vol. 5, pp. 108–124, 2023.
- [210] M. Fink, G. Montaldo, and M. Tanter, “Time-reversal acoustics in biomedical engineering,” *Annual review of biomedical engineering*, vol. 5, no. 1, pp. 465–497, 2003.
- [211] Q. Xu, Y. Chen, B. Wang, and K. R. Liu, “Radio biometrics: Human recognition through a wall,” *IEEE Transactions on Information Forensics and Security*, vol. 12, no. 5, pp. 1141–1155, 2017.
- [212] M. Fink, “Time reversal of ultrasonic fields. i. basic principles,” *IEEE Transactions on Ultrasonics, Ferroelectrics, and Frequency Control*, vol. 39, no. 5, pp. 555–566, 1992.

Bibliography

- [213] G. Lerosey, J. de Rosny, A. Tourin, A. Derode, G. Montaldo, and M. Fink, “Time reversal of electromagnetic waves,” *Physical Review Letters*, vol. 92, no. 19, p. 193904, 2004.
- [214] G. C. Alexandropoulos, A. Mokh, R. Khayatzadeh, J. De Rosny, M. Kamoun, A. Ourir, A. Tourin, M. Fink, and M. Debbah, “Time reversal for 6G spatiotemporal focusing: Recent experiments, opportunities, and challenges,” *IEEE Vehicular Technology Magazine*, vol. 17, no. 4, pp. 74–82, 2022.
- [215] K. Cumanan, G. C. Alexandropoulos, Z. Ding, and G. K. Karagiannidis, “Secure communications with cooperative jamming: Optimal power allocation and secrecy outage analysis,” *IEEE Transactions on Vehicular Technology*, vol. 66, no. 8, pp. 7495–7505, 2017.
- [216] X. Liu, Y. Gao, G. Zang, N. Sha, and M. Guo, “Distributionally robust secure transmission for miso downlink networks with assisting jammer,” *IEEE Access*, vol. 7, pp. 119 981–119 995, 2019.
- [217] C. Peel, Q. Spencer, A. L. Swindlehurst, and B. Hochwald, “Downlink transmit beamforming in multi-user mimo systems,” in *Processing workshop proceedings, 2004 sensor array and multichannel signal*. IEEE, 2004, pp. 43–51.
- [218] M. Schubert and H. Boche, “Iterative multiuser uplink and downlink beamforming under SINR constraints,” *IEEE Transactions on Signal Processing*, vol. 53, no. 7, pp. 2324–2334, 2005.
- [219] H. Boche and M. Schubert, “A general duality theory for uplink and downlink beamforming,” in *Proceedings IEEE 56th Vehicular Technology Conference*, vol. 1. IEEE, 2002, pp. 87–91.
- [220] H. L. V. Trees, *Detection, Estimation, and Modulation Theory: Optimum Array Processing*. New York: Wiley, 2002.

Bibliography

- [221] M. Bakhit, F. Khattak, G. Rice, I. Proudler, and S. Weiss, “Recovering ground truth singular values from randomly perturbed MIMO transfer functions,” in *23rd IEEE Statistical Signal Processing Workshop*, Edinburgh, UK, June 2025.
- [222] F. K. Coutts, I. K. Proudler, and S. Weiss, “Efficient implementation of iterative polynomial matrix evd algorithms exploiting structural redundancy and parallelisation,” *IEEE Transactions on Circuits and Systems I: Regular Papers*, vol. 66, no. 12, pp. 4753–4766, Dec. 2019.
- [223] Q. H. Spencer and A. L. Swindlehurst, “A hybrid approach to spatial multiplexing in multiuser mimo downlinks,” *EURASIP Journal on Wireless Communications and Networking*, vol. 2004, no. 2, pp. 236–247, 2004.
- [224] Q. H. Spencer, C. B. Peel, A. L. Swindlehurst, and M. Haardt, “An introduction to the multi-user MIMO downlink,” *IEEE Communications Magazine*, vol. 42, no. 10, pp. 60–67, 2004.
- [225] D. P. Palomar and J. R. Fonollosa, “Practical algorithms for a family of water-filling solutions,” *IEEE Transactions on Signal Processing*, vol. 53, no. 2, pp. 686–695, 2005.
- [226] D. L. Fried, “Probability of getting a lucky short-exposure image through turbulence,” *Journal of the Optical Society of America*, vol. 68, no. 12, pp. 1651–1658, 1978.
- [227] M. Erol-Kantarci, H. T. Mouftah, and S. Oktug, “A survey of architectures and localization techniques for underwater acoustic sensor networks,” *IEEE Communications Surveys & Tutorials*, vol. 13, no. 3, pp. 487–502, 2011.
- [228] X. Wei, H. Guo, X. Wang, X. Wang, and M. Qiu, “Reliable data collection techniques in underwater wireless sensor networks: A survey,” *IEEE Communications Surveys & Tutorials*, vol. 24, no. 1, pp. 404–431, 2022.

Bibliography

- [229] E. Gorodetskaya, A. Malekhanov, A. Sazontov, and N. Vdovicheva, “Deep-water acoustic coherence at long ranges: theoretical prediction and effects on large-array signal processing,” *IEEE Journal of Oceanic Engineering*, vol. 24, no. 2, pp. 156–171, 1999.
- [230] H. Cox, “Line array performance when the signal coherence is spatially dependent,” *The Journal of the Acoustical Society of America*, vol. 54, no. 6, pp. 1743–1746, 1973.
- [231] A. B. Gershman, C. F. Mecklenbräuker, and J. F. Bohme, “Matrix fitting approach to direction of arrival estimation with imperfect spatial coherence of wavefronts,” *IEEE Transactions on Signal Processing*, vol. 45, no. 7, pp. 1894–1899, 1997.
- [232] H. Ge and I. P. Kirsteins, “Lucky ranging with towed arrays in underwater environments subject to non-stationary spatial coherence loss,” in *2016 IEEE International Conference on Acoustics, Speech and Signal Processing (ICASSP)*. IEEE, 2016, pp. 3156–3160.
- [233] D. A. Miles, D. Kirk, and T. Clarke, “A statistical analysis of the detection performance of a broadband splitbeam passive sonar,” *IEEE Journal of Oceanic Engineering*, vol. 31, no. 4, pp. 986–996, 2006.
- [234] A. L’her, A. Drémeau, F. Le Courtois, G. Real, X. Cristol, and Y. Stéphan, “Towards improved sonar performance using environment-informed sparse subarray processing,” in *IEEE International Conference on Acoustics, Speech and Signal Processing (ICASSP)*, Rhodes, Greece, June 2023, pp. 1–5.
- [235] A. Paulraj and T. Kailath, “Direction of arrival estimation by eigenstructure methods with imperfect spatial coherence of wave fronts,” *The Journal of the Acoustical Society of America*, vol. 83, no. 3, pp. 1034–1040, 1988.
- [236] Y. Abramovich, N. Spencer, and A. Gorokhov, “Bounds on maximum likelihood ratio—part ii: Application to antenna array detection-estimation with imperfect

Bibliography

- wavefront coherence,” *IEEE Transactions on Signal Processing*, vol. 53, no. 6, pp. 2046–2058, 2005.
- [237] O. Besson, P. Stoica, and A. B. Gershman, “Simple and accurate direction of arrival estimator in the case of imperfect spatial coherence,” *IEEE Transactions on Signal Processing*, vol. 49, no. 4, pp. 730–737, 2001.
- [238] R. Lefort and A. Drémeau, “Sub-antenna sparse processing for coherence loss in underwater source localization,” in *2017 25th European Signal Processing Conference (EUSIPCO)*. IEEE, 2017, pp. 2413–2417.
- [239] A. Zoubir, Y. Wang, and P. Chargé, “Efficient subspace-based estimator for localization of multiple incoherently distributed sources,” *IEEE Transactions on Signal Processing*, vol. 56, no. 2, pp. 532–542, 2008.
- [240] V. W. Neo, C. Evers, S. Weiss, and P. A. Naylor, “Signal compaction using polynomial EVD for spherical array processing with applications,” *IEEE/ACM Transactions on Audio, Speech, and Language Processing*, vol. 31, pp. 3537–3549, 2023.
- [241] A. P. Shikhaliev, L. C. Potter, and Y. Chi, “Low-rank structured covariance matrix estimation,” *IEEE Signal Processing Letters*, vol. 26, no. 5, pp. 700–704, 2019.
- [242] R. Zhou, J. Ying, and D. P. Palomar, “Covariance matrix estimation under low-rank factor model with nonnegative correlations,” *IEEE Transactions on Signal Processing*, vol. 70, pp. 4020–4030, 2022.
- [243] G. A. Arredondo, W. H. Chriss, and E. H. Walker, “A multipath fading simulator for mobile radio,” *IEEE Transactions on Vehicular Technology*, vol. 22, no. 4, pp. 241–244, 2013.

Bibliography

- [244] M. K. Tsatsanis and G. B. Giannakis, “Modelling and equalization of rapidly fading channels,” *International Journal of Adaptive Control and Signal Processing*, vol. 10, no. 2-3, pp. 159–176, 1996.
- [245] Z. Tang, R. C. Cannizzaro, G. Leus, and P. Banelli, “Pilot-assisted time-varying channel estimation for OFDM systems,” *IEEE Transactions on Signal Processing*, vol. 55, no. 5, pp. 2226–2238, 2007.
- [246] G. B. Giannakis and C. Tepedelenlioglu, “Basis expansion models and diversity techniques for blind identification and equalization of time-varying channels,” *Proceedings of the IEEE*, vol. 86, no. 10, pp. 1969–1986, Oct. 1998.
- [247] X. Wang, G. Wang, J. Sun, and Y. Zou, “Channel estimation with new basis expansion model for wireless communications on high speed railways,” in *2016 IEEE 83rd Vehicular Technology Conference (VTC Spring)*. IEEE, 2016, pp. 1–5.
- [248] N. M. Idrees, W. Haselmayr, D. Schellander, and A. Springer, “Time variant channel estimation using a modified complex exponential basis expansion model in LTE-OFDM systems,” in *21st Annual IEEE International Symposium on Personal, Indoor and Mobile Radio Communications*. IEEE, 2010, pp. 603–607.
- [249] N. M. Idrees, W. Haselmayr, M. Petit, and A. Springer, “Complexity reduction for time variant channel estimation in 3GPP LTE downlink,” in *Proceedings of the 11th International Conference on Telecommunications*. IEEE, 2011, pp. 47–50.
- [250] T. Zemen and C. F. Mecklenbräuker, “Time-variant channel estimation using discrete prolate spheroidal sequences,” *IEEE Transactions on Signal Processing*, vol. 53, no. 9, pp. 3597–3607, 2005.
- [251] M. Visintin, “Karhunen-Loeve expansion of a fast Rayleigh fading process,” *Electronics Letters*, vol. 32, no. 18, pp. 1712–1713, 1996.

Bibliography

- [252] Q. Zhang, X. Zhao, Y. Zeng, and S. Song, “Efficient estimation of fast fading OFDM channels,” in *2006 IEEE International Conference on Communications*, vol. 10. IEEE, 2006, pp. 4601–4605.
- [253] D. K. Borah and B. Hart, “Frequency-selective fading channel estimation with a polynomial time-varying channel model,” *IEEE Transactions on Communications*, vol. 47, no. 6, pp. 862–873, 1999.
- [254] S. Benedetto and E. Biglieri, *Principles of digital transmission: with wireless applications*. Springer Science & Business Media, 2005.
- [255] P. W. Wu and H. Lev-Ari, “Optimized estimation of moments for nonstationary signals,” *IEEE Transactions on Signal Processing*, vol. 45, no. 5, pp. 1210–1221, 1997.
- [256] W. A. Gardner, *Introduction to Random Processes: With Applications to Signals and Systems*, 2nd ed. McGraw-Hill, 1990.
- [257] S. Weiss, S. Bendoukha, A. Alzin, F. K. Coutts, I. K. Proudler, and J. Chambers, “MVDR broadband beamforming using polynomial matrix techniques,” in *23rd European signal processing Conference (EUSIPCO)*, Nice, France, September 2015, pp. 839–843.
- [258] B. Girod, R. Rabenstein, and A. Stenger, *Signals and Systems*. Chichester: J. Wiley & Sons, 2001.
- [259] F. K. Coutts, J. Corr, K. Thompson, S. Weiss, I. Proudler, and J. G. McWhirter, “Memory and complexity reduction in parahermitian matrix manipulations of PEVD algorithms,” in *24th European Signal Processing Conference*, Budapest, Hungary, Aug. 2016.
- [260] F. Haddadi, M. Malek-Mohammadi, M. M. Nayebi, and M. R. Aref, “Statistical performance analysis of MDL source enumeration in array processing,” *IEEE Transactions on Signal Processing*, vol. 58, no. 1, pp. 452–457, 2010.

Bibliography

- [261] V. Garg, I. Santamaria, D. Ramírez, and L. L. Scharf, “Subspace averaging and order determination for source enumeration,” *IEEE Transactions on Signal Processing*, vol. 67, no. 11, pp. 3028–3041, 2019.
- [262] V. Garg, D. Ramírez, and I. Santamaria, “Sparse subspace averaging for order estimation,” in *IEEE Statistical Signal Processing Workshop (SSP)*, 2021, pp. 411–415.
- [263] S. Weiss and I. K. Proudler, “Why can wiener-hopf reach accurate solutions with poor statistical estimates?” in *IEEE Workshop on Statistical Signal Processing*, Edinburgh, Scotland, Jun. 2025, pp. 146–150.
- [264] S. Weiss, I. K. Proudler, and Y. Altmann, “Accuracy of the Wiener-Hopf solution when based on sample statistics,” *IEEE Signal Processing Letters*, pp. 1106–1110, February 2026.
- [265] L. Crockett, D. Northcote, and R. W. Stewart, *Software Defined Radio with Zynq UltraScale+ RFSoc*. Strathclyde Academic Media, 2023.
- [266] F. A. Khattak, I. K. Proudler, and S. Weiss, “Scalable analytic eigenvalue extraction algorithm,” *IEEE Access*, vol. 12, pp. 166 652–166 659, Dec. 2024.

Bibliography